



National Library
of Canada

Acquisitions and
Bibliographic Services Branch

395 Wellington Street
Ottawa, Ontario
K1A 0N4

Bibliothèque nationale
du Canada

Direction des acquisitions et
des services bibliographiques

395, rue Wellington
Ottawa (Ontario)
K1A 0N4

Your file Votre référence

Our file Notre référence

NOTICE

The quality of this microform is heavily dependent upon the quality of the original thesis submitted for microfilming. Every effort has been made to ensure the highest quality of reproduction possible.

If pages are missing, contact the university which granted the degree.

Some pages may have indistinct print especially if the original pages were typed with a poor typewriter ribbon or if the university sent us an inferior photocopy.

Reproduction in full or in part of this microform is governed by the Canadian Copyright Act, R.S.C. 1970, c. C-30, and subsequent amendments.

AVIS

La qualité de cette microforme dépend grandement de la qualité de la thèse soumise au microfilmage. Nous avons tout fait pour assurer une qualité supérieure de reproduction.

S'il manque des pages, veuillez communiquer avec l'université qui a conféré le grade.

La qualité d'impression de certaines pages peut laisser à désirer, surtout si les pages originales ont été dactylographiées à l'aide d'un ruban usé ou si l'université nous a fait parvenir une photocopie de qualité inférieure.

La reproduction, même partielle, de cette microforme est soumise à la Loi canadienne sur le droit d'auteur, SRC 1970, c. C-30, et ses amendements subséquents.

Canada

University of Alberta

**Bifurcation Structure of
Isothermal and Non-isothermal flows
through Rotating Ducts**

by



Ravi K. Sharma

A thesis
submitted to the Faculty of Graduate Studies and Research
in partial fulfillment of the requirements for the degree of

Master of Science

Department of Chemical Engineering

Edmonton, Alberta

Spring 1995



National Library
of Canada

Acquisitions and
Bibliographic Services Branch

395 Wellington Street
Ottawa, Ontario
K1A 0N4

Bibliothèque nationale
du Canada

Direction des acquisitions et
des services bibliographiques

395, rue Wellington
Ottawa (Ontario)
K1A 0N4

Your file Votre référence

Our file Notre référence

THE AUTHOR HAS GRANTED AN
IRREVOCABLE NON-EXCLUSIVE
LICENCE ALLOWING THE NATIONAL
LIBRARY OF CANADA TO
REPRODUCE, LOAN, DISTRIBUTE OR
SELL COPIES OF HIS/HER THESIS BY
ANY MEANS AND IN ANY FORM OR
FORMAT, MAKING THIS THESIS
AVAILABLE TO INTERESTED
PERSONS.

L'AUTEUR A ACCORDE UNE LICENCE
IRREVOCABLE ET NON EXCLUSIVE
PERMETTANT A LA BIBLIOTHEQUE
NATIONALE DU CANADA DE
REPRODUIRE, PRETER, DISTRIBUER
OU VENDRE DES COPIES DE SA
THESE DE QUELQUE MANIERE ET
SOUS QUELQUE FORME QUE CE SOIT
POUR METTRE DES EXEMPLAIRES DE
CETTE THESE A LA DISPOSITION DES
PERSONNE INTERESSEES.

THE AUTHOR RETAINS OWNERSHIP
OF THE COPYRIGHT IN HIS/HER
THESIS. NEITHER THE THESIS NOR
SUBSTANTIAL EXTRACTS FROM IT
MAY BE PRINTED OR OTHERWISE
REPRODUCED WITHOUT HIS/HER
PERMISSION.

L'AUTEUR CONSERVE LA PROPRIETE
DU DROIT D'AUTEUR QUI PROTEGE
SA THESE. NI LA THESE NI DES
EXTRAITS SUBSTANTIELS DE CELLE-
CI NE DOIVENT ETRE IMPRIMES OU
AUTREMENT REPRODUITS SANS SON
AUTORISATION.

ISBN 0-612-01652-8

Canada

University of Alberta

Library Release Form

Name of Author:

Ravi K. Sharma

Title of Thesis:

**Bifurcation Structures of
Isothermal and Non-isothermal flows
through Rotating Ducts**

Degree:

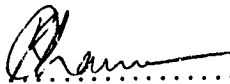
Master of Science

Year this degree granted:

Spring 1995

Permission is hereby granted to the **University of Alberta Library** to reproduce single copies of this thesis and to lend or sell such copies for private, scholarly or scientific research purposes only.

The author reserves all other publication and other rights in association with the copyright in the thesis, and except as hereinbefore provided neither the thesis nor any substantial portion thereof may be printed or otherwise reproduced in any material form whatever without the author's prior written permission.

.....

(Student's signature)

Ravi K. Sharma

Y-45, Hauz Khas

New Delhi


Pin: 110 016

India

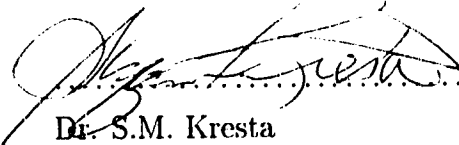
Date :*April 12 '95*.....

University of Alberta
Faculty of Graduate Studies and Research

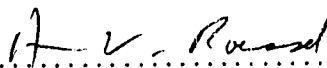
The undersigned certify that they have read, and recommend to the Faculty of Graduate Studies and Research for acceptance, a thesis entitled **Bifurcation Structures of Isothermal and Non-isothermal flows through Rotating Ducts** submitted by **Ravi K. Sharma** in partial fulfillment of the requirements for the degree of **Master of Science**.


.....

Dr. K. Nandakumar (Supervisor)


.....

Dr. S.M. Kresta


.....

Dr. H.J. Van Roessel

Date : *April 12, 1955*...

To my wife, Manju

Abstract

Fully developed flow of an incompressible Newtonian fluid driven by a pressure gradient through a straight duct that rotates about an axis perpendicular to the duct axis is analyzed under both the isothermal and nonisothermal conditions. For a circular cross-section and under isothermal conditions, a hitherto unknown solution with a four-cell flow structure appears, which coexists with the two-cell flow structure over a range of Rossby numbers. The four-cell flow structure is unstable to asymmetric perturbations, where it breaks down to a two-cell flow structure.

For a rectangular cross-section, the governing equations are discretized using spectral approximation and arclength continuation scheme is used to track the solution path. Seven solutions are reported at a Rossby number of five. When non-isothermal effects are introduced the governing equations give only asymmetric solutions. A smooth unfolding of bifurcation branches take place with heating/cooling. The unfolding of symmetry breaking bifurcation points occur through a tilted cusp.

Acknowledgments

I take this opportunity to place on record my sincere and deep gratitude to my supervisor, Dr. K. Nandakumar who has been the constant source of inspiration, guidance, and cooperation throughout the evolution of the present work. His quality work in the area of bifurcations and fluid flow was always before me to emulate. I hope, I have been able to do justice to these influences. I recall in particular many discussions which helped shape the present work.

I will also remember for a long time my association with all friends through the entire stay at University of Alberta. Thanks to Mohammad Selmi for introducing 'Spectral methods'. Special thanks to my friend Suneel for his invariable encouragement and support.

I owe much thanks to my wife, Manju for her love, support and understanding which make it possible to see the completion of the present work today.

Contents

Chapter 1

Introduction	1
1.1 Transitions in fluid flow	1
1.2 Bifurcation phenomena	2
1.3 Motion in a rotating frame	4
1.4 Creation of Vorticity by Coriolis and Buoyancy Forces	5
1.5 Organization of Thesis	7

References	10
-------------------	-----------

Chapter 2

Flow through a rotating pipe	11
2.1 Introduction	11
2.2 Governing Equations	15
2.3 Results and Discussion	16
2.4 Conclusion	22

References	36
-------------------	-----------

Chapter 3

Isothermal flow in a rotating duct	39
3.1 Introduction	39
3.2 Governing equations	42
3.3 Numerical methods	46
3.3.1 Spectral approximation	47
3.3.2 Arclength continuation	48
3.3.3 Limit points	50
3.3.4 Symmetry breaking bifurcation points	52
3.4 Results and Discussion	54
3.5 Conclusion	60

References	72
-------------------	-----------

Chapter 4

Non-isothermal flow in a rotating duct	74
4.1 Introduction	74
4.2 Governing Equations	76
4.3 Results and Discussion	81
4.4 Conclusions	89

References	110
-------------------	------------

Chapter 5	
Conclusions and Recommendations	112
References	115

List of Tables

2.1	Values of dimensionless mean velocity at various Ro numbers for $Ek = 0.01$	24
3.1	Numerical sensitivity tests ($\gamma = 1.0$, $Ek = 0.01$, and $\phi = 0^\circ$).	61
3.2	Computed singular points ($\gamma = 1.0$, $Ek = 0.01$, and $\phi = 0^\circ$) for 17×17	61

List of Figures

1.1	Types of bifurcations	9
2.1	(a) Geometry and coordinate system (b) grid layout	25
2.2	State diagram for the flow through straight, rotating pipe at $Ek = 0.01$. Variation of (a) transversal and (b) axial velocity with Rossby number at the monitor point ($x = -0.75, y = 0$)	26
2.3	Production of four-cell secondary flow by perturbing a two-cell flow symmetrically at $Ro = 10$. Transient solution at $Ek = 0.01$. (a) transversal velocity component, (b) secondary flow before and after a symmetric perturbation (c) axial velocity component	27
2.4	Axial velocity profile across the line of symmetry at $Ro = 10$ for two-cell and four-cell secondary flows.	28
2.5	Response to a symmetric perturbation of a two-cell secondary flow at $Ro = 2$. (a) Time series plot for transversal velocity, (b) secondary flow before and after a symmetric perturbation and (c) axial velocity	29
2.6	Response to an asymmetric perturbation of a two-cell secondary flow at $Ro = 2$. (a) Time series plot for transversal velocity, (b) secondary flow before and after an asymmetric perturbation and (c) axial velocity	30
2.7	Response to a symmetric perturbation of four-cell secondary flow at $Ro = 10$. (a) Time series plot for transversal velocity, (b) secondary flow before and after perturbation and (c) axial velocity	31
2.8	Response to an asymmetric perturbation of a four-cell secondary flow at $Ro = 10$. (a) Time series plot for transversal velocity, (b) secondary flow before and after perturbation and (c) axial velocity	32

2.9	Snap shots of contours of axial velocity and vectors of secondary velocity when a four-cell flow is subject to an asymmetric perturbation at $Ro = 10$	33
2.10	Response to a general asymmetric perturbation of a four-cell secondary flow at $Ro = 10$. Figure shows the effect of amplitude of perturbation. (a) Time series plot for transversal velocity and (b) axial velocity	34
2.11	Snap shots of contours of axial velocity when a four-cell flow is subject to a general asymmetric perturbation at $Ro = 10$. The amplitude of perturbation $\epsilon = 0.5V_{max}$	35
3.1	Geometry and coordinate system	62
3.2	This figure shows the asymptotic limit of slow rotation for $Ek = 0.1, \gamma = 1.0, \phi = 0^\circ, Ro = 10^{-4}$	63
3.3	This figure shows the asymptotic limit of rapid rotation for $Ek = 0.001, \gamma = 1.0, \phi = 0^\circ, Ro = 10^{-4}$	64
3.4	State diagram shows dimensionless flow rate vs. Rossby number at $Ek = 0.01, \gamma = 1.0, \phi = 0^\circ$	65
3.5	State diagram shows dimensionless stream function at $x = -0.45$ and $y = 0.05$ vs. Rossby number at $Ek = 0.01, \gamma = 1.0, \phi = 0^\circ$	66
3.6	State diagram shows dimensionless streamwise velocity at $x = -0.45$ and $y = 0.05$ vs. Rossby number at $Ek = 0.01, \gamma = 1.0, \phi = 0^\circ$	67
3.7	Three solutions are present on the primary branch PM at $Ro = 1.3$ and $Ek = 0.01, \gamma = 1.0, \phi = 0^\circ$. These three solutions are on the primary branch originating from $Ro = 0$, intermediate branch connecting $L1$ and $L2$ and after turning around $L1$ respectively. . . .	68
3.8	Three symmetric are solutions present at $Ro = 5.0$ and $Ek = 0.01, \gamma = 1.0, \phi = 0^\circ$. These correspond to <i>point 1</i> , <i>point 2</i> and <i>point 3</i> in the state diagram, Figure 3.6.	69
3.9	Two two-cell asymmetric solutions present at $Ro = 5.0$ and $Ek = 0.01, \gamma = 1.0, \phi = 0^\circ$. These correspond to <i>point 4</i> and <i>point 5</i> in the state diagram, Figure 3.6.	70

3.10	Two four-cell asymmetric solutions present at $Ro = 5.0$ and $Ek = 0.01, \gamma = 1.0, \phi = 0^\circ$. These correspond to <i>point 6</i> and <i>point 7</i> in the state diagram, Figure 3.6.	71
4.1	Geometry and coordinate system	90
4.2	This figure shows the contours of streamline with increasing Gr for $\phi = 0, \gamma = 1, \eta = 0.001, Pr = 0.707, Ek = 0.01, Ro = 0.1$	91
4.3	This figure shows the isotherms with increasing Gr for $\phi = 0, \gamma = 1, \eta = 0.001, Pr = 0.707, Ek = 0.01, Ro = 0.1$	92
4.4	This figure shows the contours of streamwise velocity with increasing Gr for $\phi = 0, \gamma = 1, \eta = 0.001, Pr = 0.707, Ek = 0.01, Ro = 0.1$	93
4.5	State diagram shows how the solution structure unfolds in the presence of non-isothermal effects for $\phi = 0, \gamma = 1, Gr = 1000, Pr = 0.707, Ek = 0.01$. Q vs. Ro for (a)isothermal case, (b)heating with $\eta = 0.001$ and (c) cooling with $\eta = -0.001$	94
4.6	State diagram shows how the solution structure unfolds in the presence of non-isothermal effects for $\phi = 0, \gamma = 1, Gr = 1000, Pr = 0.707, Ek = 0.01$. $w(-0.45, 0.05)$ vs. Ro for (a) isothermal case, (b)heating with $\eta = 0.001$ and (c) cooling with $\eta = -0.001$	95
4.7	State diagram shows how the solution structure unfolds in the presence of non-isothermal effects for $\phi = 0, \gamma = 1, Gr = 1000, Pr = 0.707, Ek = 0.01$. $\psi(-0.45, 0.05)$ vs. Ro for (a)isothermal case, (b)heating with $\eta = 0.001$ and (c) cooling with $\eta = -0.001$	96
4.8	Streamline contours for seven solutions present at $Ro = 5$ for $\phi = 0, \gamma = 1, \eta = 0.001, Gr = 1000, Pr = 0.707, Ek = 0.01$. Points refer to the labels on Figure 4.6(b).	97
4.9	Streamwise velocity perspectives for seven solutions present at $Ro = 5$ for $\phi = 0, \gamma = 1, \eta = 0.001, Gr = 1000, Pr = 0.707, Ek = 0.01$. Points refer to the labels on Figure 4.6(b).	98
4.10	Isotherms for seven solutions present at $Ro = 5$ for $\phi = 0, \gamma = 1, \eta = 0.001, Gr = 1000, Pr = 0.707, Ek = 0.01$. Points refer to the labels on Figure 4.6(b).	99
4.11	State diagram shows how the solution structure unfolds in the presence of non-isothermal effects for $\phi = 0, \gamma = 1, \eta = 0.001, Gr = 10^6, Pr = 0.707, Ek = 0.01$. (a) Q vs. Ro and (b) Q vs. Gr	100

4.12	State diagram shows how the solution structure unfolds in the presence of non-isothermal effects for $\phi = 0, \gamma = 1, \eta = 0.001, Gv = 10^6, Pr = 0.707, Ek = 0.01$. (a) fRe vs. Ro and (b) fRe vs. Gr	101
4.13	State diagram shows how the solution structure unfolds in the presence of non-isothermal effects for $\phi = 0, \gamma = 1, \eta = 0.001, Gv = 10^6, Pr = 0.707, Ek = 0.01$. (a) Nu vs. Ro and (b) Nu vs. Gr	102
4.14	State diagram shows how the solution structure unfolds in the presence of non-isothermal effects for $\phi = 0, \gamma = 1, \eta = 0.001, Gv = 10^6, Pr = 0.707, Ek = 0.01$. (a) $w(-0.45, 0.05)$ vs. Ro and (b) $w(-0.45, 0.05)$ vs. Gr	103
4.15	State diagram shows how the solution structure unfolds in the presence of non-isothermal effects for $\phi = 0, \gamma = 1, \eta = 0.001, Gv = 10^6, Pr = 0.707, Ek = 0.01$. (a) $\psi(-0.45, 0.05)$ vs. Ro and (b) $\psi(-0.45, 0.05)$ vs. Gr	104
4.16	Streamline contours for seven solutions present at $Ro = 5$ for $\phi = 0, \gamma = 1, \eta = 0.001, Gv = 10^6, Pr = 0.707, Ek = 0.01$. Points refer to the labels on Figure 4.14(a).	105
4.17	Streamwise velocity perspectives for seven solutions present at $Ro = 5$ for $\phi = 0, \gamma = 1, \eta = 0.001, Gv = 10^6, Pr = 0.707, Ek = 0.01$. Points refer to the labels on Figure 4.14(a).	106
4.18	Isotherms for seven solutions present at $Ro = 5$ for $\phi = 0, \gamma = 1, \eta = 0.001, Gv = 10^6, Pr = 0.707, Ek = 0.01$. Points refer to the labels on Figure 4.14(a).	107
4.19	Unfolding of $SB1$ for $\phi = 0, \gamma = 1, \eta = 0.001, Pr = 0.707, Ek = 0.01$ with heating.	108
4.20	Unfolding of $SB1$ for $\phi = 0, \gamma = 1, \eta = 0.001, Pr = 0.707, Ek = 0.01$ with increasing $Gv = 1000, 2000, 3000, 4000$, and 5000 . (a) $w(-0.45, 0.05)$ vs. Ro and (b) $\psi(-0.45, 0.05)$ vs. Ro	109

Nomenclature

a	width of the duct	(m)
b	height of the duct	(m)
\mathbf{a}	acceleration vector	(m/s^2)
C_{mn}^u	expansion coefficients for velocity	(-)
C_{mn}^ψ	expansion coefficients for stream function	(-)
C_{mn}^θ	expansion coefficients for temperature	(-)
c_p	specific heat	(J/kgK)
D	diameter of the pipe	(m)
Ek	Ekman number, $\nu/D^2\Omega(\text{pipe})$ or $\nu/b^2\Omega$	(-)
fRe	Frictional coefficient	(-)
f_u	Jacobian	(-)
f_p	$\partial f/\partial p$	(-)
g	acceleration due to gravity	(m^2/s)
Gv	Gravity number, gb^3/ν^2	(-)
\mathbf{h}	right null vector	(-)
k	thermal conductivity	(J/msK)
Nu	Nusselt number	(-)
Pr	Prandtl number, $c_p\mu/k$	(-)
R	domain of computation	

Ro	Rossby number, $U/D\Omega(\text{pipe})$ or $U/b\Omega$	(-)
r	position vector	(m)
Gr	Grashoff number	(-)
Q_l	heat transfer rate per unit length	(W/m ³)
s	arclength parameter	(-)
S	symmetric matrix	
t	time	(-)
τ	time	(-)
T_l	Chebyshev polynomials of order l	(-)
u, v, w	velocity component in x,y and z directions	(-)
U	velocity	(-)
v	velocity vector	(m/s)
w_1, w_2	weights	(-)
X^u	expansion functions for velocity	(-)
X^ψ	expansion functions for stream function	(-)
X^θ	expansion functions for temperature	(-)
x, y, z	coordinate axes	(-)
\tilde{x}, \tilde{y}	axes for Chebyshev domain	(-)
<i>Greek</i>		
∇	gradient operator	
∇^2	Laplacian operator	
α	component of parameter space, p	(-)
β	coefficient of thermal expansion	(1/K ²)
Ω	angular velocity	(s ⁻¹)
$\mathbf{\Omega}$	angular velocity vector	(s ⁻¹)
ψ	vorticity	(-)

μ	dynamic viscosity	(kg/ms)
ν	kinematic viscosity	(m^2/s)
ψ	stream function	$(-)$
ρ	density	(kg/m^3)
θ	temperature	$(-)$
ϕ	angle of tilt	$(-)$
γ	aspect ration b/a	$(-)$
η	$\beta\Delta\hat{\theta}$	$(-)$
ϵ	amplitude of perturbation	$(-)$
Ψ	potential	$(-)$

Subscripts, superscripts and other symbols

a	antisymmetric property
b	bulk quantity
s	symmetric property
\sim	dimensional quantity
r	reference quantity
$\langle \rangle$	averaged quantity

Chapter 1

Introduction

1.1 Transitions in fluid flow

There are many references in fluid mechanics where flow transitions take place whenever there is an imbalance among the forces governing the physics of flow. For example, when the flow rate in a pipe is increased beyond a certain critical value, the well defined motion of the fluid in parallel layers breaks up into irregular motion and spreads throughout the cross-section of the pipe, indicating the presence of macroscopic mixing motions perpendicular to the direction of the flow. Such a transition from laminar to turbulent flow is an example of a qualitative change in the flow structure. This kind of transition occurs over a range of Reynold numbers due to the relative balance between the convective inertial and viscous forces. Similar qualitative changes in the flow structure are observed in other problems in fluid flow. In the Rayleigh-Bénard problem, convection cells are observed due to an onset of instability in a layer of fluid heated from below. Such a qualitative change is due to a thermal instability that occurs when the adverse temperature gradient is large enough to make the Rayleigh number (the ratio of the destabilizing effect of

buoyancy force to the stabilizing effect of viscous force), increase above a critical value. The instability in flow between two rotating cylinders, called the Taylor-Couette problem, has many similarities to Rayleigh-Bénard problem. In the Bénard problem, there is a potentially unstable arrangement of an "adverse" temperature gradient. In the Couette flow problem the source of instability is the adverse gradient of angular momentum. Whereas convection in a heated layer is induced by buoyant forces becoming large enough to overcome the viscous resistance, the convection in Couette flow is generated by the centrifugal forces which overcome the viscous forces. These qualitative changes are characterised by the Taylor number. The instability appears in the form of counter-rotating toroidal vortices, called Taylor vortices. These vortices themselves become unstable at even higher values of Taylor number. Phenomena analogous to the Taylor vortices are called secondary flows, because they are superposed on a primary flow, such as the Couette flow. The possibility of secondary flows signifies that the solutions of the Navier-Stokes equations are nonunique, in the sense that more than one steady solution is allowed under the same boundary conditions. There are other situations where the combination of centrifugal and viscous forces result in instability and steady secondary flows in the form of vortices. Flow in a curved duct, the Dean problem, and boundary layer flow along a concave wall, the Görtler problem, also belong to the class of problems where centrifugal instability brings about qualitative changes in the flow and solution structures.

1.2 Bifurcation phenomena

It is interesting to observe from the discussion in the preceding section that whenever there is an imbalance among the forces driving the fluid flow, a qualitative

change occurs in the system. Such changes may often be described by a parameter or group of parameters that signify the relative magnitude of the forces involved. A bifurcation occurs where the solutions of a nonlinear system change their qualitative character as a parameter changes. In particular, bifurcation theory is about how the number of steady solutions of a system depends on parameters. A diagram illustrating the change in number of solutions with a change of a parameter is called a bifurcation diagram and a point with respect to parameter in the bifurcation diagram where the number of solution changes is called a branch point. Figure 1.1 illustrates a few types of bifurcations. Figure 1.1(a) shows a limit point, also known as a turning point, which is a one-sided bifurcation in the sense that solution comes from one side and turns around. At the limit point either two solutions are born or annihilate each other. Figure 1.1(b) shows a pitchfork bifurcation where two branches intersect and one of them is one-sided. This is a generic bifurcation in the sense that it breaks down in the presence of an imperfection to either one of the bifurcations shown in its left and right in Figure 1.1(b). Whenever the two solution branches intersect and none of them is one sided, transcritical bifurcation occurs, as shown in Figure 1.1(c). An exchange of stability occurs at a transcritical bifurcation point. A bifurcation which connects equilibria to periodic solution is called a Hopf bifurcation. Because the periodic solution is approached by other solutions in the limit of infinite time, such a solution is also called a limit cycle as shown in Figure 1.1(d). The essence of a transcritical bifurcation and a pitchfork bifurcation is that the real eigenvalue of the unique least stable mode increases through zero and one or two new steady solutions arise. In contrast, for a Hopf bifurcation, the real part of a pair of eigenvalues of the least stable complex conjugate modes increases through zero and a time-periodic solution arises. At a hysteresis or cusp bifurcation two limit points coalesce. This type of bifurcation usually occurs in a multiparameter study where the change of another parameter may bring two limit points near to each other and a further

change may bring about hysteresis or cusp bifurcation as shown in Figure 1.1(c). Within the cusp region there are three solutions and outside this region only one solution exists. As said above, these bifurcations spell qualitative changes brought about by the body forces. An important body force which occurs due to system rotation is the Coriolis force. The origin of this force is described in the next section.

1.3 Motion in a rotating frame

There are many engineering applications involving fluid flow and heat transfer in rotating ducts. They are used in turbomachinery, cooling systems of gas turbine blades and conductors of electric generators, motors, and various cooling systems for rotating components, notably prime movers.

In order to study hydrodynamics, we need governing equations describing the fluid flow. Newton's second law of motion relates the resultant force acting on a body to the change in momentum experienced by the body. However, for this law to be valid it is necessary to ensure that the motion concerned is referred to an inertial frame of reference, a reference frame which is either stationary in space or moving with uniform velocity. For example, if the motion of a fluid particle moving inside a stationary duct is required, a convenient reference frame is fixed in relation to the duct itself. Because the duct is stationary such a reference frame will be inertial and Newton's second law of motion may be used to describe the motion of the particle. However, if the duct is rotating and/or translating, a reference frame fixed to the duct is no longer inertial. Under these circumstances correction terms must be applied to the Newton's second law in order to maintain its applicability in a non-inertial frame of reference. If the rotating frame is translating with velocity \mathbf{v}_0 and rotating with a angular velocity Ω then the velocity, \mathbf{v} and acceleration, \mathbf{a} ,

of particle in the inertial frame can be represented as (Morris, 1981),

$$\mathbf{v} = \frac{\partial \mathbf{r}}{\partial t} + \boldsymbol{\Omega} \times \mathbf{r} + \mathbf{v}_o \quad (1.1)$$

$$\mathbf{a} = \frac{\partial^2 \mathbf{r}}{\partial t^2} + 2 \left[\boldsymbol{\Omega} \times \frac{\partial \mathbf{r}}{\partial t} \right] + [\boldsymbol{\Omega} \times (\boldsymbol{\Omega} \times \mathbf{r})] + \left[\frac{\partial \boldsymbol{\Omega}}{\partial t} \times \mathbf{r} \right] + \mathbf{a}_o \quad (1.2)$$

where, \mathbf{r} represents the position vector in rotating frame.

In the equation (1.2), $\frac{\partial^2 \mathbf{r}}{\partial t^2}$ represents acceleration with respect to the non-inertial frame of reference. The expressions, $2 \left[\boldsymbol{\Omega} \times \frac{\partial \mathbf{r}}{\partial t} \right]$, and $[\boldsymbol{\Omega} \times (\boldsymbol{\Omega} \times \mathbf{r})]$ are known as the Coriolis acceleration and the centripetal acceleration respectively. The expression, $\left[\frac{\partial \boldsymbol{\Omega}}{\partial t} \times \mathbf{r} \right]$, accounts for the angular acceleration of the frame. This occurs whenever the reference is rotating with non-uniform angular velocity (start up or spin up). Finally, the last term, \mathbf{a}_o , in equation (1.2) occurs if the origin has acceleration with respect to the inertial frame.

These additional correction terms of acceleration affect the path of a particle in a rotating system significantly. In the next section, we study the effect of these forces in generating vorticity in fluid.

1.4 Creation of Vorticity by Coriolis and Buoyancy Forces

Vorticity is a measure of the angular velocity which a particle of fluid has at a point in the flow. It can be defined as:

$$\boldsymbol{\xi} = \nabla \times \mathbf{v} \quad (1.3)$$

By taking curl of momentum equations, we get vorticity transport equation that governs the manner in which vorticity is generated, convected and diffused through a

moving fluid. For the motion in an inertial frame of reference, the vorticity equation takes the following form:

$$\frac{D\xi}{Dt} = (\xi \cdot \nabla) \mathbf{v} + \nu \nabla^2 \xi \quad (1.4)$$

For a non-inertial frame, additional terms appear because of correction terms to the momentum equations. By assuming that the centripetal and translational acceleration of the origin combine to form a conservative field which can be described by a scalar function ϕ such that

$$\nabla \phi = \boldsymbol{\Omega} \times (\boldsymbol{\Omega} \times \mathbf{r}) + \mathbf{a}_0 \quad (1.5)$$

we get the following momentum equation:

$$\frac{D\mathbf{v}}{Dt} + 2(\boldsymbol{\Omega} \times \mathbf{v}) = -\nabla \left(\frac{p}{\rho} + \phi \right) + \nu \nabla^2 \mathbf{v} \quad (1.6)$$

By taking curl of the equation(1.6), we get the following vorticity equation for non-inertial frame:

$$\frac{D\xi}{Dt} = (\xi \cdot \nabla) \mathbf{v} + \nu \nabla^2 \xi + 2(\boldsymbol{\Omega} \cdot \nabla) \mathbf{v} \quad (1.7)$$

In equations(1.4) and (1.7), vorticity is generated by the term $(\xi \cdot \nabla) \mathbf{v}$ and subsequently convected and diffused through the flow by means of the terms $\frac{D\xi}{Dt}$ and $\nu \nabla^2 \xi$ respectively. In rotating frame of reference the non-zero value of $2(\boldsymbol{\Omega} \cdot \nabla) \mathbf{v}$ is responsible for generating vorticity. Thus, Coriolis acceleration can generate secondary flows in planes perpendicular to the main directions of the flow for rotating ducts. This could significantly affect resistance to flow and convective heat transfer inside the duct.

For constant property flow, the conservative combination of the centripetal acceleration and translational acceleration of the origin is hydrostatic in nature. In other words they do not contribute to the generation of vorticity. For a non-isothermal flow, density varies with temperature via an equation of state having the

form

$$\rho = \rho_r[1 - \beta(\theta - \theta_r)] \quad (1.8)$$

where ρ_r density of the fluid at a specified reference temperature θ_r , and β is the coefficient of cubical expansion. Thus, the momentum equations take the following form,

$$\frac{D\mathbf{v}}{Dt} + 2(\boldsymbol{\Omega} \times \mathbf{v}) = -\frac{1}{\rho_r}\nabla p' + \beta(\theta - \theta_r)\nabla\phi + \nu\nabla^2\mathbf{v} \quad (1.9)$$

By taking curl of equation(1.9) we get following vorticity equation:

$$\frac{D\xi}{Dt} = (\xi \cdot \nabla)\mathbf{v} + \nu\nabla^2\xi + 2(\boldsymbol{\Omega} \cdot \nabla)\mathbf{v} + \nabla \times [\beta(\theta - \theta_r)\nabla\phi] \quad (1.10)$$

Equation(1.10) permits the following observations for a nonisothermal flow through a rotating duct. The Coriolis acceleration generates vorticity as was shown earlier and temperature-induced density variations do not directly affect this term to a first approximation. The conservative effective body force field described by the scalar function ϕ can create vorticity via a temperature density interaction. Thus, in a non-isothermal rotating duct the flow field will be simultaneously influenced by Coriolis acceleration and a buoyancy force. When these forces interact with the inertial and viscous forces interesting flow structures appear. For some values of parameters describing the interaction of the forces involved multiple solutions exist. These solutions are represented by using convenient state functions in a bifurcation diagram. In the following chapters we study bifurcation structures of isothermal and non-isothermal flow through a straight rotating duct.

1.5 Organization of Thesis

The present study has been divided into five chapters of which the present one is the Introduction.

In Chapter 1, some discussion of the problems in fluid flow where bifurcation occurs is presented. The basic types of bifurcations are introduced which are common in the presence of body forces. The concept of Coriolis force due to system rotation and the effect of Coriolis and buoyancy forces in the generation of vortices is presented. Finally an outline of the thesis is presented.

In Chapter 2, we investigate multiple solutions of flow in a straight pipe that is rotating about the axis perpendicular to the pipe axis. The governing equations are solved using control volume approach. In this problem we analyse the existence of multiple solutions and their stability to symmetric and asymmetric perturbations. The main focus of this study is to get a hitherto unknown four-cell solution.

In Chapter 3, a bifurcation study of isothermal flow in a straight rotating duct of rectangular cross-section is examined. In this study spectral approximation techniques are used to discretize equations and arclength continuation schemes are used to track the solution path. Two new solutions through a pitchfork bifurcation are discovered.

The nonlinear coupling between the momentum and energy equation in the presence of system rotation results in a complex bifurcation structure. In particular the presence of a buoyancy force breaks the symmetry in the problem of isothermal flow in a straight rotating duct. This results in a smooth unfolding of symmetry breaking bifurcation points. The focus of Chapter 4 is to study such unfolding for the bifurcation diagram obtained in Chapter 3.

Finally, in Chapter 5, the main conclusions are presented along with some recommendations for future work.

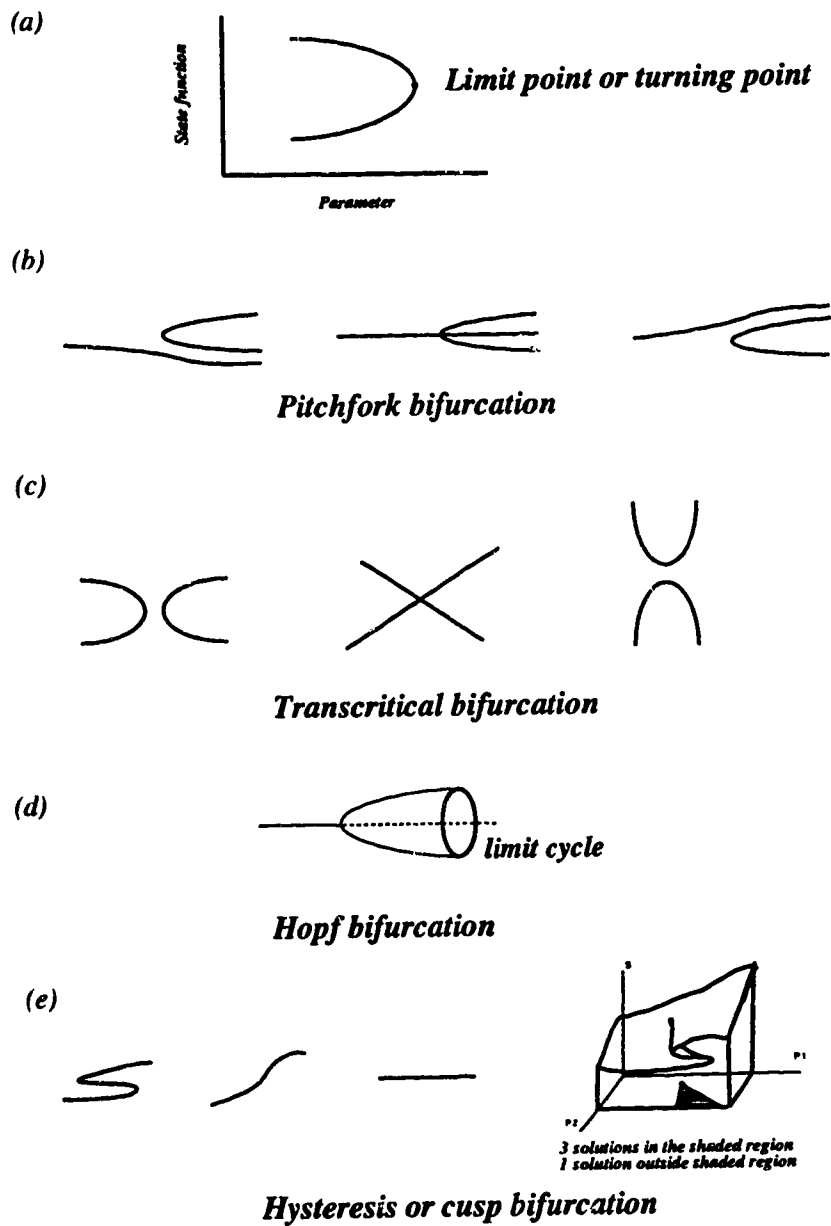


Figure 1.1: Types of bifurcations

References

MORRIS, W.D. 1981. *Heat Transfer and Fluid Flow in Rotating Coolant Channels*.
Research Studies Press, John Wiley and Sons.

Chapter 2

Flow through a rotating pipe

2.1 Introduction

Laminar flow in rotating ducts (rectangular cross section) and pipes (circular cross section) has been studied extensively from both theoretical and experimental points of view. The flow in a rotating duct/pipe has many practical applications in rotating machinery ((Debruge & L.S.Han, 1972); (Walker, 1975)) and in instruments that measure flow rates based on the Coriolis effect (Raszillier & Durst, 1991). Hydrodynamic stability aspects of flows in a rotating frame are equally important and have been a subject of investigation by many authors. The presence of a Coriolis force due to the system rotation makes governing differential equations nonlinear and intractable by analytical means; but it is also responsible for very interesting and complex changes in the flow and solution structure. The presence of a Coriolis force introduces transverse differential pressure gradients which modifies the primary Hagen-Poiseuille flow under axial pressure gradient. A region of higher pressure is formed in a direction opposite to the Coriolis acceleration. Slow moving fluid near the upper and lower surfaces of the duct gains momentum as it flows from the

high pressure to the low pressure region. Because the flow is confined, the fast moving fluid moves back to the high pressure region through the central core. This establishes a mechanism for secondary flow, which is typically a two-dimensional flow consisting of two counter-rotating vortices in the plane perpendicular to the flow direction. The interaction of the secondary flow with the pressure driven primary flow causes a shift in the location of the maximum axial velocity from the center of the duct toward the high pressure wall of the duct.

The relative importance of the forces that govern the flow structure in flow through rotating duct/pipe can be characterized by two dynamical parameters - *viz.*, the Ekman number, Ek , represents the ratio of viscous to Coriolis force and the Rossby number, Ro , represent the ratio of inertial to Coriolis force. Other forms of dynamical parameters in terms of Reynolds number and rotational number have also been used in literature. See Figure 2.1 for definitions and scales.

The flow in a rotating straight duct/pipe is qualitatively similar to the flow in stationary curved duct/pipe. The role of centrifugal force in a curved pipe is the same that of the Coriolis force in a straight rotating pipe in generating and sustaining the secondary flow. While this similarity between these two flows has been recognized by numerous authors, it is interesting that the multiplicity features of flow in a rotating straight pipe have not been investigated to date. Instead the focus has been on the enhancement of heat and mass transfer effects due to the presence of secondary flow. The centrifugal and Coriolis forces are also responsible for the interesting and rich solution structure of two-dimensional flows in these classes of problems. Historically, there has been a strong parallel between the studies on flow through stationary curved pipes and rotating straight pipes, with the later lagging behind by several years.

The earliest work on flow in a rotating straight pipe was inspired by Dean's (1927;

1928) work on stationary curved pipes. It was carried out for the asymptotic limits of weak and strong rotations by Barua(1954) and Benton(1956) using a perturbation expansion on the Hagen-Poiseuille flow. They found a two-cell secondary flow structure similar to the Dean(1927; 1928) study for stationary curved pipe flow. The studies of Mori & Nakayama(1968), and Ito & Nanbu(1971) for small rotational speeds and high axial pressure gradient resulted a good agreement with experiments, showing an increase in friction factor with rotational speed. At the other extreme of the asymptotic limit, Benton(1966) considered the flow through a rapidly rotating channel. He showed that viscous effects are important only in a thin boundary layer along the channel walls and in the interior, where the nonlinear acceleration and viscous terms in the Navier-Stokes equations can be neglected with respect to the Coriolis term, the flow is geostrophic. In this region the cross flow is constant throughout. This flow is similar to the flow in stationary curved duct for high Dean numbers as observed by Barua(1963).

Inspired by Van Dyke's(1978) work on the Dean problem, Mansour(1985) used the computer extended Stokes series approach for extending the results of Barua(1963) for flow in a rotating straight pipe in the double limit of $Ek \rightarrow \infty$, $(Ro/Ek) \rightarrow \infty$, and $(Ro/Ek^2) = \text{constant}$. When the forces are of comparable magnitude a complex flow structure results that can be unraveled only by numerical means as recognized by Duck(1983). None of these studies reveal any multiple solutions for flow in a straight rotating pipe. The first numerical studies to reveal multiple solutions in the Dean problem were by Dennis & Ng(1982) and Nandakumar & Masliyah(1982). The only available numerical study on rotating straight pipe by Duck(1983) does not reveal such multiplicity features, although Duck recognized a strong parallel between flows in curved pipes and rotating pipes.

The flow in rotating straight ducts and stationary curved ducts of rectangular

geometry is fairly well understood. Winters(1987) has presented a definitive bifurcation study of laminar flow in a stationary curved duct of rectangular cross-section. He showed that four-cell flows are stable to symmetric perturbations, but unstable to asymmetric perturbations. Experimental and numerical investigation by Bara *et al.* (1992) showed that when perturbed asymmetrically, the four-cell flow might evolve to flows with sustained spatial oscillations farther downstream. In a numerical study of the flow in rotating, rectangular duct Speziale(1982) demonstrated that a transition from a two-cell to a four-cell flow structure occurs as Ro is changed. Nandakumar *et al.* (1991) examined the flow through the rotating rectangular duct. Their study confirmed the hysteresis behavior between the two- and four-cell flow structure by Khesghi & Scriven(1985). Further they found an additional branch that has a two-cell flow structure at one end, and a four-cell flow structure at the other with three limit points on the path.

For fully developed flow in a curved pipe of circular cross-section, the numerical studies of Nandakumar & Masliyah(1982), Dennis & Ng(1982), Yang & Keller(1986) and Daskopoulos & Lenhoff(1989) showed the existence of multiple solutions. The flow features in a rotating straight pipe of circular cross-section are not yet fully documented. Duck(1983) examined the flow through rotating straight pipes of a circular cross section using Fourier decomposition in the angular direction. However, due to the convergence difficulties of the iterative solution method used, no solutions at high Rossby numbers could be obtained. In particular a dual four-cell solution was not computed. Solution multiplicity is, however, expected since the equations governing the two-dimensional flows through rotating channels are analogous to those of laminar flow in coiled ducts(the Dean problem) in the double limit of $Ek \rightarrow \infty$, $(Ro/Ek) \rightarrow \infty$, and $(Ro/Ek^2) = \text{constant}$ as shown, for example, by Mansour(1985).

In the present work ¹ our objective has been a modest one of establishing dual solutions for the rotating flows just as was done by Nandakumar & Masliyah(1982) and Dennis & Ng(1982) for the Dean problem. We examine the multiplicity features and the secondary flow structure in the fully developed regime in a straight pipe of circular cross-section rotating about an axis perpendicular to the pipe axis. The present work can be considered a direct extension of the works Barua(1963), Mansour(1985) and Duck(1983). The numerical simulations reported in the present study establish the following features: (i) a primary two-cell solution branch is found at all values of Rossby numbers, which is in agreement with earlier works; (ii) above a certain critical Rossby number, additional solutions exhibiting four-cell flow structure that coexist with the two-cell flow structure are found; (iii) the four-cell flow solutions are unstable to asymmetric perturbation and stable to symmetric perturbation; (iv) unlike the two-dimensional, four-cell flow in a rectangular geometry which breaks down into a three-dimensional, streamwise periodic mode, the two-dimensional, four-cell flow in a circular geometry breaks down to a stable two-dimensional, two-cell flow over the range of Rossby numbers investigated here.

2.2 Governing Equations

The Navier-Stokes equations governing the two-dimensional flow in a rotating frame of reference are solved to study the flow through a rotating pipe. Two-dimensionality is imposed by assuming that the pipe is sufficiently long and that the flow is driven by a constant axial pressure gradient. The equations are

¹A version of this chapter has been accepted for publication in *Physics of Fluids*; presented in 47th Annual meeting of the Division of Fluid Dynamics, Atlanta, 1994

rendered dimensionless using D , diameter of pipe to scale the radial direction, $U = -(1/\rho\Omega D)\partial\Psi/\partial z$ to scale velocities, where Ψ is a potential that combines pressure, gravitational, and centrifugal forces, $\rho U D \Omega$ to scale pressure, and $1/\Omega$ to scale time. The dimensionless form of the equations of motion are given below.

continuity equation:

$$\frac{\partial u}{\partial x} + \frac{\partial v}{\partial y} = 0 \quad (2.1)$$

x-transversal momentum equation:

$$\frac{\partial u}{\partial t} + Ro(u \frac{\partial u}{\partial x} + v \frac{\partial u}{\partial y}) = -\frac{\partial \Psi}{\partial x} + Ek(\frac{\partial^2 u}{\partial x^2} + \frac{\partial^2 u}{\partial y^2}) - 2w \quad (2.2)$$

y-longitudinal momentum equation:

$$\frac{\partial v}{\partial t} + Ro(u \frac{\partial v}{\partial x} + v \frac{\partial v}{\partial y}) = -\frac{\partial \Psi}{\partial y} + Ek(\frac{\partial^2 v}{\partial x^2} + \frac{\partial^2 v}{\partial y^2}) \quad (2.3)$$

z-axial momentum equation:

$$\frac{\partial w}{\partial t} + Ro(u \frac{\partial w}{\partial x} + v \frac{\partial w}{\partial y}) = 1 + Ek(\frac{\partial^2 w}{\partial x^2} + \frac{\partial^2 w}{\partial y^2}) + 2u \quad (2.4)$$

2.3 Results and Discussion

The steady and transient forms of the governing equations of motion were discretized using the control volume method. The two-dimensional flow domain of a circular pipe in the physical space is mapped to body-fitted coordinates in computational space using curvilinear coordinate transformation. The discretized equations were solved using the SIMPLE algorithm. The transient simulations are carried out using the backward difference scheme in time domain. The simulations were carried out by keeping $Ek = 0.01$ fixed and varying Ro in the range of 0.01 to 20. It should be noted that higher values of $Ek = 0.1$ correspond to rectilinear flow where the viscous force overwhelms the Coriolis force. On the other hand,

lower values of $Ek = 0.001$ correspond to an Ekman boundary layer flow having its geostrophic core in the center of the duct. In this study we are mainly interested in the region where the viscous and the Coriolis forces compete with each other, leading to interesting multiplicity features. The flow geometry and coordinate axes are shown in Figure 2.1(a). The nonuniform grid shown in Figure 2.1(b) with total of 1350 elements was found to give adequate flow resolution. The adequacy of grid resolution was checked against the limiting one-dimensional flow in a circular pipe, using the mean velocity for Hagen-Poiseuille flow and fRe was calculated to be 16.03, which is within 0.2% of the analytical result. Grid sensitivity was also checked at non-zero Rossby numbers by taking 2700 elements and comparing detailed velocity profiles in regions where there are multiple solutions. These results will be presented later.

Two views of the state diagram are shown in Figures 2.2(a)- 2.2(b). The variation of transversal velocity, u , with Ro is represented in Figure 2.2(a). The monitor point for the transversal velocity, u , is on the line of symmetry ($x = -0.75, y = 0$) since any flow reversal is expected to occur in this region. The negative velocity component indicates that the secondary flow is pointing towards the axis of rotation. A unique two-cell flow solution is found for low values of Ro . This result is in agreement with the two-cell flow solution predicted by Duck(1983). In Figure 2.2(b), the axial velocity is used to represent the state of the solution as a function of Rossby number. As the strength of the secondary flow increases with increasing Ro , the axial velocity component decreases which is to be expected since the simulations were carried out at a fixed streamwise pressure gradient. The dimensionless mean velocities for the two-cell and the four-cell solution branches at various values of Ro are given in Table 2.1.

For centrifugally driven secondary flow in a curved pipe of circular cross-section

(the Dean problem) multiple solutions have been reported by Yang & Keller(1986) among others. While several limit points were found by Yang & Keller(1986) all of the limit points cannot be deemed real for the following reason. Except for the lowest limit point, below which a unique two-cell solution exists, all other limit points were found to be sensitive to grid refinement. Thus the question of whether they are spurious is left unresolved. Also, the reflective symmetry was imposed in the calculations, and hence symmetry breaking points and non-symmetric solutions were not computed. Similar questions remain to be answered for the flow in rotating pipes.

In order to observe dual solutions experimentally Bara *et al.* (1992) inserted a pin symmetrically, across part of the duct. The motivation behind this approach was to reduce the development length for the four-cell flow. If the pin did not cause a symmetric perturbation, then the fully developed symmetric four-cell flow could not be observed in their experiments. Inspired by this, in our current numerical experiments we simulate the insertion of pin by making the velocity zero at the grid points that lie on the axis of symmetry. This perturbation has been found to be adequate to make the solution to be attracted to a four-cell flow as long as the Rossby number is sufficiently large. Figures 2.3(a) and 2.3(c) show the transient evolution of the axial and transversal velocities at the monitor point when the flow is perturbed symmetrically at $Ro = 10$. As shown in Figure 2.3(a) and 2.3(c), the flow is perturbed at $t = 0.75$ by making velocity zero at that instant of time only. Prior to the perturbation, the transversal velocity component u in Figure 2.3(a) is negative, showing that secondary flow has a two-cell flow structure. But when the flow is perturbed at $t = 0.75$, the solution is attracted to the four-cell flow solution and steady state is reached within $t = 7$. The secondary flow reversal near the monitor point is clear in Figure 2.2(a), showing positive transversal velocity component for

four-cell flow once a steady state has been attained. This flow reversal is also evident in vector plots of two-cell and four-cell shown in Figure 2.3(b). Once the four-cell flow is obtained at $Ro = 10$, it was used as an initial guess for generating the solution at other values of Ro below and above $Ro = 10$, in order to trace the four-cell solution branch in Figure 2.2. When Ro was decreased to 2.61 the four-cell flow structure breaks down spontaneously to the two-cell flow structure. This point is identified as the limit point $L1$ in Figure 2.2. This limit point will be a function of the Ekman number.

From the earlier works of Kheshgi & Scriven(1985), Nandakumar *et al.* (1991), Winters(1987) and Yang & Keller(1986) it is clear that an intermediate branch connecting the two-cell and four-cell solution branches in Figure 2.2 must exist. It is also clear that the intermediate solution branch must be unstable. In our experience the SIMPLE algorithm is capable of converging only to those solutions that are also physically stable. This procedure is adequate to demonstrate the existence of four-cell flow solution for the rotating straight pipes. Thus, in our study, we do not find an unstable solution branch connecting the two-cell and four-cell branch, as reported by Yang & Keller(1986) for curved pipes.

Figure 2.4 shows the variation of the axial-velocity along the line of symmetry for both the two-cell and the four-cell flow solution at the same Rossby number of 10.0. Also shown in this figure are the results of grid refinement on the flow profiles. It is clear that both the two-cell and four-cell flows are captured adequately by 1350 and 2700 cells. Duck(1983) noted the departure from non-rotating case in terms of shift in the maximum axial velocity away from the pipe axis and towards the direction of the secondary flow. We also note the same phenomena, as shown in Figure 2.4. In addition to it, Figure 2.4 shows that for four-cell flow the magnitude of maximum axial velocity is less than the magnitude of maximum axial velocity

for two-cell flow. This is expected since additional vortices in four-cell generates more cross-flow. Also, note that for four-cell flow the maximum axial velocity shifts toward the axis. This happens because the additional vortices that develop in four-cell flow carry more fluid to the central core by their positive velocity component on the horizontal line of symmetry of pipe.

Two-cell flows are known to be stable in many geometries such as square and circular ducts. To determine the stability of the various steady-state solutions, a set of transient simulations were conducted under the conditions of imposed symmetry about the line($x,y=0$), and with out imposing symmetry. Also, the stability of the solutions were tested for both symmetric and asymmetric perturbations.

At $Ro = 2$ only a two-cell flow structure exists (Figure 2.2(a)) which is expected to be stable. To test the stability of the two-cell flow solution at $Ro = 2$, transient simulations were carried out. Figures 2.5(a) and 2.5(c) show the transient evolution of the velocities when a symmetric perturbation is applied to a well established, steady two-cell flow solution. These figures illustrate that within $t=3$, the perturbation dies out and stable two-cell flow solution is re-established. The vector diagrams before and after the application of the symmetric perturbation are shown in Figure 2.5(b). Similarly, Figures 2.6(a)-2.6(c) show that the unique two-cell flow solution at $Ro = 2$ is stable to asymmetric perturbation also. The four-cell flow solution is also found to be stable to symmetric perturbations as illustrated in Figures 2.7(a)-2.7(c). As shown in Figure 2.7(a) and 2.7(c) the perturbation dies out with in $t = 4$ and the steady state four-cell flow solution results.

The four-cell flows in curved ducts/pipes are know to be unstable to asymmetric perturbations. In order to investigate the expected instability of the four-cell flow solutions in a rotating pipe to such asymmetric perturbations, a transient simulation is performed subject to an asymmetric perturbation with out imposing

symmetry boundary conditions. The time series is shown in Figures 2.8(a)- 2.8(c) and the secondary flow structure is shown in Figure 2.8(b) both before and after the perturbation. It is clear that the four-cell secondary flow structure is destroyed and a steady, two-cell structure emerges.

The asymmetric perturbation of the four-cell flow solution causes a major disturbance in the flow pattern. When steady-state is achieved again, the flow pattern has stabilized to a symmetric, steady, two-cell flow pattern. It is interesting to observe transient states of the breakdown of four-cell to two-cell flow. Figure 2.9 shows the various intermediate transient states of the contour and vector diagrams when the asymmetric perturbation is applied to the four-cell flow. At $t = 0.05$, we have a steady, four-cell flow structure. When this four-cell flow solution is perturbed asymmetrically at $t=0.75$, it breaks down to a two-cell flow solution at $t = 3.5$ via an intermediate three-cell flow structure, which folds itself into a stable two-cell flow structure. In order to gain more insight into the effect of an asymmetric perturbation, varying degrees of asymmetry were imposed by using

$$V(r,\theta) = V_o(r,\theta) + \epsilon (1 - r^2) \sin \theta$$

where V is the velocity and ϵ , the amplitude of perturbation was varied. Figure 2.10 shows the effect of varying the degree of asymmetry on the breakdown of four-cell flow structure to two-cell flow structure. For both smaller ($\epsilon = 0.1V_{max}$) and larger ($\epsilon = 0.5V_{max}$) amplitudes of perturbation four-cell flow breaks down to two-cell flow. Figure 2.11 shows the snapshots of contours of axial velocity when the four-cell flow is subjected to a general perturbation of a amplitude of 50% of the maximum velocity. The four-cell solution is perturbed at $t = 0.75$ which quickly breaks down to a two-cell asymmetric solution structure which transforms into two-cell steady symmetric flow structure at $t = 3.5$.

It should be noted that this transient breakdown of four-cell to two-cell

flow structure is not experimentally realizable, since in any experiment there is a dominant, streamwise motion. Any asymmetric perturbations due to the imperfections in experimental apparatus would grow and eventually destabilize the four-cell flow. These are arbitrary perturbations as shown in Figure 2.10 and 2.11. On the other hand, though not realistic, the effect of asymmetric perturbation can easily be implemented by inserting a pin asymmetrically. Our present study is limited to the stability analysis of two-dimensional flows to two-dimensional perturbations. While the inference on the conditional stability of the two-dimensional, four-cell flow remains valid, in actual experiments the breakdown of the four-cell flow solution would occur spatially in the streamwise direction. A three-dimensional stability analysis is a natural extension to our present study.

Another interesting consequence of the conditional stability result for the four-cell flow is that there must exist a symmetry breaking point some where along the primary solution branch. A similar result of conditional stability of the four-cell flow in curved pipes also exists in the work of Yanase *et al.* (1988). Yet for both the curved pipe and rotating pipe problems, the complete bifurcation structure for the circular geometry remains to be mapped out using continuation methods and extended systems for locating the various singular points. Questions regarding grid independent results for the location of the singular points also remain.

2.4 Conclusion

Two-dimensional flows in rotating circular pipes are shown to exhibit multiple solutions above a certain critical value of the Rossby number. The primary solution branch that starts at very low values of the Rossby number exhibits a secondary flow structure with two-cells. Such flows have been previously computed by Duck(1983).

In addition a second solution branch has been found that corresponds to a secondary flow structure with four-cells. Such four-cell solutions are unstable to asymmetric perturbations, while two-cell solutions are stable to both symmetric and asymmetric perturbation.

Flow Structure	Ro	V_{mean}
Two-Cell	0.01	4.4711
	0.10	4.4512
	1.00	3.9819
	2.00	3.6618
	5.00	3.2491
	8.00	3.0227
	12.00	2.8342
	16.00	2.7069
	20.00	2.6076
Four-Cell	2.68	3.5676
	2.87	3.5320
	3.25	3.4701
	5.00	3.2646
	8.00	3.0418
	10.00	2.9363
	12.00	2.8521
	15.00	2.7479
	20.00	2.6178

Table 2.1: Values of dimensionless mean velocity at various Ro numbers for $Ek = 0.01$.

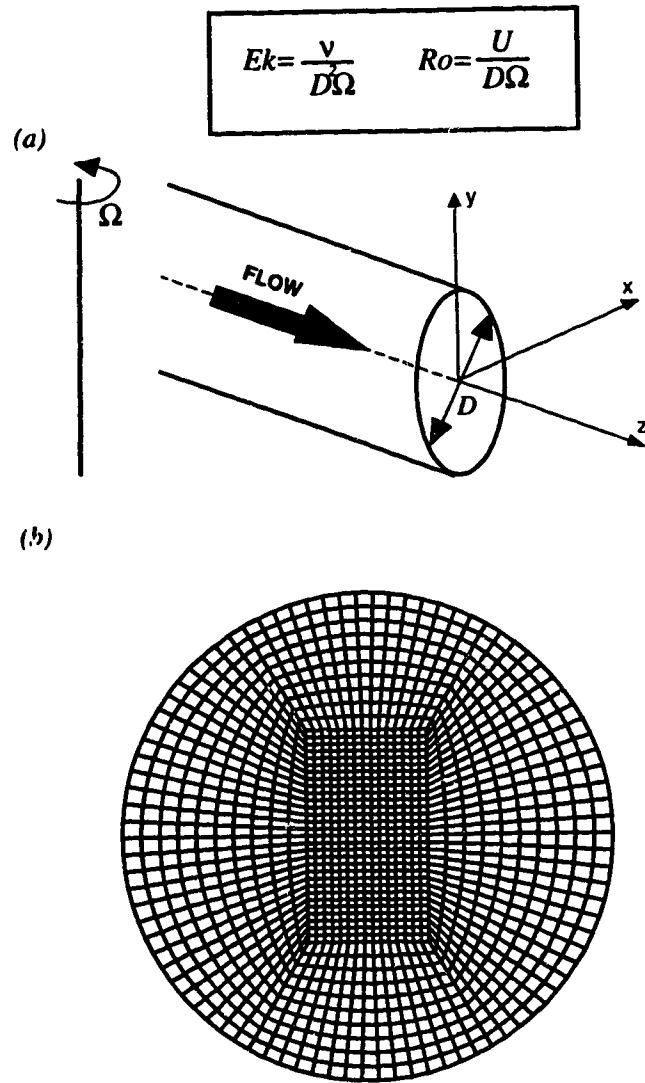


Figure 2.1: (a) Geometry and coordinate system (b) grid layout

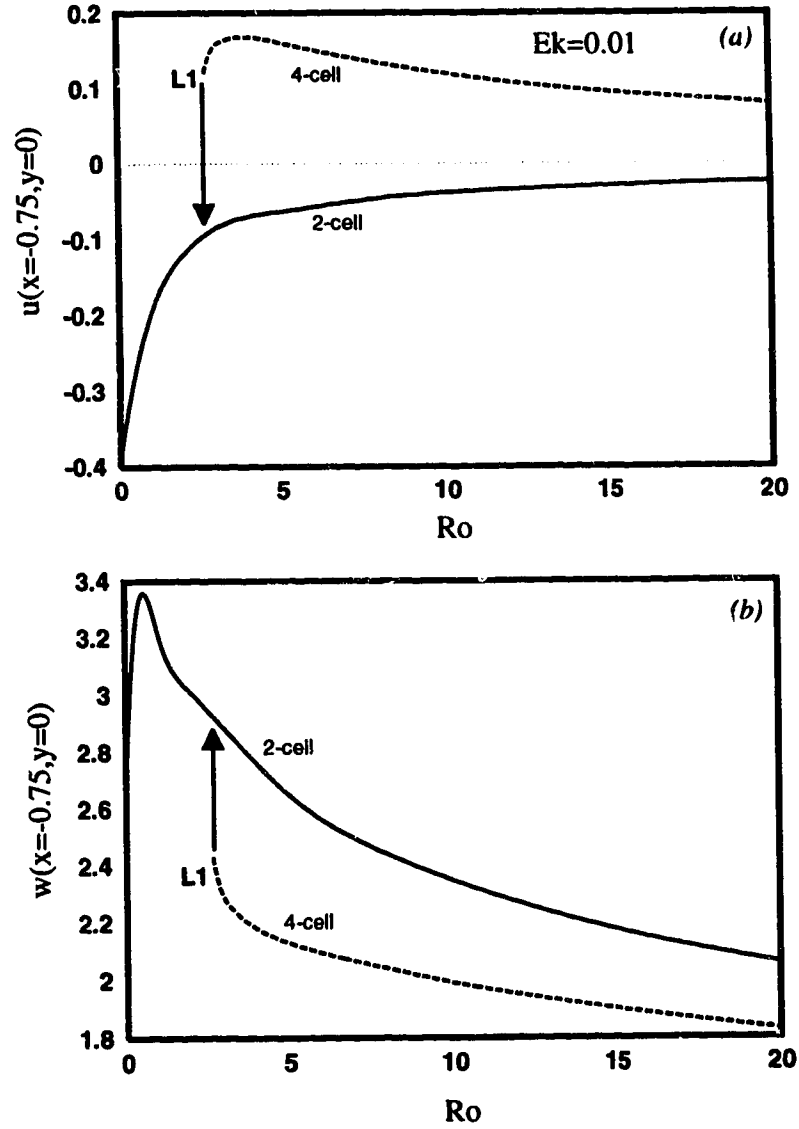


Figure 2.2: State diagram for the flow through straight, rotating pipe at $Ek = 0.01$. Variation of (a) transversal and (b) axial velocity with Rossby number at the monitor point $(x = -0.75, y = 0)$

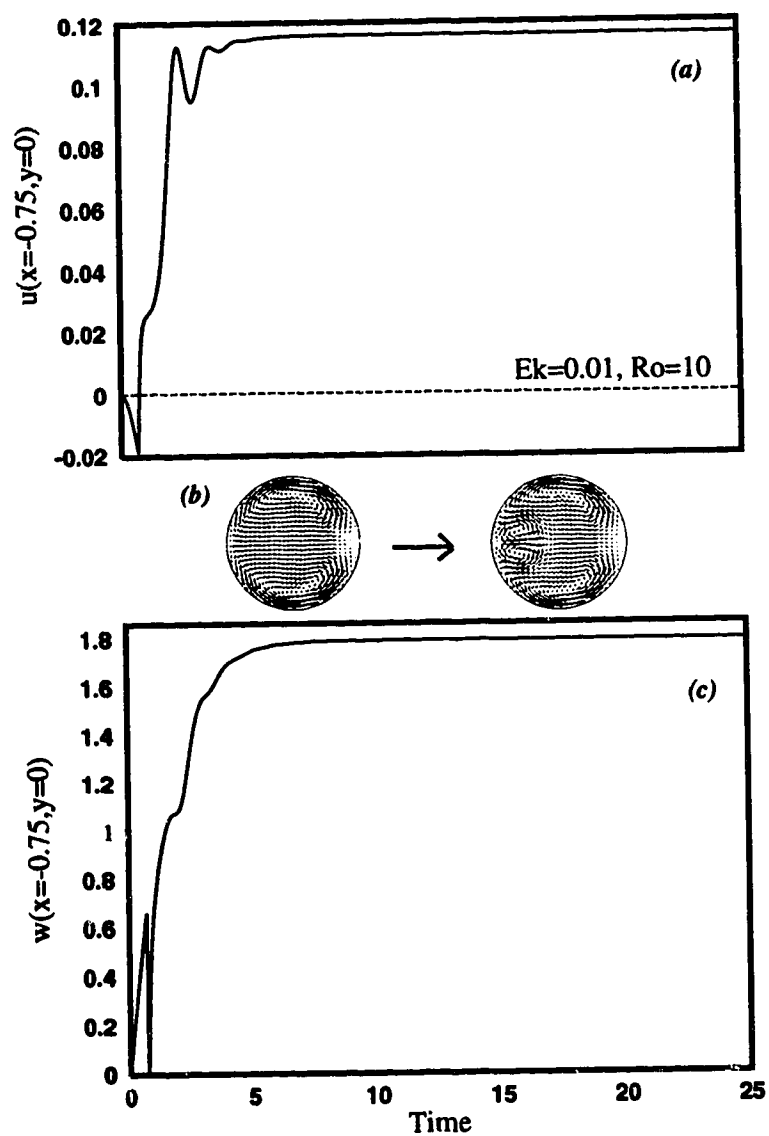


Figure 2.3: Production of four-cell secondary flow by perturbing a two-cell flow symmetrically at $Ro = 10$. Transient solution at $Ek = 0.01$. (a) transversal velocity component, (b) secondary flow before and after a symmetric perturbation (c) axial velocity component

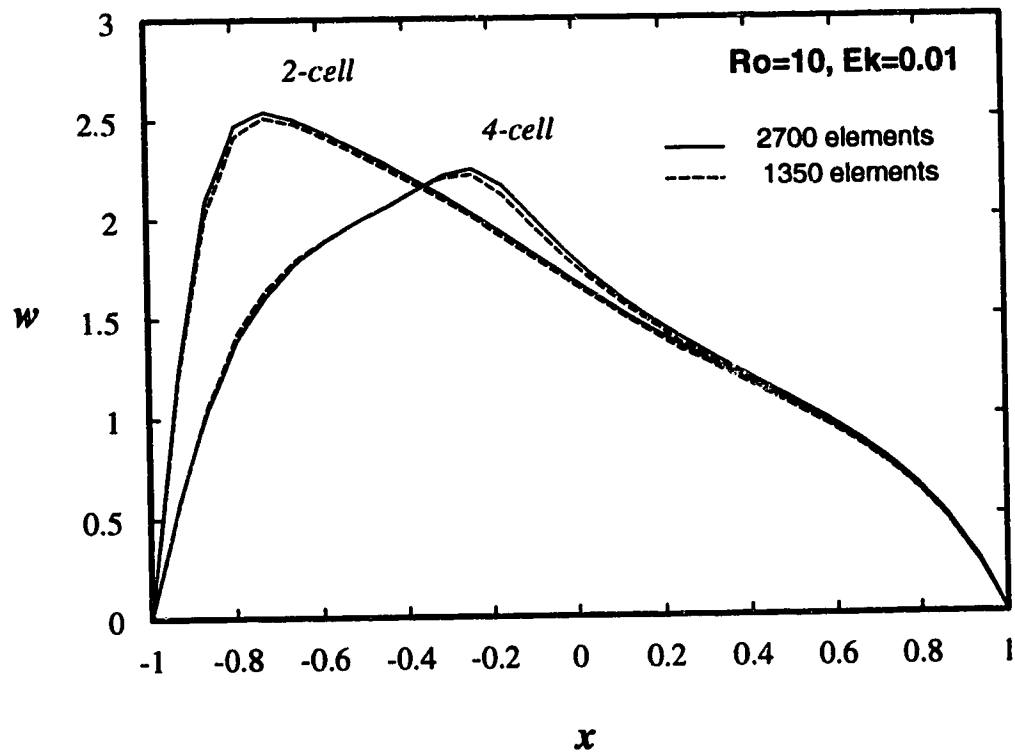


Figure 2.4: Axial velocity profile across the line of symmetry at $Ro = 10$ for two-cell and four-cell secondary flows.

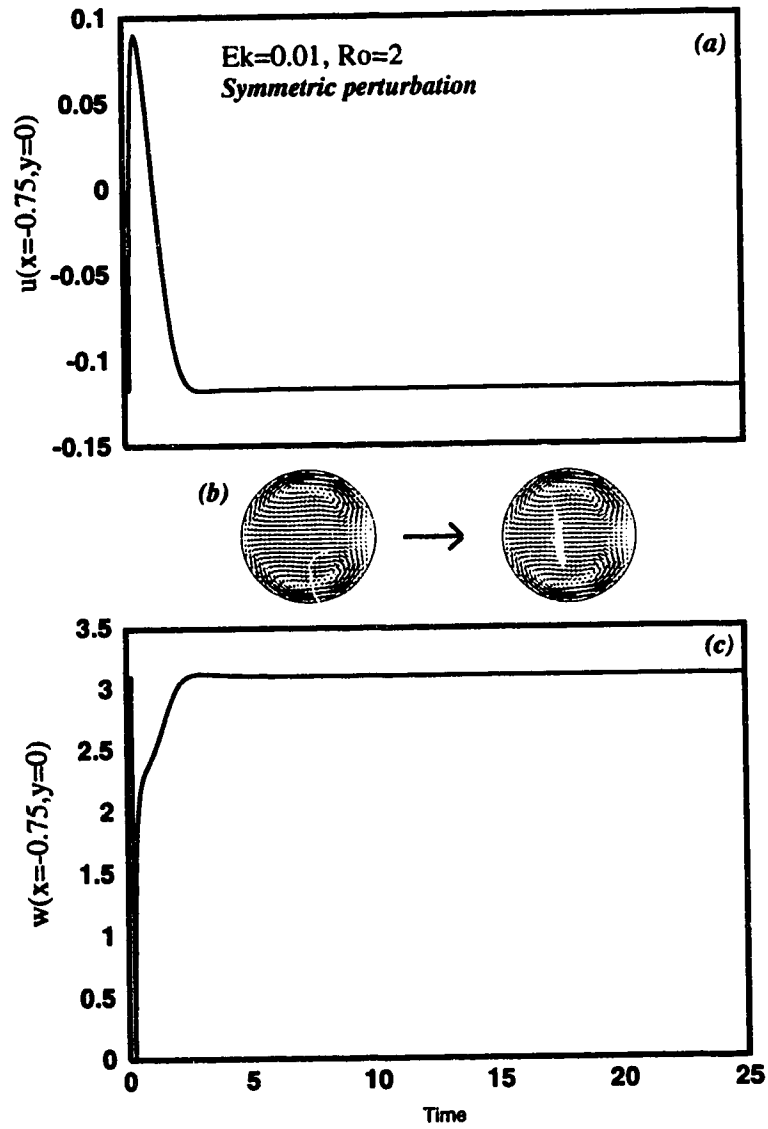


Figure 2.5: Response to a symmetric perturbation of a two-cell secondary flow at $Ro = 2$. (a) Time series plot for transversal velocity, (b) secondary flow before and after a symmetric perturbation and (c) axial velocity

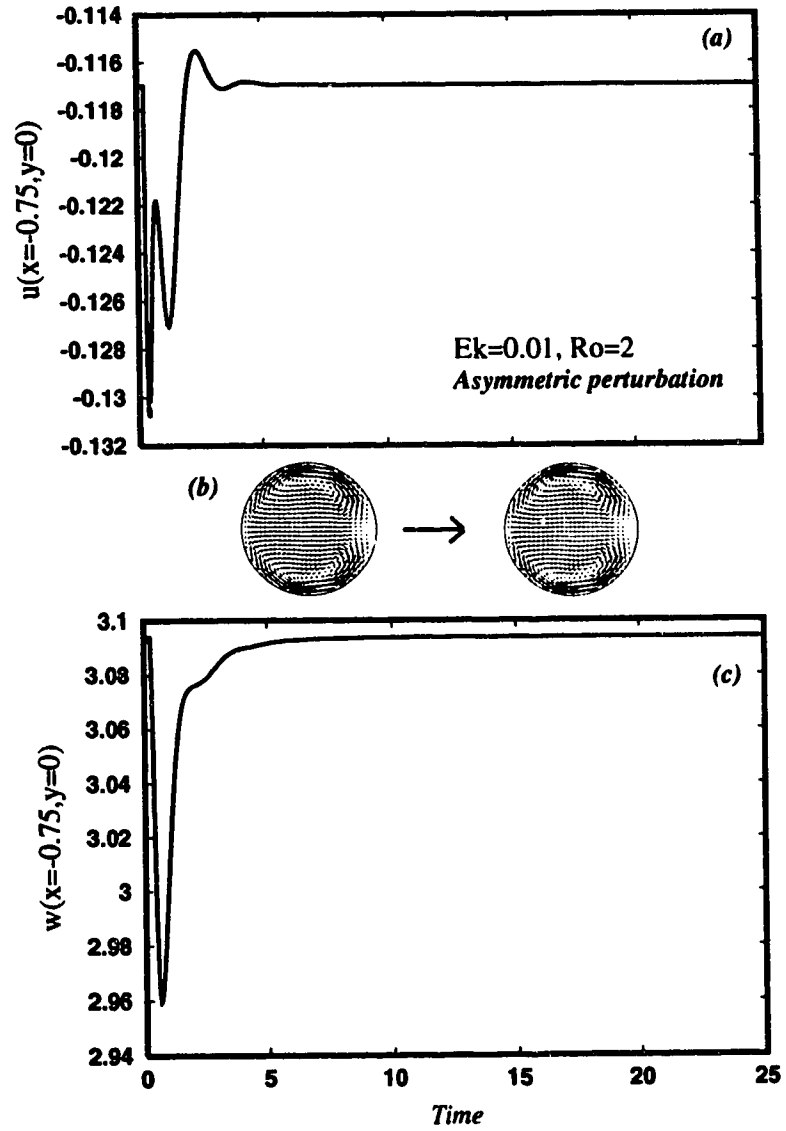


Figure 2.6: Response to an asymmetric perturbation of a two-cell secondary flow at $Ro = 2$. (a) Time series plot for transversal velocity, (b) secondary flow before and after an asymmetric perturbation and (c) axial velocity

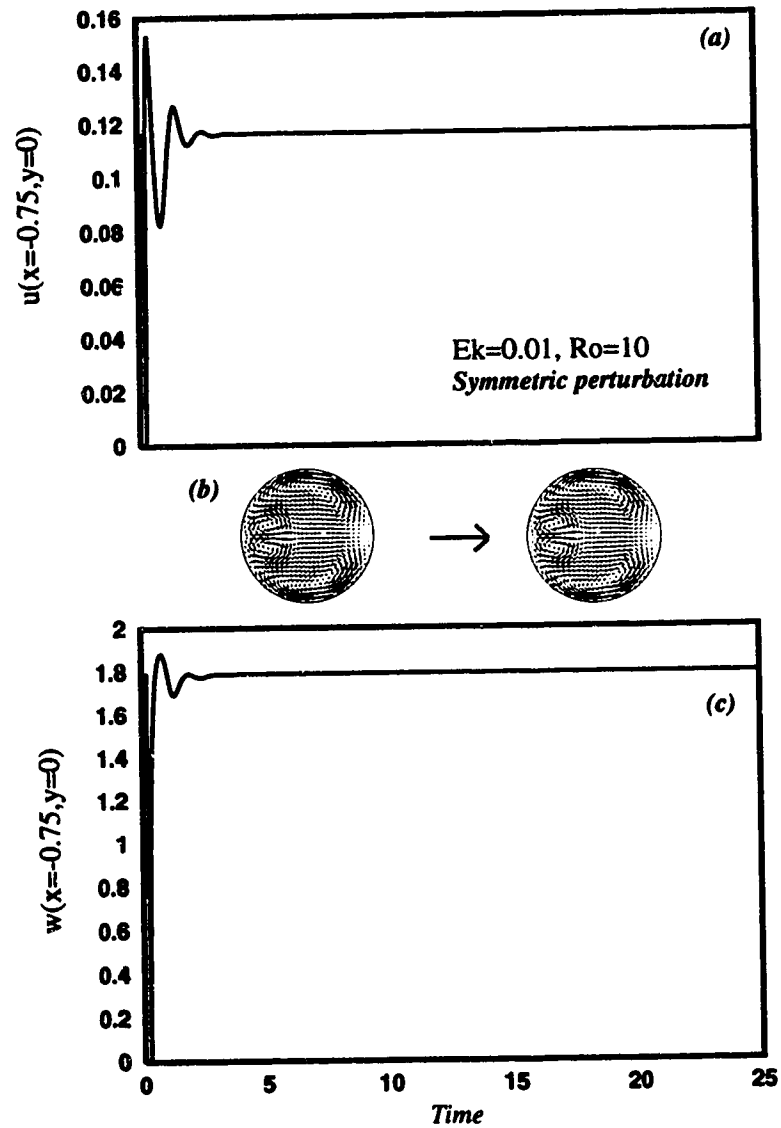


Figure 2.7: Response to a symmetric perturbation of four-cell secondary flow at $Ro = 10$. (a) Time series plot for transversal velocity, (b) secondary flow before and after perturbation and (c) axial velocity

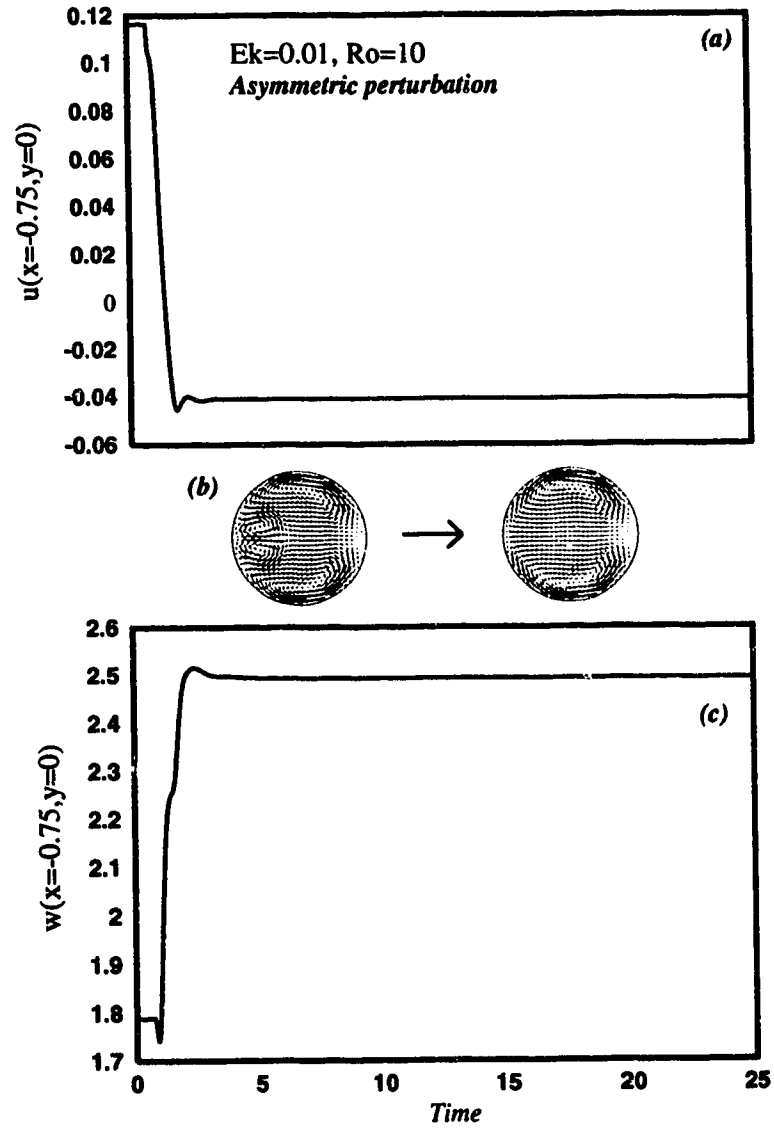


Figure 2.8: Response to an asymmetric perturbation of a four-cell secondary flow at $Ro = 10$. (a) Time series plot for transversal velocity, (b) secondary flow before and after perturbation and (c) axial velocity

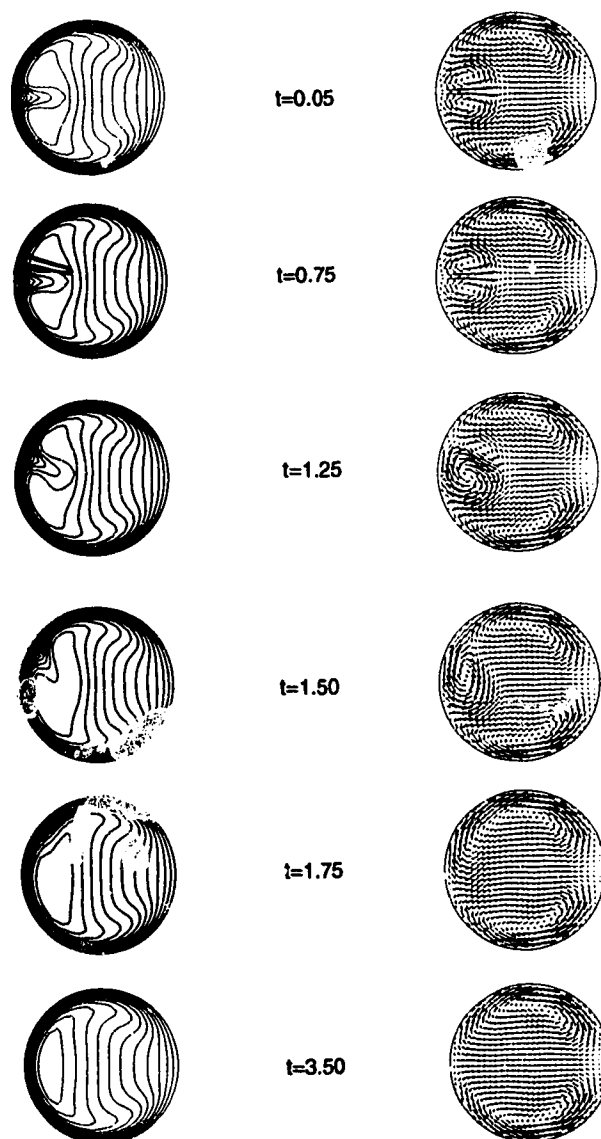


Figure 2.9: Snap shots of contours of axial velocity and vectors of secondary velocity when a four-cell flow is subject to an asymmetric perturbation at $Ro = 10$.

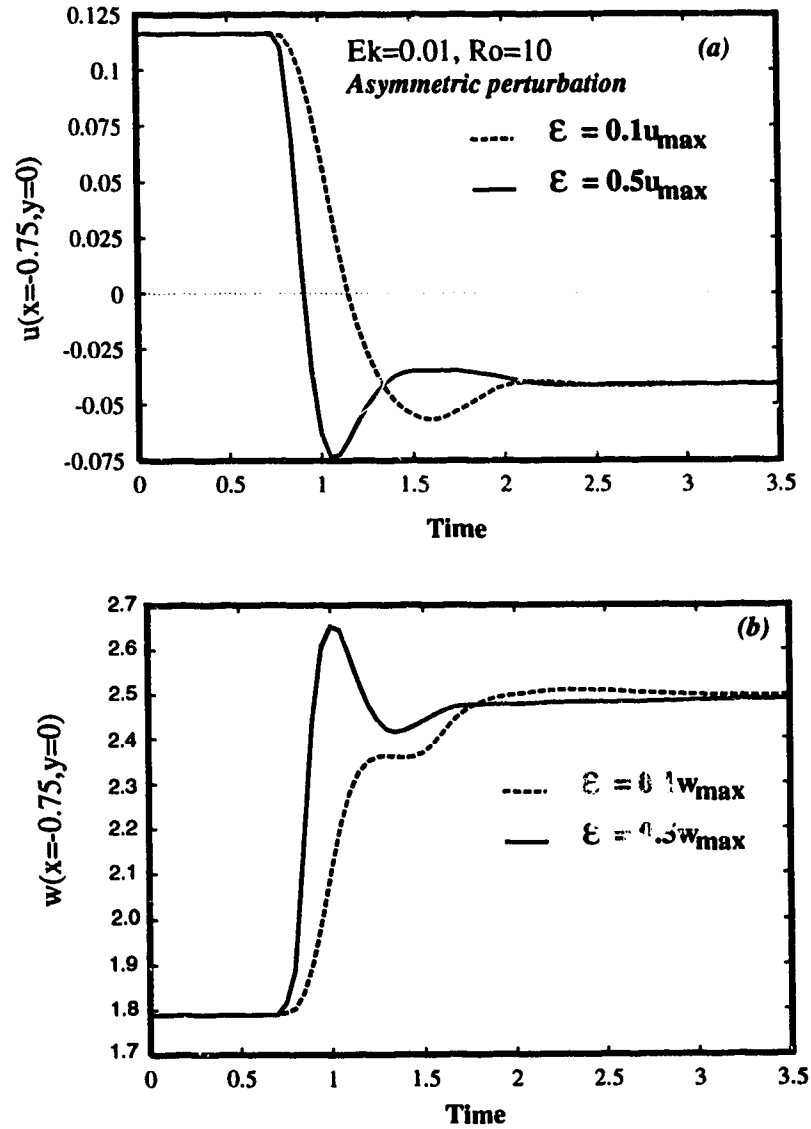


Figure 2.10: Response to a general asymmetric perturbation of a four-cell secondary flow at $Ro = 10$. Figure shows the effect of amplitude of perturbation. (a) Time series plot for transversal velocity and (b) axial velocity

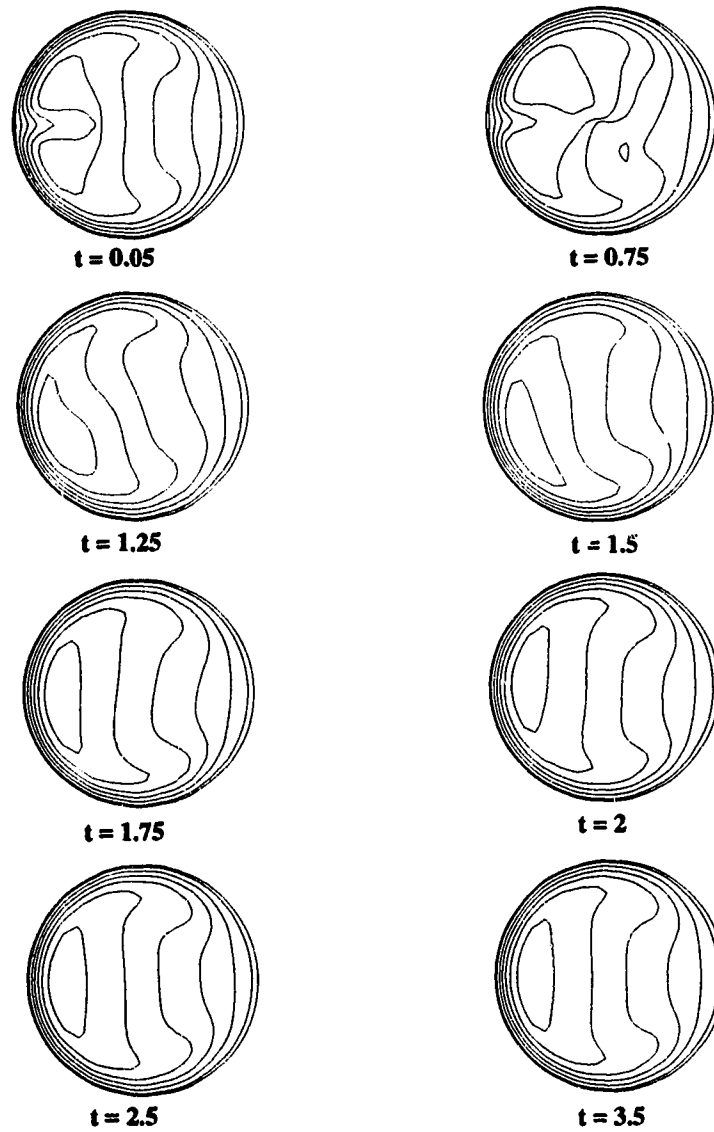


Figure 2.11: Snap shots of contours of axial velocity when a four-cell flow is subject to a general asymmetric perturbation at $Ro = 10$. The amplitude of perturbation $\epsilon = 0.5V_{max}$

References

- BARA, B., NANDAKUMAR, K., & MASLIYAH, J.H. 1992. An experimental and numerical study of the Dean problem: flow development towards two-dimensional multiple solutions. *J. Fluid Mech.*, **244**, 339.
- BARUA, S.N. 1954. Secondary flow in a rotating straight pipe. *Proc. Roy. Soc. London A.*, **227**, 133.
- BARUA, S.N. 1963. On Secondary flow in stationary curved pipes. *Q. J. Mech. Appl. Maths*, **16**, 61.
- BENTON, G.S. 1956. The effect of earth's rotation on laminar flow in pipes. *J. Appl. Mech.*, **23**, 123.
- BENTON, G.S., & BOYER, D. 1966. Flow through a rapidly rotating conduit of arbitrary cross-section. *J. Fluid Mech.*, **26**, 69.
- DASKOPOULOS, P., & LENHOFF, A.M. 1989. Flow in curved ducts: Bifurcation structure for stationary ducts. *J. Fluid Mech.*, **203**, 125.
- DEAN, W.R. 1927. Note on the motion of fluid in a curved pipe. *Phil. Mag*, **4**, 208.
- DEAN, W.R. 1928. The Streamline motion of fluid in a curved pipe(second paper). *Phil. Mag*, **7**, 673.

- DEBRUGE, L.L., & L.S.HAN. 1972. Heat transfer in a channel with a porous wall for turbine cooling application. *J. Heat Transfer*, **94**, 385-390.
- DENNIS, S.R.C., & NG, M. 1982. Dual solutions for steady laminar flows through a curved tube. *Q. J. Mech. Appl. Maths.* **35**, 305.
- DUCK, P.W. 1983. Flow through rotating straight pipes of a circular cross section. *Phys. Fluids*, **26**, 614.
- ITO, H., & K.NANBU. 1971. Flow in a rotating straight pipes of circular cross section. *Trans. ASME D: J.Basic Engng.* **93**, 383.
- KHESHGI, HAROON S., & SCRIVEN, L.E. 1985. Viscous flow through a rotating square channel. *Phys. Fluids*, **28**, 2968.
- MANSOUR, K. 1985. Laminar flow through a slowly rotating straight pipe. *J. Fluid Mech.*, **150**, 1.
- MORI, Y., & NAKAYAMA, W. 1968. Convective heat transfer in a rotating radial circular pipes. *Intl. J. Heat Mass Transfer*, **11**, 1027.
- NANDAKUMAR, K., & MASLIYAH, J.H. 1982. Bifurcation in steady laminar flow through curved tubes. *J. Fluid Mech.*, **119**, 475.
- NANDAKUMAR, K., RASZILLIER, H., & DURST, F. 1991. Flow through rotating rectangular ducts. *Phys. Fluids A*, **3**, 770.
- RASZILLIER, H., & DURST, F. 1991. Coriolis-effect in mass flow metering. *Arch. Appl. Mech.*, **61**, 192.
- SPEZIALE, CHARLES G. 1982. Numerical study of viscous flow in rotating rectangular ducts. *J. Fluid Mech.*, **122**, 251.

- VAN DYKE, M. 1978. Extended stokes series: laminar flow through a loosely coiled pipe. *J. Fluid Mech.*, **86**, 129–145.
- WALKER, J.S. 1975. Steady flow in a rapidly rotating variable area rectangular ducts. *J. Fluid Mech.*, **69**, 209.
- WINTERS, KEITH H. 1987. A bifurcation study of laminar flow in a curved tube of rectangular cross-section. *J. Fluid Mech.*, **180**, 343.
- YANASE, S., GOTO, N.. & YAMAMOTO, K. 1988. Stability of dual solutions of the flow in a curved circular tube. *Journal of the Physical Society of Japan*, **57**(8), 2602–2604.
- YANG, Z., & KELLER, H.B. 1986. Multiple laminar flows through curved pipes. *Applied Numerical Mathematics*, **2**, 257.

Chapter 3

Isothermal flow in a rotating duct

3.1 Introduction

Fully developed laminar flow of an incompressible viscous fluid driven by an axial pressure gradient along a long rectangular duct is not rectilinear if the entire system rotates about an axis perpendicular to the duct. The clockwise rotation of the duct creates a Coriolis force which throws the fast moving fluid in the central core of the duct towards the right when looking downstream of the duct. Because there cannot be any accumulation of the fluid, the fluid is pushed to the top and bottom portion of the duct where it moves back to left wall and thus a secondary flow of two counter rotating vortices is established. The interaction of secondary flow with the pressure driven primary flow causes a shift in the location of maximum streamwise velocity away from the center. When convective inertia becomes stronger relative to Coriolis forces nonlinear effects start dominating and thus a possibility of multiple solutions exists.

The solution structure has several features in common with flow through a curved

duct (the Dean problem), non-isothermal mixed convection heat transfer in a square duct (the Morton problem) and rotating rectangular ducts. In all these problems, the primary flow in the streamwise direction is pressure driven in a finite duct or tube with inlet and outlet. The flow is inherently three dimensional near the inlet region. In certain regions of parameter space, the flow develops from the inlet condition and reaches a streamwise invariant state for low values of the dynamical parameter. In the Dean problem, the effect of curvature introduces centrifugal forces. The interaction of centrifugal forces with convective and viscous forces generates a secondary flow. Thus the flow is at least two-dimensional in nature. If a sufficient inlet length is provided to reach streamwise invariant state, the two-dimensional Navier-Stokes equations can be used to study the flow structure. Similarly in the mixed convection problems, the interaction of buoyancy force with convective and viscous forces results in a secondary flow in the cross-section of the duct. In the flow through a rotating straight duct the secondary flow is generated by Coriolis force due to system rotation. In all of these problems, the primary two-dimensional flow breaks down above a certain critical value of the forcing parameter, leading to a complex bifurcation structure. In the Dean problem, this forcing parameter is called Dean number, Dn , which represents the ratio of inertial and centrifugal forces, to viscous forces. In a similar way, the Grashoff number, Gr represents the effect of buoyancy on secondary flow generation. The relative importance of the forces that govern the flow structure in flow through a rotating duct can be characterized by two dynamical parameters - viz., the Ekman number, Ek , represents the ratio of viscous to Coriolis forces and the Rossby number, Ro , represents the ratio of inertial to Coriolis forces. Other forms of dynamical parameters in terms of the Reynolds number and the rotational number have also been used in literature.

The earliest work on flow in a rotating straight pipe was inspired by Dean's (1927;

1928) work on stationary curved pipes. It was carried out for the asymptotic limits of weak and strong rotations by Barua(1954) and Benton(1956) using a perturbation expansion on the Hagen-Poiseuille flow. The studies of Mori & Nakayama(1968), and of Ito & Nanbu(1971) for small rotational speeds and high axial pressure gradients resulted in good agreement with experiments, showing an increase in friction factor with rotational speed. At the other extreme of the asymptotic limit, Benton(1966) considered the flow through a rapidly rotating channel. He showed that viscous effects are important only in a thin boundary layer along the channel walls and in the interior, where the nonlinear acceleration and viscous terms in the Navier-Stokes equations can be neglected with respect to the Coriolis term, the flow is geostrophic. In a numerical study of the flow in a rotating, rectangular duct Speziale (1982) demonstrated that a transition from a two-cell to a four-cell flow structure occurs as Ro is changed. Duck(1983) examined the flow through rotating straight pipes of a circular cross section using Fourier decomposition in the angular direction. However, due to the convergence difficulties of the iterative solution method used, no solutions at high Rossby numbers could be obtained. In particular, a dual four-cell solution was not computed. Solution multiplicity is, however, expected since the equations governing the two-dimensional flows through rotating channels are analogous to those of laminar flow in coiled ducts(the Dean problem) in the double limit of $Ek \rightarrow \infty$, $(Ro/Ek) \rightarrow \infty$, and $(Ro/Ek^2) = \text{constant}$ as shown, for example, by Mansour(1985). A comprehensive bifurcation study for the flow through a rotating duct is done by Nandakumar *et al.* (1991). Their study confirmed the hysteresis behavior between the two- and four-cell flow structure by Kheshgi & Scriven(1985). Further they found an additional branch that has a two-cell flow structure at one end, and a four-cell flow structure at the other with three limit points on the path. Two asymmetric solution branches emanating from symmetry breaking bifurcation points are also found. They found five solutions at $Ro = 5$. It was also confirmed

for a rotating duct that four cell solution is unstable to asymmetric perturbation. Unfolding of bifurcation diagram with angle of tilt and the effect of aspect ratio is also investigated.

The objective of this chapter is to test our computational code and reconstruct a bifurcation diagram similar to Nandakumar *et al.* (1991), on which the effect of heating will be discussed in the next chapter.

3.2 Governing equations

We consider the flow of an incompressible fluid of density ρ and viscosity μ through a rectangular duct of width a and height b , and rotating about an axis perpendicular to the axis of symmetry of duct at the rate Ω . The aspect ratio of the duct is $\gamma = b/a$. The cross-section of the duct can be tilted by ϕ° with respect to rotational axis as shown in Figure 3.1. The flow is driven by a constant imposed pressure gradient, $\partial\varphi/\partial\hat{z}$. The Navier-Stokes equations governing the two-dimensional flow through the rotating duct, are given by

$$\frac{\partial\hat{u}}{\partial\hat{x}} + \frac{\partial\hat{v}}{\partial\hat{y}} = 0 \quad (3.1)$$

$$\frac{\partial\hat{u}}{\partial\hat{t}} + \left(\hat{u}\frac{\partial\hat{u}}{\partial\hat{x}} + \hat{v}\frac{\partial\hat{u}}{\partial\hat{y}} \right) = -\frac{\partial\varphi}{\partial\hat{x}} + \frac{\mu}{\rho}\hat{\nabla}^2\hat{u} - 2\Omega\hat{w}\cos\phi \quad (3.2)$$

$$\frac{\partial\hat{v}}{\partial\hat{t}} + \left(\hat{u}\frac{\partial\hat{v}}{\partial\hat{x}} + \hat{v}\frac{\partial\hat{v}}{\partial\hat{y}} \right) = -\frac{\partial\varphi}{\partial\hat{y}} + \frac{\mu}{\rho}\hat{\nabla}^2\hat{v} + 2\Omega\hat{w}\sin\phi \quad (3.3)$$

$$\frac{\partial\hat{w}}{\partial\hat{t}} + \left(\hat{u}\frac{\partial\hat{w}}{\partial\hat{x}} + \hat{v}\frac{\partial\hat{w}}{\partial\hat{y}} \right) = -\frac{\partial\varphi}{\partial\hat{z}} + \frac{\mu}{\rho}\hat{\nabla}^2\hat{w} + 2\Omega(\hat{u}\cos\phi - \hat{v}\sin\phi) \quad (3.4)$$

where $\hat{\nabla}^2 = \frac{\partial^2}{\partial\hat{x}^2} + \frac{\partial^2}{\partial\hat{y}^2}$. Here $[\hat{u}(\hat{x},\hat{y}), \hat{v}(\hat{x},\hat{y}), \hat{w}(\hat{x},\hat{y})]$ represents the velocity vector and φ is a potential that combines the centrifugal, gravitational and thermodynamics pressure. The rotation vector $(\Omega\sin\phi, \Omega\cos\phi, 0)$ allows the duct to be tilted with

respect to the rotation axis by an angle ϕ° . Here Ω is the magnitude of the rotational speed. Equations(3.1-3.4) have to be solved subject to no slip and impenetrability conditions at the walls of the duct:

$$\hat{u} = \hat{v} = \hat{w} = 0 \text{ at } \hat{x} = \pm \frac{a}{2} \text{ and } \hat{y} = \pm \frac{b}{2} \quad (3.5)$$

Taking the axis of the duct to be the z direction, and invoking the fully developed condition that the velocity components are independent of z , it follows that $\frac{\partial \hat{\psi}}{\partial \hat{z}}$ is constant. Two dimensionality allows the introduction of a stream function as

$$\hat{u} = \frac{\partial \hat{\psi}}{\partial \hat{y}}, \quad \text{and} \quad \hat{v} = -\frac{\partial \hat{\psi}}{\partial \hat{x}} \quad (3.6)$$

The above equations are non-dimensionalized using the following scales:

$$u = \frac{\hat{u}}{U}, \quad v = \frac{\hat{v}}{U}, \quad w = \frac{\hat{w}}{U}, \quad x = \frac{\hat{x}}{a}, \quad y = \frac{\hat{y}}{b},$$

$$\tau = \hat{t}\Omega, \quad \varphi = \frac{\hat{\varphi}}{bU\Omega}, \quad \psi = \frac{\hat{\psi}}{bU} \quad (3.7)$$

where $U = -\varphi_z/\rho\Omega$. The non-dimensional equations take the following form:

$$\gamma \frac{\partial u}{\partial x} + \frac{\partial v}{\partial y} = 0 \quad (3.8)$$

$$\frac{\partial u}{\partial \tau} + Ro \left(\gamma u \frac{\partial u}{\partial x} + v \frac{\partial u}{\partial y} \right) = -\gamma \frac{\partial \varphi}{\partial x} + Ek \nabla^2 u - 2w \cos \phi \quad (3.9)$$

$$\frac{\partial v}{\partial \tau} + Ro \left(\gamma u \frac{\partial v}{\partial x} + v \frac{\partial v}{\partial y} \right) = -\frac{\partial \varphi}{\partial y} + Ek \nabla^2 v + 2w \sin \phi \quad (3.10)$$

$$\frac{\partial w}{\partial \tau} + Ro \left(\gamma u \frac{\partial w}{\partial x} + v \frac{\partial w}{\partial y} \right) = 1 + Ek \nabla^2 w + 2(u \cos \phi - v \sin \phi) \quad (3.11)$$

where $\nabla^2 = \gamma^2 \frac{\partial^2}{\partial x^2} + \frac{\partial^2}{\partial y^2}$; $\gamma = b/a$ is the aspect ratio; $Ro = U/b\Omega$ is the Rossby number; $Ek = \nu/b^2\Omega$ is the Ekman number.

The choice of scales is by no means unique. Hence there is a proliferation of definitions of dimensionless groups dealing with flow in a rotating duct. Our choice

is inspired by the work of Khesghi & Scriven (1985) and Nandakumar *et al.* (1991). An alternative choice that leads to a Reynolds number and a rotation number is also used frequently. Such alternative definitions are clearly related. For example the Reynolds number defined as $Re = bU/\nu$ is related to Rossby number and Ekman numbers by $Re = Ro/Ek$, while the rotation number defined as $R_\Omega = 1/Ro$. More important than defining a particular choice of scales an understanding of the physical interpretation of the resulting dimensionless numbers. In our case the Ekman number represents the ratio of viscous to Coriolis force and is held constant at $Ek = 0.01$. The Rossby number represents the ratio of inertial to Coriolis forces. As the rotational speed Ω is increased, the rotational effects are increased. This corresponds to the low Rossby number limit. At higher Rossby numbers, the inertial effects dominate the solution and flow structures.

The equation of continuity is satisfied by introducing the stream function ψ such that taking curl of momentum equations eliminates the potential, φ and yields the vorticity transport equation having the streamwise component:

$$\frac{\partial \xi}{\partial \tau} = Ek \nabla^2 \xi + Ro \gamma \left(\frac{\partial \psi}{\partial x} \frac{\partial \xi}{\partial y} - \frac{\partial \psi}{\partial y} \frac{\partial \xi}{\partial x} \right) + 2 \left(\gamma \frac{\partial w}{\partial x} \sin \phi + \frac{\partial w}{\partial y} \cos \phi \right) \quad (3.12)$$

where ξ is the streamwise component of the vorticity. The third term in the right hand side of equation(3.12), $2 \left(\gamma \frac{\partial w}{\partial x} \sin \phi + \frac{\partial w}{\partial y} \cos \phi \right)$, is the source term for generating streamwise vorticity by Coriolis force. It should be noted, for an angle of tilt $\phi = 0$, this term depends on the gradient of streamwise velocity with respect to the spanwise direction, which is always non-zero owing to the presence of the wall boundaries in the spanwise direction. Thus secondary flow is always present for any non-zero forcing. In the idealized case of infinite extent in the spanwise direction, the basic flow will be one-dimensional and two-dimensional solutions emerge at supercritical bifurcations. In the present case, however, the basic flow is itself two-dimensional with counter rotating streamwise vortices. The streamwise vorticity is

related to the stream function ψ by

$$\xi = \gamma \frac{\partial v}{\partial x} - \frac{\partial u}{\partial y} = -\nabla^2 \psi \quad (3.13)$$

By substituting these equations in equation(3.12), we obtain the streamwise vorticity equation in the stream-function form:

$$\begin{aligned} \frac{\partial (-\nabla^2 \psi)}{\partial \tau} = & -Ek \nabla^4 \psi \\ & + Ro \gamma \left[\left(\gamma^2 \frac{\partial^3 \psi}{\partial x^3} \frac{\partial \psi}{\partial y} - \frac{\partial \psi}{\partial x} \frac{\partial^3 \psi}{\partial y^3} \right) - \left(\gamma^2 \frac{\partial \psi}{\partial x} \frac{\partial^3 \psi}{\partial x^2 y} + \frac{\partial^3 \psi}{\partial x y^2} \frac{\partial \psi}{\partial y} \right) \right] \\ & + 2 \left(\gamma \frac{\partial w}{\partial x} \sin \phi + \frac{\partial w}{\partial y} \cos \phi \right) \end{aligned} \quad (3.14)$$

where

$$\nabla^4 = \gamma^4 \frac{\partial^4}{\partial x^4} + 2\gamma^2 \frac{\partial^4}{\partial x^2 y^2} + \frac{\partial^4}{\partial y^4}$$

and the streamwise momentum equation(3.11) can be written as

$$\begin{aligned} \frac{\partial w}{\partial \tau} = & 1 + Ek \nabla^2 w + Ro \gamma \left(\frac{\partial \psi}{\partial x} \frac{\partial w}{\partial y} - \frac{\partial \psi}{\partial y} \frac{\partial w}{\partial x} \right) \\ & + 2 \left(\gamma \frac{\partial \psi}{\partial x} \sin \phi + \frac{\partial \psi}{\partial y} \cos \phi \right) \end{aligned} \quad (3.15)$$

We have to find the stationary solutions of the equations(3.14) and (3.15). The computational domains for finding stationary symmetric and asymmetric solutions are given by R^+ (Half domain) and R (Full domain) respectively. They are defined as:

$$R^+ := \{(x, y) \mid -0.5 \leq x \leq 0.5, 0 \leq y \leq 0.5\} \quad (3.16)$$

$$R := \{(x, y) \mid -0.5 \leq x \leq 0.5, -0.5 \leq y \leq 0.5\} \quad (3.17)$$

For finding stationary solutions in the full domain the boundary conditions are no-slip and impenetrability conditions at the walls of the duct:

$$w = 0, \quad \psi = 0, \quad \frac{\partial \psi}{\partial x} = 0, \quad \text{and} \quad \frac{\partial \psi}{\partial y} = 0 \quad \text{at} \quad x = \pm \frac{1}{2}, y = \pm \frac{1}{2} \quad (3.18)$$

For $\phi = 0$, the following symmetry properties exist:

$$\begin{aligned} w(x, -y) &= w(x, y) \\ \xi(x, -y) &= -\xi(x, y) \\ \psi(x, -y) &= -\psi(x, y) \end{aligned} \quad (3.19)$$

Thus, at the line of symmetry ($x, y = 0$), the boundary conditions are

$$\frac{\partial w}{\partial y} = 0, \quad \psi = 0, \quad \text{and} \quad \xi = 0 \quad (3.20)$$

which can be used as boundary conditions while computing symmetric solutions in the half domain R^+ .

3.3 Numerical methods

We are primarily interested in finding out the multiple stationary solutions to (3.14) and (3.15). The transient two-dimensional solutions are not physically realizable in an experiment as they are inconsistent with the streamwise invariance or fully developed flow assumption. In other words we expect any disturbance at a streamwise position to grow (or decay) with time as well as be carried downstream by the forced axial flow. In regions of the parameter space where there are multiple solutions, the pseudo-transient simulation may converge to any one of the stationary solutions, depending on the initial starting condition, the stability and the region of attraction of the stationary solution. Whenever we refer to (3.14) and (3.15), we mean the stationary form of (3.14) and (3.15). Together with the boundary conditions (3.18), they can be written symbolically as a single equation,

$$f(\mathbf{u}, \mathbf{p}) = 0 \quad (3.21)$$

where $\mathbf{u} = [\psi(x, y), w(x, y)]$ and $\mathbf{p} = [Ro, Ek, \phi, \gamma]$ is the parameter set.

3.3.1 Spectral approximation

The equations (3.21) are discretized using spectral approximation. The expansion functions for the approximation are chosen as linear combinations of Chebyshev polynomials such that they satisfy the boundary conditions at the wall. The approximate solution ψ , for stream function and w , for streamwise velocity on the physical domain of the duct can be expressed as:

$$\psi = \sum_{m=0}^{N_x-1} \sum_{n=0}^{N_y-1} C_{mn}^{\psi} X_m^{\psi}(\tilde{x}) Y_n^{\psi}(\tilde{y}) \quad (3.22)$$

$$w = \sum_{m=0}^{N_x-1} \sum_{n=0}^{N_y-1} C_{mn}^w X_m^w(\tilde{x}) Y_n^w(\tilde{y}) \quad (3.23)$$

where

$$\tilde{x} = 2x, \quad \text{and} \quad \tilde{y} = 2y$$

are algebraic mapping that transform the cross-section of the duct into the computational domain of Chebyshev polynomials $[-1,1]$ and the expansion functions X_m^{ψ} , Y_m^w , X_n^{ψ} and Y_n^w are defined as follows:

$$X_l^w(\tilde{x}) = Y_l^w(\tilde{x}) = T_{l+2}(\tilde{x}) - T_l(\tilde{x}), \quad (3.24)$$

$$X_l^{\psi}(\tilde{x}) = Y_l^{\psi}(\tilde{x}) = (l+1)T_{l+4}(\tilde{x}) - 2(l+2)T_{l+2}(\tilde{x}) + (l+3)T_l(\tilde{x}), \quad (3.25)$$

For half domain(R^+) calculations they take the form of,

$$X_l^w(\tilde{x}) = T_{l+2}(\tilde{x}) - T_l(\tilde{x}), \quad (3.26)$$

$$Y_l^w(\tilde{x}) = T_{2l+2}(\tilde{x}) - T_{2l}(\tilde{x}), \quad (3.27)$$

$$X_l^{\psi}(\tilde{x}) = (l+1)T_{l+4}(\tilde{x}) - 2(l+2)T_{l+2}(\tilde{x}) + (l+3)T_l(\tilde{x}), \quad (3.28)$$

$$Y_l^{\psi}(\tilde{x}) = (2l+2)T_{2l+5}(\tilde{x}) - 2(2l+3)T_{2l+3}(\tilde{x}) + (2l+4)T_{2l+1}(\tilde{x}), \quad (3.29)$$

where $l = 0, 1, 2, \dots$, and \tilde{x} in $[-1, 1]$.

When the approximating functions ψ and w are substituted into equation(3.21), we get a system of nonlinear algebraic equations for the expansion coefficients, C_{mn}^ψ and C_{mn}^w . The resulting equations are satisfied at the Chebyshev-Gauss-Lobatto points

$$(\tilde{x}_j, \tilde{y}_k) = \left(\cos \frac{j\pi}{N_x}, \cos \frac{k\pi}{N_y} \right) \quad (3.30)$$

for $j = 1, 2, \dots, N_x, k = 1, 2, \dots, N_y$. We write this system symbolically as a vector \mathbf{f} of size $N = 2N_x N_y$ that contains the discrete form of the momentum and vorticity equations,

$$\mathbf{f}(\mathbf{C}; \mathbf{p}) = \mathbf{0}, \quad (3.31)$$

where, $\mathbf{C} := [C_{mn}^\psi, C_{mn}^w]$. Our task is to solve the system of nonlinear equations as a function of the components of \mathbf{p} . Once the expansion coefficients are found, the flow variables are obtained from the expansion functions.

3.3.2 Arclength continuation

Based on previous studies(Winters (1987); Nandakumar *et al.* (1991)) we expect the flow structure to begin with two counter-rotating streamwise-oriented vortices that bifurcate into more complicated flow structures through several limit or symmetry breaking points as the Rossby number increases. For low values of Ro the governing equations (3.14) and (3.15) tend to become linear and therefore we can get a good initial guess for Newton's method. Thus, equations (3.14) and (3.15) are solved using Newton's method and a zero initial guess. A correction to the estimated solution is found through a Newton-Raphson iteration

$$\delta \mathbf{C} = \mathbf{J}^{-1} \mathbf{f} \quad (3.32)$$

where \mathbf{J} is the Jacobian of the system of equations. Once a converged solution is obtained Euler-Newton continuation is used to continue on any chosen parameter,

say α , a component of the vector \mathbf{p} . This entails developing a good initial guess for the solution at

$$\mathbf{C}(\alpha + \Delta\alpha) = \mathbf{C}(\alpha) + \frac{\partial \mathbf{C}}{\partial \alpha} \Delta\alpha, \quad (3.33)$$

where $\frac{\partial \mathbf{C}}{\partial \alpha}$ is found from differentiating \mathbf{f} with respect to α :

$$\mathbf{J} \frac{\partial \mathbf{C}}{\partial \alpha} = -\frac{\partial \mathbf{f}}{\partial \alpha}. \quad (3.34)$$

This requires only one back substitution since \mathbf{J} is already factored during the previous Newton iteration. When this method fails to converge, a nearby singularity is indicated and we switch to the arclength continuation scheme. This entails reparametrizing the problem in terms of arclength, s ,

$$\mathbf{f}(\mathbf{C}(s), \alpha(s)) = 0 \quad (3.35)$$

A parameterization is a kind of measure along the branch, a mathematical way of identifying each solution on the branch. Various parametrizing schemes have been proposed with efficient step size control. In this study we use one suggested by Keller(1977),

$$\begin{aligned} \mathcal{N}(\mathbf{C}, \alpha, s) &= w_1 \sum_{j=1}^N \left(\frac{dc_j}{ds} \right)_{s_o} [c_j(s) - c_j(s_o)] \\ &+ w_2 \left(\frac{d\alpha}{ds} \right)_{s_o} [\alpha(s) - \alpha(s_o)] - (s - s_o) = 0 \end{aligned} \quad (3.36)$$

where w_1 and w_2 are the tuning parameters that allows us to place different emphasis on \mathbf{C} or on α . The tangents dc_j/ds and $d\alpha/ds$ are computed using

$$\left(\frac{d\alpha}{ds} \right)_{s_o} = \frac{1}{\sqrt{w_1 \sum_{j=1}^N \left(\frac{dc_j}{d\alpha} \right)^2 + w_2}} \quad (3.37)$$

$$\left(\frac{dc_j}{ds} \right)_{s_o} = \left(\frac{dc_j}{d\alpha} \right) \left(\frac{d\alpha}{ds} \right)_{s_o} \quad (3.38)$$

We formulate the following extended system,

$$\begin{bmatrix} \mathbf{f}(\mathbf{C}, \alpha) \\ \mathcal{N}(\mathbf{C}, \alpha, s) \end{bmatrix} = \mathbf{0} \quad (3.39)$$

which consists of $N + 1$ scalar equations for $N + 1$ unknowns (\mathbf{C}, α) . The resulting extended system(3.39) is solved by Newton's method for a specified s and this procedure has no difficulty in turning around limit points. A simple step-length adjustment procedure, which adjusts Δs such that the Newton iteration converges to specified tolerance within four iterations, was found to be adequate to turn around even sharp corners. Differentiating \mathbf{f} with respect to s provides

$$\sum_{k=1}^N \frac{\partial f_j}{\partial c_k} \frac{dc_k}{ds} = -\frac{\partial f_j}{\partial \alpha} \frac{d\alpha}{ds}. \quad (3.40)$$

Equations(3.40) and (3.36) are solved for $\frac{dc_j}{ds}$ and $\frac{d\alpha}{ds}$ and represent a regular system. Once $\frac{dc_j}{ds}$ and $\frac{d\alpha}{ds}$ are found at a particular s , Euler's method is used to predict the solution at $s + \Delta s$:

$$c_j(s + \Delta s) = c_j(s) + \frac{dc_j}{ds} \Delta s. \quad (3.41)$$

$$\alpha(s + \Delta s) = \alpha(s) + \frac{d\alpha}{ds} \Delta s. \quad (3.42)$$

3.3.3 Limit points

If $(\bar{\mathbf{u}}, \bar{\mathbf{p}})$ is a regular solution of (3.21), then $f_u(\bar{\mathbf{u}}, \bar{\mathbf{p}})\mathbf{h} = \mathbf{v}$ has a unique solution \mathbf{h} for any \mathbf{v} . In particular, for $\mathbf{v} = \mathbf{0}$, the only solution is $\mathbf{h} = \mathbf{0}$. On the other hand, if $(\mathbf{u}_o, \mathbf{p}_o)$ is a singular point of (3.21) then $f_u(\mathbf{u}_o, \mathbf{p}_o)\mathbf{h} = \mathbf{0}$ has a nontrivial solution $\mathbf{h} \neq \mathbf{0}$. If the Jacobian, $f_u(\mathbf{u}_o, \mathbf{p}_o)$ has a simple zero eigenvalue and $f_p(\mathbf{u}_o, \mathbf{p}_o) \notin \text{range}\{f_u(\mathbf{u}_o, \mathbf{p}_o)\}$, then $(\mathbf{u}_o, \mathbf{p}_o)$ is a limit point. A simple limit point can be located by solving the following extended system, proposed by Moore

& Spence (1980) and Spence and Werner (1982)

$$\begin{pmatrix} f(\mathbf{u}, \alpha) \\ f_u(\mathbf{u}, \alpha) \mathbf{h} \\ m(\mathbf{h}) \end{pmatrix} = \begin{pmatrix} 0 \\ 0 \\ 1 \end{pmatrix} \quad (3.43)$$

In equation(3.43), \mathbf{h} is the right null vector, and the constraint $m(\mathbf{h}) = 1$ enforces the null vector to be non-trivial. This system is known to be regular and can be solved by Newton scheme for the unknown vector $(\mathbf{u}, \mathbf{h}, \alpha)$. In order to solve extended system(3.43), a sufficient good initial guess $\mathbf{h}_o(\tilde{\psi}_o, \tilde{w}_o)$ is needed for the the right eigenvector \mathbf{h} . The limit point monitoring scheme proposed by Weinitschke (1985) was found to be useful.

Consider a linear boundary value problem $f_u(\mathbf{u}, \alpha) \mathbf{h}^* = \mathbf{c}^*$ with $\mathbf{c}^* = (1, 0)$. It allows a non-trivial unique solution, $\mathbf{h}^*(\psi^*, w^*)$ at a regular point. If we let $\mathbf{h}_o^* = \epsilon \mathbf{h}^*$ and determine ϵ from $m(\mathbf{h}_o^*) = m(\epsilon \mathbf{h}^*) = 1$, it follows that \mathbf{h}_o satisfies $f_u(\mathbf{u}, \alpha) \mathbf{h}_o = \mathbf{c}$ with $\mathbf{c} = (\epsilon, 0)$.

As $\alpha \rightarrow \alpha_o$, where α_o is the limit point, $\epsilon \rightarrow 0$. Thus, if $\epsilon(\alpha) \rightarrow 0$ when computing a sequence of solutions on the branch, we are approximating a limit point of $f(\mathbf{u}, \alpha) = 0$. The extended system(3.43) is solved with initial guess \mathbf{h}_o . Thus, the extended system amounts to solving for unknowns $(\psi, w, \tilde{\psi}, \tilde{w}, \alpha)$ with $(\psi_o, w_o, \tilde{\psi}_o, \tilde{w}_o, \alpha_o)$ as the initial guess to Newton's method.

In Chebshev space, these unknowns are expressed as

$$\psi = \sum_{m=0}^{N_x-1} \sum_{n=0}^{N_y-1} C_{mn}^{\psi} X_m^{\psi}(\tilde{x}) Y_n^{\psi}(\tilde{y}) \quad (3.44)$$

$$w = \sum_{m=0}^{N_x-1} \sum_{n=0}^{N_y-1} C_{mn}^w X_m^w(\tilde{x}) Y_n^w(\tilde{y}) \quad (3.45)$$

$$\tilde{\psi} = \sum_{m=0}^{N_x-1} \sum_{n=0}^{N_y-1} \tilde{C}_{mn}^{\psi} X_m^{\psi}(\tilde{x}) Y_n^{\psi}(\tilde{y}) \quad (3.46)$$

$$\tilde{w} = \sum_{m=0}^{N_x-1} \sum_{n=0}^{N_y-1} \tilde{C}_{mn}^w X_m^w(\tilde{x}) Y_n^w(\tilde{y}) \quad (3.47)$$

where the expansion functions in half domain (R^+) are defined as:

$$X_l^w(\tilde{x}) = \tilde{X}_l^w(\tilde{x}) = T_{l+2}(\tilde{x}) - T_l(\tilde{x}) \quad (3.48)$$

$$Y_l^w(\tilde{x}) = \tilde{Y}_l^w(\tilde{x}) = T_{2l+2}(\tilde{x}) - T_{2l}(\tilde{x}) \quad (3.49)$$

$$X_l^\psi(\tilde{x}) = \tilde{X}_l^\psi(\tilde{x}) = (l+1)T_{l+4}(\tilde{x}) - 2(l+2)T_{l+2}(\tilde{x}) + (l+3)T_l(\tilde{x}) \quad (3.50)$$

$$Y_l^\psi(\tilde{x}) = \tilde{Y}_l^\psi(\tilde{x}) = (2l+2)T_{2l+5}(\tilde{x}) - 2(2l+3)T_{2l+3}(\tilde{x}) + (2l+4)T_{2l+1}(\tilde{x}) \quad (3.51)$$

3.3.4 Symmetry breaking bifurcation points

The symmetry breaking bifurcation points may be described as the bifurcation in which the solutions of one of the two intersecting branches are symmetric while the solutions of the other branch are asymmetric. The symmetry S is defined by

$$S \neq I, \quad S^2 = I, \quad f(S\mathbf{u}, \alpha) = Sf(\mathbf{u}, \alpha) \quad (3.52)$$

Consider the symmetric subspace, $X_s := [\mathbf{u} \mid S\mathbf{u} = \mathbf{u}]$, and the antisymmetric subspace $X_a := [\mathbf{u} \mid S\mathbf{u} = -\mathbf{u}]$. If $\mathbf{z}_o(\mathbf{u}_o, \alpha_o)$ is the simple bifurcation point and $u_o \in X_s$ and $h_o \in X_a$, then $\mathbf{z}_o(\mathbf{u}_o, \alpha_o)$ is the pitchfork type symmetry breaking bifurcation point and can be located by solving the same extended system with the restriction $u_o \in X_s$ and $h_o \in X_a$.

The symmetry properties of the present problem are

$$\begin{aligned} w(x, -y) &= w(x, y) \\ \psi(x, -y) &= -\psi(x, y) \end{aligned} \quad (3.53)$$

The subspaces X_s and X_a are

$$X_s = [(\psi, w) \mid w(x, -y) = w(x, y), \psi(x, -y) = -\psi(x, y)]$$

$$X_a = [(\psi, w) \mid w(x, -y) = -w(x, y), \psi(x, -y) = \psi(x, y)]$$

Therefore, to calculate the symmetry breaking bifurcation point, the extended system must be solved with the following symmetry and antisymmetry conditions at $y = 0$

$$\frac{\partial w}{\partial y} = 0, \quad \psi = 0$$

$$\frac{\partial \tilde{\psi}}{\partial y} = 0, \quad \tilde{w} = 0$$

Thus, the extended system amounts to solving for the unknowns $(\psi, w, \tilde{\psi}, \tilde{w}, \alpha)$ with $(\psi_o, w_o, \tilde{\psi}_o, \tilde{w}_o, \alpha_o)$ as the initial guess to Newton's method. For the symmetric subspace, X_s , ψ and w are expressed as:

$$\psi = \sum_{m=0}^{N_x-1} \sum_{n=0}^{N_y-1} C_{mn}^{\psi} X_m^{\psi}(\tilde{x}) Y_n^{\psi}(\tilde{y}) \quad (3.54)$$

$$w = \sum_{m=0}^{N_x-1} \sum_{n=0}^{N_y-1} C_{mn}^w X_m^w(\tilde{x}) Y_n^w(\tilde{y}) \quad (3.55)$$

where the expansions coefficients are:

$$X_l^w(\tilde{x}) = T_{l+2}(\tilde{x}) - T_l(\tilde{x}) \quad (3.56)$$

$$Y_l^w(\tilde{y}) = T_{2l+2}(\tilde{y}) - T_{2l}(\tilde{y}) \quad (3.57)$$

$$X_l^{\psi}(\tilde{x}) = (l+1)T_{l+4}(\tilde{x}) - 2(l+2)T_{l+2}(\tilde{x}) + (l+3)T_l(\tilde{x}) \quad (3.58)$$

$$Y_l^{\psi}(\tilde{y}) = (2l+2)T_{2l+5}(\tilde{y}) - 2(2l+3)T_{2l+3}(\tilde{y}) + (2l+4)T_{2l+1}(\tilde{y}) \quad (3.59)$$

For the antisymmetric subspace, X_a , $\tilde{\psi}$ and \tilde{w} are expressed as:

$$\tilde{\psi} = \sum_{m=0}^{N_x-1} \sum_{n=0}^{N_y-1} \tilde{C}_{mn}^{\psi} X_m^{\psi}(\tilde{x}) Y_n^{\psi}(\tilde{y}) \quad (3.60)$$

$$\tilde{w} = \sum_{m=0}^{N_x-1} \sum_{n=0}^{N_y-1} \tilde{C}_{mn}^w X_m^w(\tilde{x}) Y_n^w(\tilde{y}) \quad (3.61)$$

where the expansions functions are defined as:

$$\tilde{X}_l^w(\tilde{x}) = T_{l+2}(\tilde{x}) - T_l(\tilde{x}) \quad (3.62)$$

$$\tilde{Y}_l^w(\tilde{x}) = T_{2l+3}(\tilde{x}) - T_{2l+1}(\tilde{x}) \quad (3.63)$$

$$\tilde{X}_l^\psi(\tilde{x}) = (l+1)T_{l+4}(\tilde{x}) - 2(l+2)T_{l+2}(\tilde{x}) + (l+3)T_l(\tilde{x}) \quad (3.64)$$

$$\tilde{Y}_l^\psi(\tilde{x}) = (2l+1)T_{2l+4}(\tilde{x}) - 2(2l+2)T_{2l+2}(\tilde{x}) + (2l+3)T_{2l}(\tilde{x}) \quad (3.65)$$

The extended system is solved by Newton's method for, $(C_{mn}^w, C_{mn}^\psi, \tilde{C}_{mn}^w, \tilde{C}_{mn}^\psi, \alpha)$.

3.4 Results and Discussion

A comprehensive study of flow through a rotating straight duct is reported by Nandakumar *et al.* (1991). They reported three symmetric and two asymmetric solutions at $Ro = 5$. They used a finite difference approach for solving governing equations describing flow through a straight duct. In order to investigate unfolding of the bifurcation structure of a rotating straight duct with heating the complete bifurcation diagram without heating is required. The focus of the present study is to get such a complete bifurcation diagram with our code. This code is written using numerical schemes based on spectral approximation. The recomputations are performed for the same parameters as used by Nandakumar *et al.* (1991) with the present code for the purpose of code verification. Our computations reveals a bifurcation diagram similar to that obtained by Nandakumar *et al.* (1991). In addition to the five solutions they reported, we obtained two asymmetric solutions through a pitchfork bifurcation on the primary branch of four-cell flow structure. Thus our study obtains a total of three symmetric and four asymmetric solutions at $Ro = 5$.

Although, the choice of numerical schemes depends largely upon the required accuracy and available computational time, it is worthwhile to try different schemes to solve a problem. Because of the global nature of trial functions in spectral methods, the error propagation in the computational domain is uniform. This is in contrast to the finite-difference based method where the error is local in nature and if it is not suppressed by some dissipative mechanism, can destroy the solution. In most practical applications the benefit of spectral methods is its superior accuracy, smaller grids and thus less computational time (Canuto *et al.*, 1988). The spectral approximation gives a dense system of matrices which were solved using LAPACK subroutines (Anderson *et al.*, 1992). Using this method we could find solutions for 17 Chebyshev nodes similar to 39×39 grid used by Nandakumar *et al.* (1991). In contrast to dense matrices, the finite difference discretization based code requires solution of only sparse matrices for which efficient SPARSPACK routines (Chu *et al.*, 1984) are available. Table 3.1 shows the singular points computed for different grid size. These are not very sensitive to grid refinement.

In the asymptotic limits of slow($Ek \rightarrow \infty$ and $Ro \ll Ek$) and rapid($Ek \rightarrow 0$ and $Ro \ll \sqrt{Ek}$) rotation, the flow structure is shown in Figure 3.2 and Figure 3.3 respectively. When the duct rotates slowly, the flow is nearly rectilinear and the flow satisfies Poisson's equation. Figure 3.2 shows the effect of a slight amount of rotation, included as a perturbation to rectilinear flow. A small amount of rotation forces a typical two-dimensional flow structure consisting of two counter rotating vortices in the plane perpendicular to the flow direction. Note that the secondary flow is very weak and hence the departure from one-dimensional rectilinear flow is minimal. In the limit of rapid rotation(Figure 3.3), flow in the core of the duct is geostrophic(i.e., dominated by a Coriolis force which balances pressure gradient) and surrounded by thin viscous boundary layers. For an intermediate value of

$Ek = 0.01$, Coriolis and viscous effects compete with each other and thus solution multiplicity can be expected. A unique solution exists for low values of the Rossby number. For low values of Ro , the governing equations tend to become linear and thus can be solved easily by employing zero initial profiles for the streamwise velocity and stream functions. At higher values of Ro , convective inertia terms make the equations nonlinear and the subsequent interaction of viscous and Coriolis forces develops further vortices through bifurcations. The bifurcation diagrams are illustrated in Figure 3.4 with the dimensionless flow rate (Q) as the state variable, which is calculated from

$$Q = \int_{-0.5}^{+0.5} \int_{-0.5}^{+0.5} w dx dy = \frac{1}{4} \sum_{m=0}^{N_x-1} \sum_{n=0}^{N_y-1} \int_{-1}^{+1} \int_{-1}^{+1} C_{mn}^w X_m(\tilde{x}) Y_n(\tilde{y}) d\tilde{x} d\tilde{y} \quad (3.66)$$

In order to reveal both branches of asymmetric solutions either the stream function, ψ or the streamwise velocity, w on a point away from the line of symmetry is chosen as the state variable. The spatial location of this point is chosen as $(x=-0.45, y=0.05)$, since the flow profile changes most significantly in this region and thus both branches of any asymmetric solution will be made visible. The bifurcation diagrams for these state variables are shown in Figure 3.5, and Figure 3.6.

Various parts of the solution branches were constructed using the following general approach. Starting from $Ro = 0$ and using Euler continuation the solution branch was computed until the Rossby number was close to the limit point, $L2$, as labelled in Figure 3.6. Near the limit point, the Newton's method fails to converge quadratically because of the absence of an isolated solution. Thus, it is necessary to switch to the arclength method to turn around the limit point. The complete branch PM was obtained using arclength continuation. We obtained two limit points $L1$ and $L2$ on the primary branch. Our computations obtained $L1$ and $L2$ at $(Ro = 1.18220)$ and $(Ro = 1.63560)$ respectively. Nandakumar *et al.* (1991) obtained $L1$ and $L2$ at $(Ro = 1.17851)$ and $(Ro = 1.57164)$ respectively. Thus, our

results are in close agreement with the study of Nandakumar *et al.* (1991). The comparison of all the singular points is illustrated in Table 3.2.

Near the limit point $L2$, a symmetry breaking point, $SB1$, exists and an asymmetric branch originates from there. A regular solution on the asymmetric branch was readily generated by starting with a solution just below $L2$, tilting the duct by 1° , increasing Ro past $L2$, and finally bringing the tilt back to 0° . The branch $AS1$ is then completed using arclength continuation scheme. The branch $AS1$ turns around and forms a closed loop. The presence of additional singular points was checked in the region of the turning point at the far end of the asymmetric branch $AS1$. In this way almost coinciding singular points $L3$ and $SB2$ were found. This suggests that an isolated symmetric branch separate from PM must exist. A regular solution on this branch, $IS1$, was easily generated by starting with a solution just below $SB2$ as an initial guess and solving at value of Ro just above $SB2$. Then continuing with arclength scheme in either direction, the entire $IS1$ that lies with in $Ro \leq 5$ was computed. During this computation the arclength continuation scheme turned around three additional limit points, $L3$, $L4$ and $L5$, the precise location of which were computed using the extended system.

Note that the two pairs of singular points $(L2, SB1)$ and $(L3, SB2)$ are close. Whether or not each pair represents a single point of higher nullity in the continuous problem and their separation is an artifact of the numerical discretization can not be ascertained at present. The reflective symmetry that is present at zero degrees is, however, destroyed with even a slight degree of tilt. The solution branches near symmetry breaking points unfold into smooth processes with such a perturbation. To accommodate this possibility, we expected to find another symmetry breaking point, $SB3$, near $L4$ and an asymmetric branch to originate from there. Using steps outlined earlier the singular points $SB3$ and the branch $AS2$ were located. The

limit points $L1$ and $L5$ are the only isolated ones i.e. without a nearby symmetry breaking point. We were able to obtain all five solutions reported by Nandakumar *et al.* (1991). The continuation method does not guarantee that all possible solutions are located for a specific problem. In particular, the chance of detecting isolated branches is small. For some problems it might be worthwhile to solve the governing equations for a random choice of parameters and to check whether the solution is part of the already constructed branching diagram. When a new solution is found, its branch diagram can be constructed using the continuation method. If we perturb slightly the solutions obtained by the continuation procedure and then remove the perturbation, the solution is sometimes attracted to other isolated solutions that are not on the branches already traced by the continuation method. Using this approach we found two additional asymmetric solutions on the branch $AS3$, bifurcating at $SB4$ from the four-cell primary branch PM . This is a typical supercritical pitchfork bifurcation. A buoyancy force perturbation to flow in a rotating duct was used to obtain additional solutions. This is discussed in the next chapter.

At $Ro = 1.3$ three solutions are present and all of them lie on the branch PM . Figure 3.7 shows the flow profiles for the three solutions present at $Ro = 1.3$. Figures 3.7(a), 3.7(b) and 3.7(c) show the streamline contours, streamwise velocity perspective plots and streamwise contour plots of a two-cell flow pattern on PM just before the limit point $L2$. Figures 3.7(d-f) show similar profiles on that part of the branch PM which lies between $L1$ and $L2$. An additional pair of weak cells begins to form on the $(x = -0.5, y)$ wall. Upon turning around limit point $L1$, a strong four-cell pattern is seen to emerge. The stream function and streamwise velocity profile in this region change quite significantly and hence the choice of $\psi(-0.45, 0.05)$ and $w(-0.45, 0.05)$ as the state function in Figures 3.5 and 3.6 respectively are seen to be the sensitive indicator of changes in flow pattern on different parts of the

solution branches. Similar profiles at $Ro = 5$ are discussed, referring to Figure 3.6. *Point 1* is on the branch PM and corresponds to a strong four-cell pattern. The flow structure of this solution is shown in Figure 3.8. The streamline contour plot as shown in Figure 3.8(a) is a strong four-cell flow. Figure 3.8(b and c) show streamwise velocity perspective plot and streamwise velocity counter plots. *Point 2* is on one end of the branch $IS1$ and corresponds to a two-cell pattern. Figures 3.8(d-f) show the solution structure correspond to this solution. *Point 3* is on the other end of the branch $IS1$ and corresponds to a new four-cell pattern. This flow structure is shown in Figures 3.8(g-i). *Point 5* is on the asymmetric branch $AS2$ and the flow profiles at *point 4* are the mirror images of those at *point 5*. The flow structure for the pair of two-cell asymmetric solution is shown in Figure 3.9. The asymmetric solutions obtained as a pitchfork bifurcation on a four-cell branch, PM are shown in Figure 3.10. These correspond to *point 6* and *point 7* in Figures 3.4, 3.5 and 3.6. This pair of solutions was not reported in the study of Nandakumar *et al.* (1991).

Due to the limited scope of the present study we did not perform the stability analysis again. It has been reported by Nandakumar *et al.* (1991). Their study shows that PM remains stable until the limit point $L2$. Passing through $L3$ they found two positive eigenvalues, one corresponding to symmetric solution and the other corresponding to asymmetric solution. Thus, the middle branch of PM is unstable. On turning around the limit point $L1$ the eigenvalue corresponding to symmetric mode becomes negative. Therefore, PM having a four-cell flow structure is left with only one positive eigenvalue corresponding to the asymmetric mode. Hence, the four-cell flow is unstable to asymmetric perturbation and stable to symmetric perturbation. A similar result was obtained in Chapter 2 for the stability study of four-cell solutions for a flow in circular straight duct rotating

about a perpendicular axis. The solution branch *AS1* is unstable. All two-dimensional solutions at $Ro = 5$ were found to be unstable against two-dimensional perturbations.

3.5 Conclusion

Flow in a duct of rectangular cross section is shown to exhibit multiple solutions when the duct is rotated perpendicular to the axis of duct. The interaction of Coriolis, inertial and viscous forces gives rise to a secondary flow. At higher values of the Rossby number, governing equations become nonlinear and show multiple solutions. The results obtained are in good agreement with the study of Nandakumar *et al.* (1991). These are verified by a different numerical discretization schemes based on spectral approximation. Two new solutions which bifurcate from the primary four-cell symmetric branch are also shown to exist. With these two additional solutions, a total of seven solutions at $Ro = 5$ are reported.

	L1	L1	L2	L2
	Ro	Q	Ro	Q
13 × 13	1.17801	2.12717	1.63590	2.08978
17 × 17	1.18220	2.12705	1.63560	2.09900
21 × 21	1.18291	2.12599	1.63481	2.09010
25 × 25	1.18211	2.12839	1.63502	2.08997

Table 3.1: Numerical sensitivity to γ ($\gamma = 1.0$, $Ek = 0.01$, and $\phi = 0^\circ$).

Singular points	Branch	Ro(Nandakumar et al. 2011)	Ro(present study)
L1	PM	1.17851	1.18220
L2	PM	1.57164	1.63560
L3	IS1	2.79654	2.33029
L4	IS1	2.87313	2.77541
L5	IS1	2.61983	2.67194
SB1	PM and AS1	1.55812	1.62391
SB2	IS1 and AS1	2.80513	2.33106
SB3	IS1 and AS2	2.85347	2.75556
SB4	PM and AS3	—	3.02177

Table 3.2: Computed singular points ($\gamma = 1.0$, $Ek = 0.01$, and $\phi = 0^\circ$) for 17×17 .

$$\gamma = \frac{b}{a} \quad Ek = \frac{\nu}{b^2 \Omega} \quad Ro = \frac{U}{b \Omega}$$

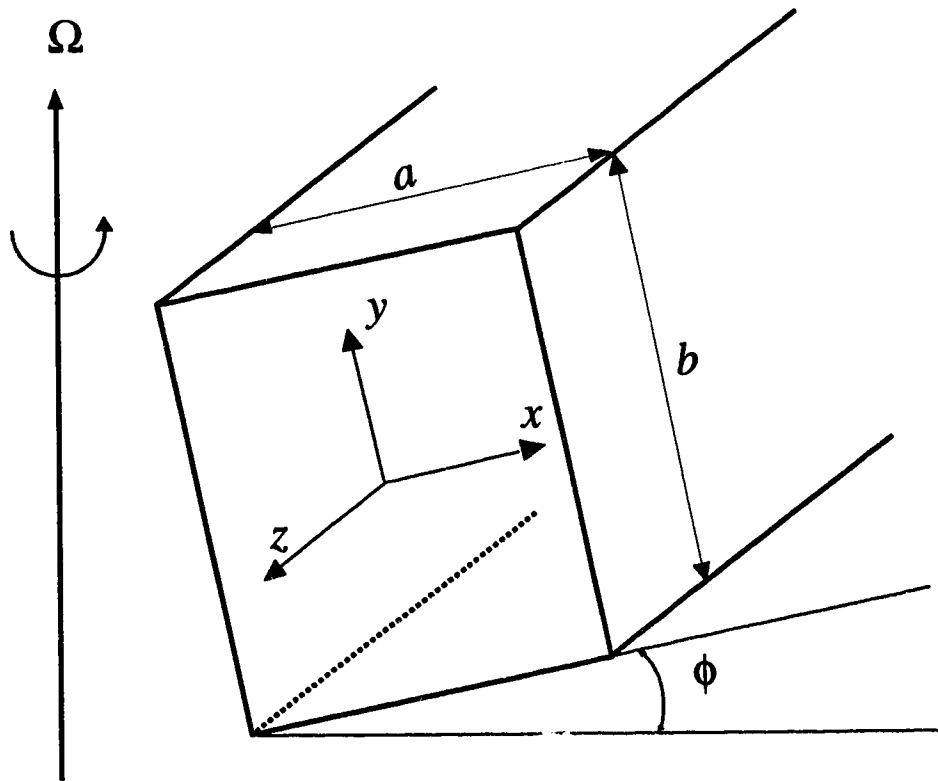


Figure 3.1: Geometry and coordinate system

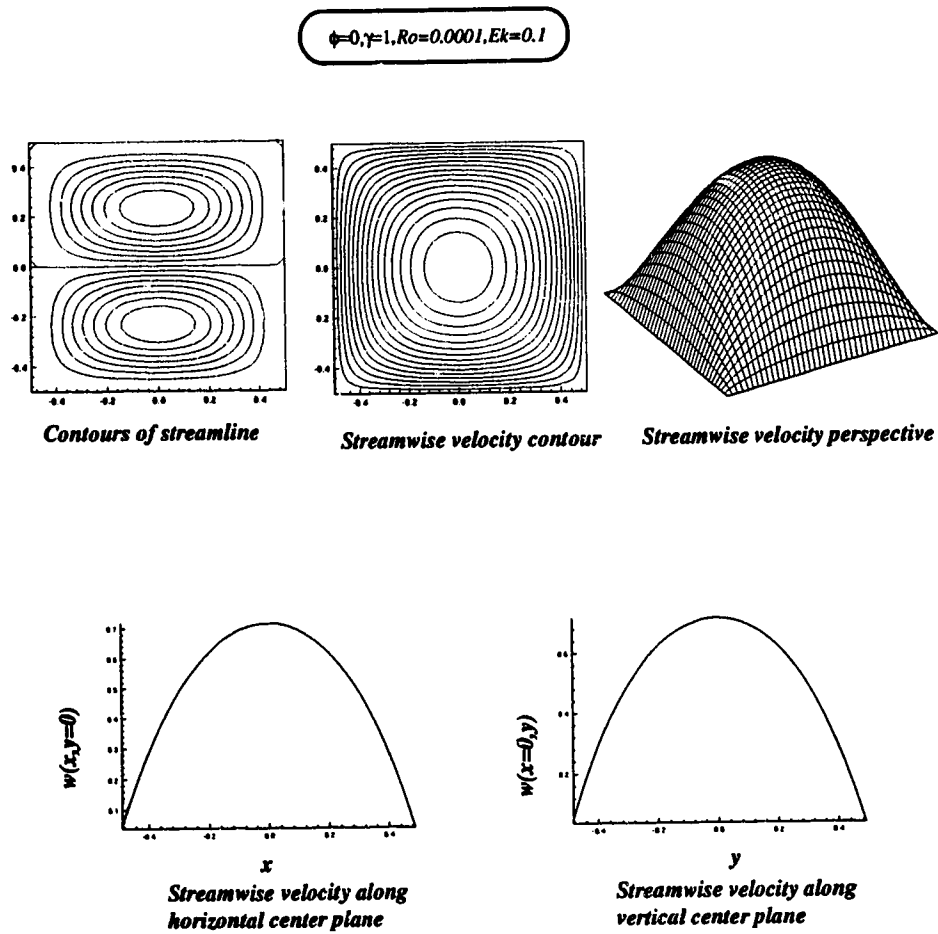


Figure 3.2: This figure shows the asymptotic limit of slow rotation for $Ek = 0.1, \gamma = 1.0, \phi = 0^\circ, Ro = 10^{-4}$.

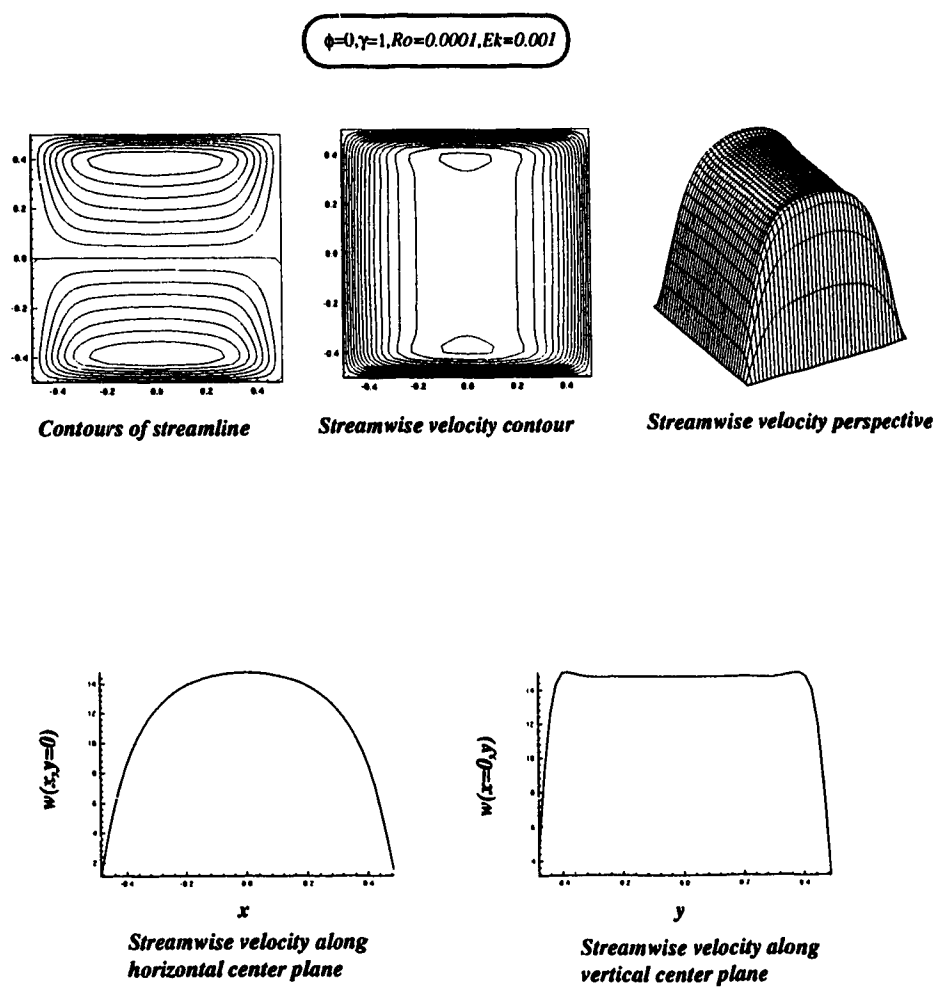


Figure 3.3: This figure shows the asymptotic limit of rapid rotation for $Ek = 0.001, \gamma = 1.0, \phi = 0^\circ, Ro = 10^{-4}$.

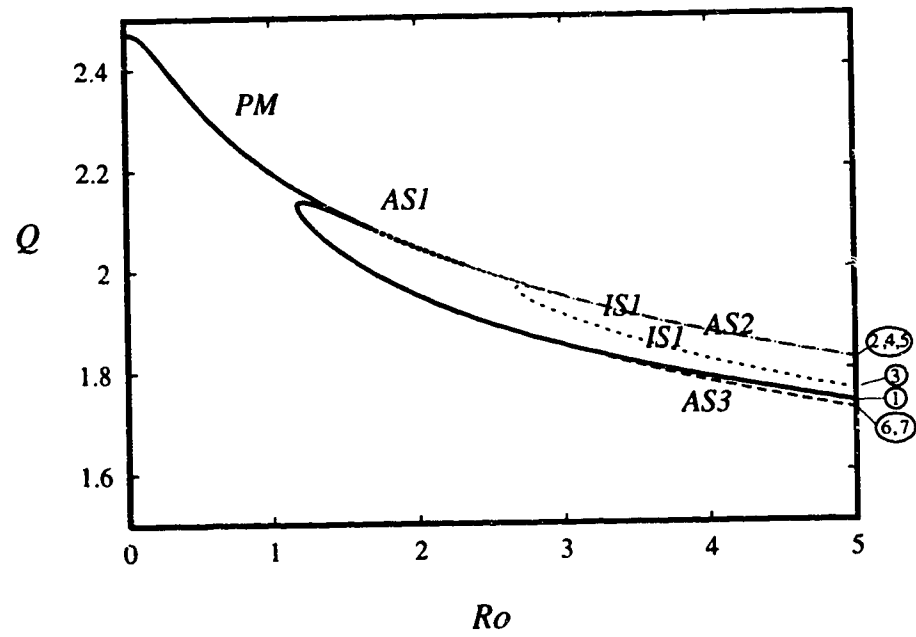


Figure 3.4: State diagram shows dimensionless flow rate vs. Rossby number at $Ek = 0.01, \gamma = 1.0, \phi = 0^\circ$.

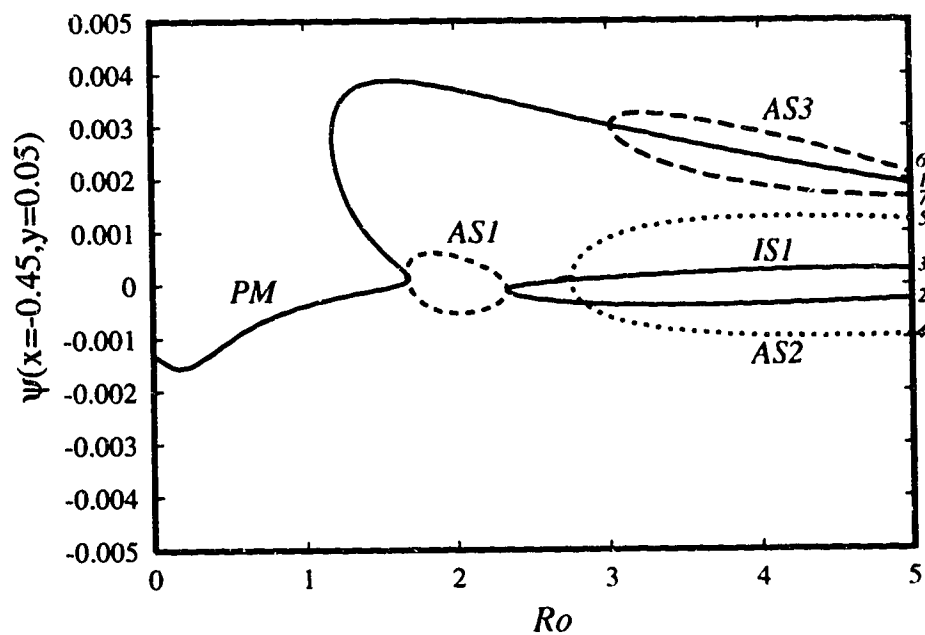


Figure 3.5: State diagram shows dimensionless stream function at $x = -0.45$ and $y = 0.05$ vs. Rossby number at $Ek = 0.01, \gamma = 1.0, \phi = 0^\circ$.

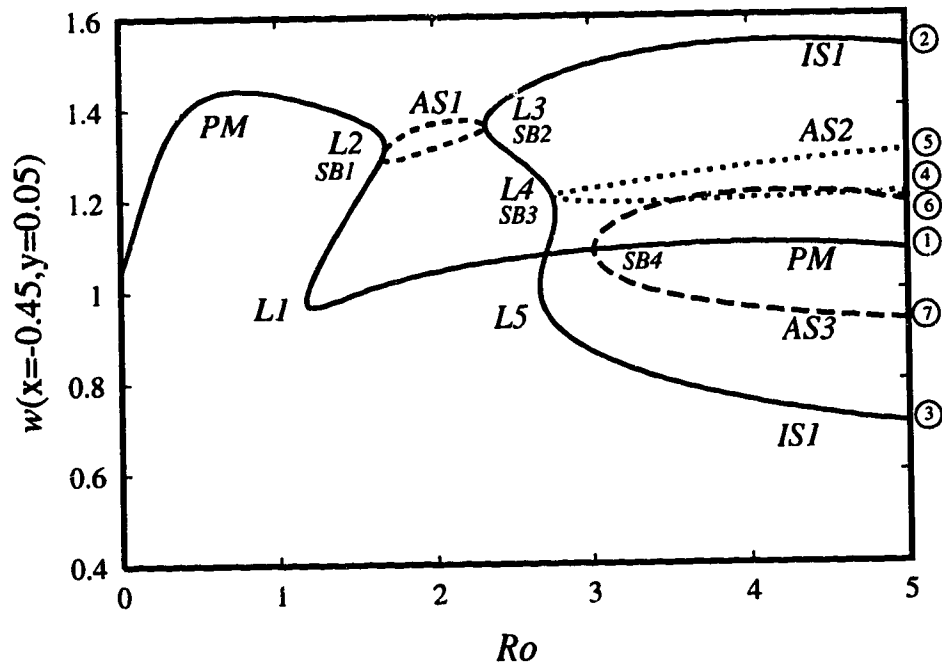


Figure 3.6: State diagram shows dimensionless streamwise velocity at $x = -0.45$ and $y = 0.05$ vs. Rossby number at $Ek = 0.01, \gamma = 1.0, \phi = 0^\circ$.

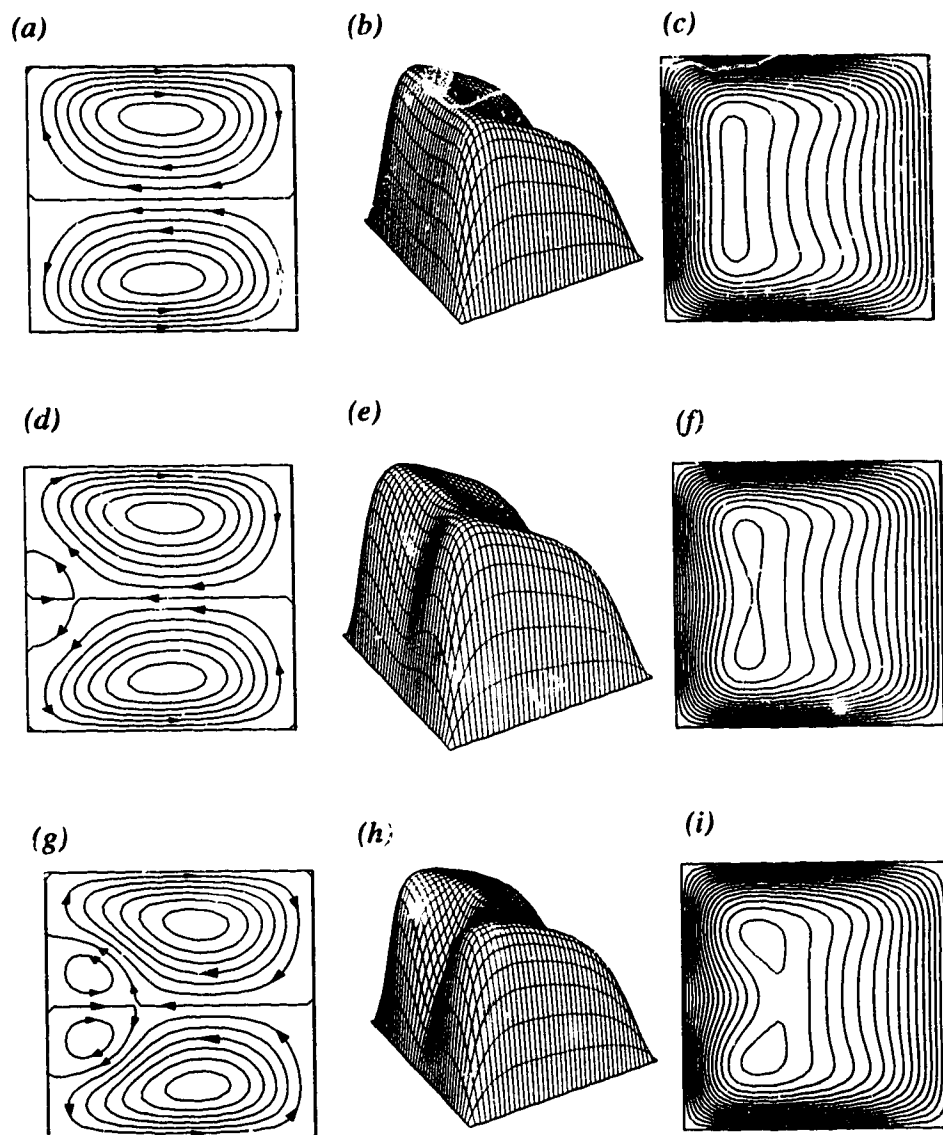


Figure 3.7: Three solutions are present on the primary branch PM at $Ro = 1.3$ and $Ek = 0.01, \gamma = 1.0, \phi = 0^\circ$. These three solutions are on the primary branch originating from $Ro = 0$, intermediate branch connecting $L1$ and $L2$ and after turning around $L1$ respectively.

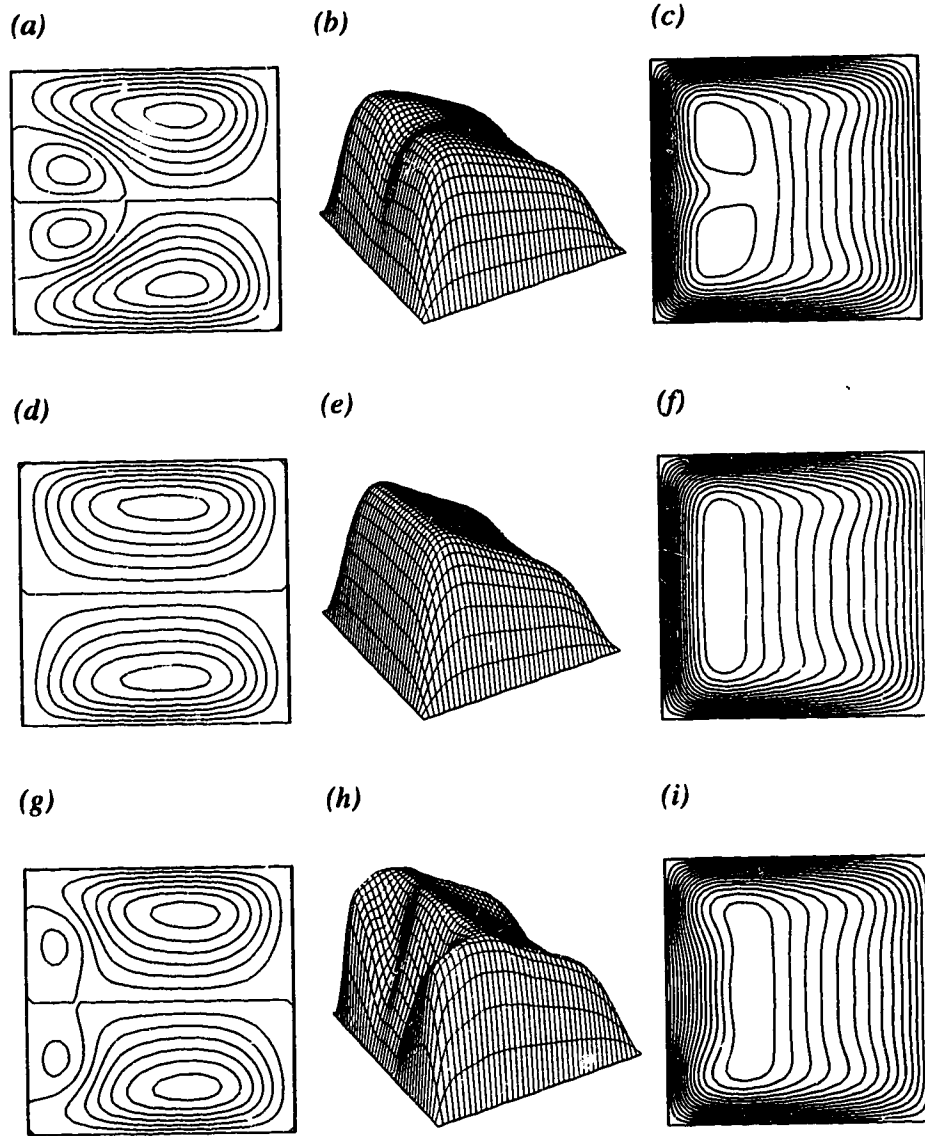


Figure 3.8: Three symmetric are solutions present at $Ro = 5.0$ and $Ek = 0.01, \gamma = 1.0, \phi = 0^\circ$. These correspond to *point 1*, *point 2* and *point 3* in the state diagram, Figure 3.6.

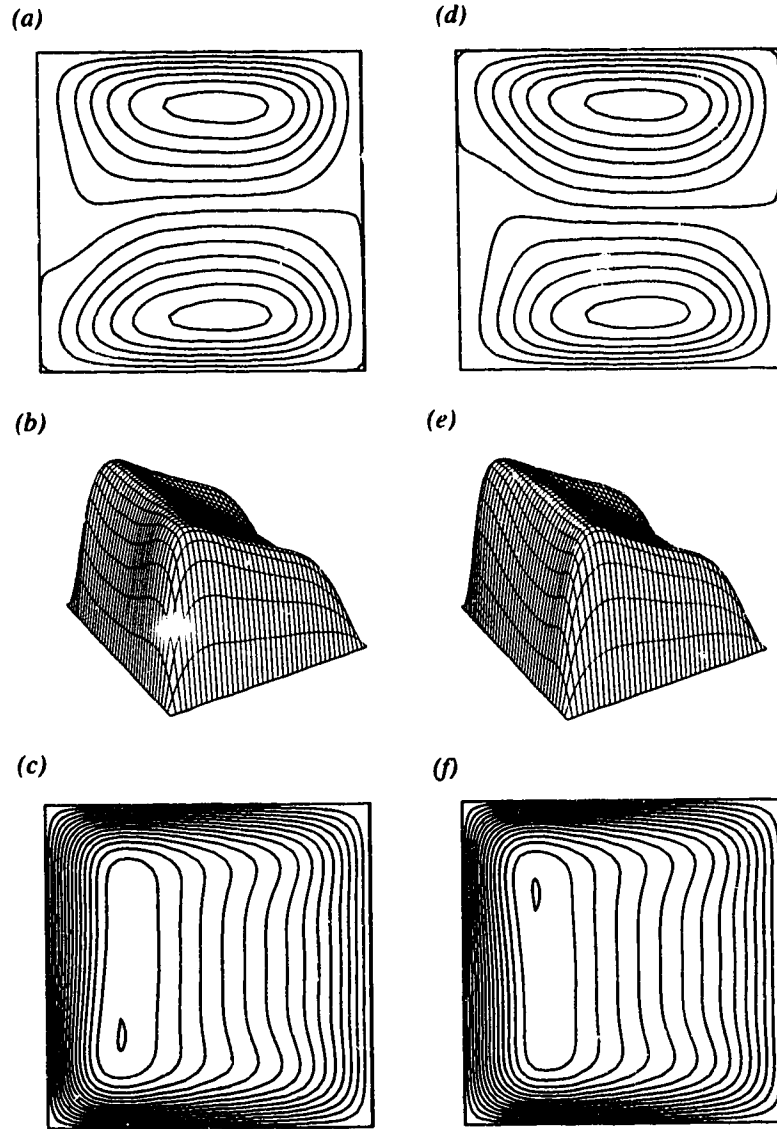


Figure 3.9: Two two-cell asymmetric solutions present at $Ro = 5.0$ and $Ek = 0.01, \gamma = 1.0, \phi = 0^\circ$. These correspond to *point 4* and *point 5* in the state diagram, Figure 3.6.

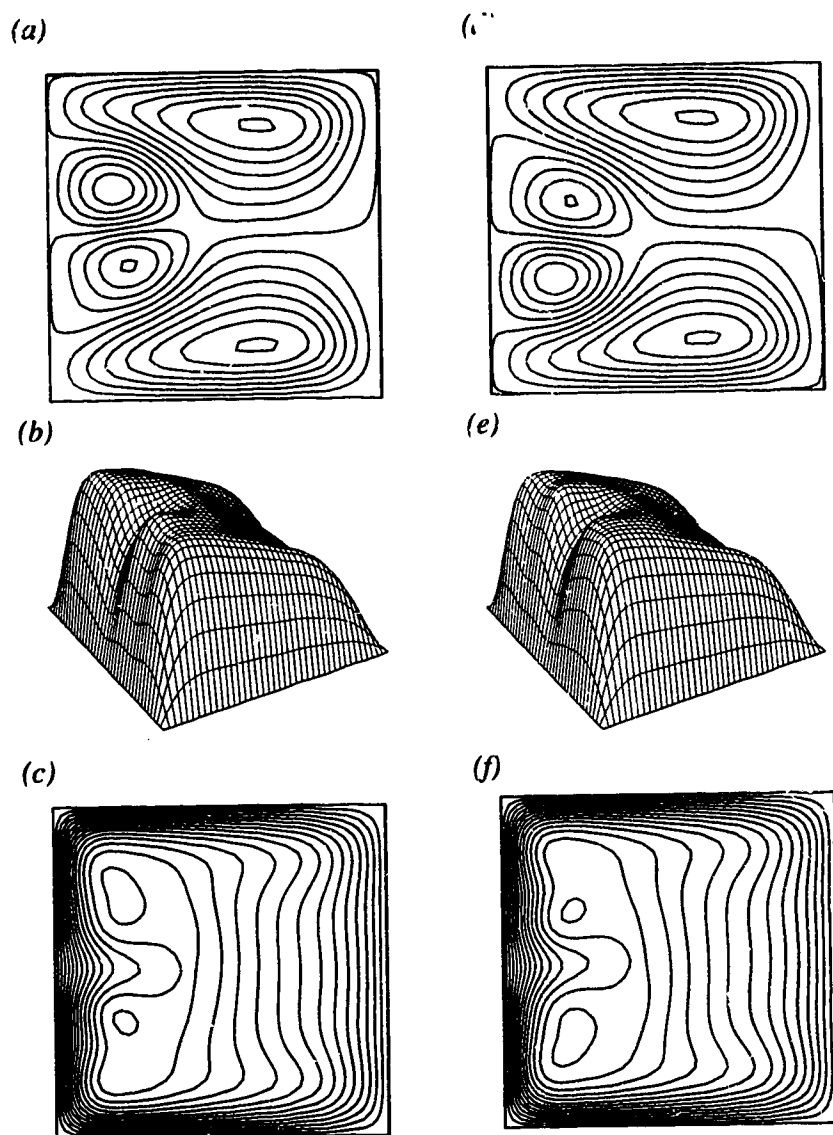


Figure 3.10: Two four-cell asymmetric solutions present at $Ro = 5.0$ and $Ek = 0.01$, $\gamma = 1.0$, $\phi = 0^\circ$. These correspond to *point 6* and *point 7* in the state diagram, Figure 3.6.

References

- ANDERSON, E., BAI, Z., BISCHOF, C., DEMMEL, J., DONGARRA, J.,
CROZ, J. DU, GREENBAUM, A., HAMMARLING, S., MCKENNEY, A.,
OSTROUCHOV, S., & SORENSEN, D. 1992. *LAPACK User's Guide*. SIAM.
- BARUA, S.N. 1954. Secondary flow in a rotating straight pipe. *Proc. Roy. Soc. London A.*, **227**, 133.
- BENTON, G.S. 1956. The effect of earth's rotation on laminar flow in pipes. *J. Appl. Mech.*, **23**, 123.
- BENTON, G.S., & BOYER, D. 1966. Flow through a rapidly rotating conduit of arbitrary cross-section. *J. Fluid Mech.*, **26**, 69.
- CANUTO, C., HUSSAINI, M.Y., QUARTERONI, A., & ZANG, T.A. 1988. *Spectral Methods in Fluid Dynamics*. Springer-Verlag.
- CHU, E., GEORGE, A., & NG, E. 1984. Department of Computer Science, University of Waterloo. *SPARSPACK, Research Report No. CS-84-36*.
- DEAN, W.R. 1927. Note on the motion of fluid in a curved pipe. *Phil. Mag*, **4**, 208.
- DEAN, W.R. 1928. The Streamline motion of fluid in a curved pipe(second paper). *Phil. Mag*, **7**, 673.

- DUCK, P.W. 1983. Flow through rotating straight pipes of a circular cross section. *Phys. Fluids*, **26**, 614.
- ITO, H., & K.NANBU. 1971. Flow in a rotating straight pipes of circular cross section. *Trans. ASME D: J.Basic Engng*, **93**, 383.
- KHESHGI, HAROON S., & SCRIVEN, L.E. 1985. Viscous flow through a rotating square channel. *Phys. Fluids*, **28**, 2968.
- MANSOUR, K. 1985. Laminar flow through a slowly rotating straight pipe. *J. Fluid Mech.*, **150**, 1.
- MOORE, G., & SPENCE, A. 1980. The calculation of turning points of non-linear equations. *SIAM J. Numer. Anal.*, **17**, 567.
- MORI, Y., & NAKAYAMA, W. 1968. Convective heat transfer in a rotating radial circular pipes. *Intl. J. Heat Mass Transfer*, **11**, 1027.
- NANDAKUMAR, K., RASZILLIER, H., & DURST, F. 1991. Flow through rotating rectangular ducts. *Phys. Fluids A*, **3**, 770.
- SPENCE, A., & WERNER, B. 1982. Non-simple turning points and cusps. *IMA J. Numer. Anal.*, **2**, 413.
- SPEZIALE, CHARLES G. 1982. Numerical study of viscous flow in rotating rectangular ducts. *J. Fluid Mech.*, **122**, 251.
- WEINITSCHKE, H.J. 1985. On the calculation of limit and bifurcation points in stability problems of elastic shells. *Int. J. Solids Structures*, **21**, 79.
- WINTERS, KEITH H. 1987. A bifurcation study of laminar flow in a curved tube of rectangular cross-section. *J. Fluid Mech.*, **180**, 343.

Chapter 4

Non-isothermal flow in a rotating duct

4.1 Introduction

In this chapter we investigate the bifurcation of steady laminar mixed convection flow through a duct rotating about an axis perpendicular to its own. The simultaneous presence of buoyancy and Coriolis forces modify the secondary flow in an interesting fashion. These forces, when individually present, drive the secondary flow in directions orthogonal to each other. As a consequence of this, their simultaneous presence modifies the two-dimensional primary flow of two counter rotating vortices in the cross-section of the duct.

Our present problem can be understood as a natural extension of two widely studied problems: mixed convection heat transfer in horizontal ducts, and isothermal flow through a rotating ducts. The problem under investigation reduces to these problems in the asymptotic limits of zero rotation and zero buoyancy respectively.

The problem of mixed convection heat transfer in horizontal duct is also known as the Morton problem after the work by Morton(1959). Following this, numerous papers discussed this issue. Among these, Iqbal & Stachiewicz(1966) and Faris & Viskanta(1969) used a perturbation approach along the lines of Morton (1959). A two-cell flow structure was observed by Cheng & and Hwang(1969) and Hwang & Cheng(1970). They used finite difference based numerical methods to study the problem of mixed convection. Patankar, Ramadhyani & Sparrow(1978) examined the effect of non-uniform peripheral heating in a duct of circular cross-section. They showed a transition to a four-cell flow structure. A similar transition is also reported by Chou & Hwang(1984) for rectangular geometry with uniform heating. Dual solutions were observed by Nandakumar *et al.* (1985) in their study of mixed-convection flow in horizontal ducts of rectangular, circular and semicircular cross-sections. A much richer solution structure with up to five solutions over certain ranges of Grashoff number was reported by Nandakumar & Weinitchke(1991).

In the other asymptotic limit of flow through a rotating duct under isothermal conditions, a detailed bifurcation study is reported in Chapter 3. In this chapter, the effect of buoyancy force on the bifurcation diagram obtained in Chapter 3 is investigated. In particular, we are interesting in finding out how the unfolding of various bifurcation points occur in the presence of a buoyancy force.

The combined effect of rotation and heating have been addressed in many papers. A combined free and forced convective heat transfer in a rotating curved circular tube has been investigated by Wang & Cheng(1995). An extensive review of heat transfer in rotating channels has been presented in a review monograph by Morris(1981). An experimental study of convective heat transfer in radially rotating rectangular ducts was presented by Soong *et al.* (1991).

4.2 Governing Equations

The governing equations for flow through a rotating duct under non-isothermal conditions can be obtained as a natural extension to the equations under isothermal conditions. In order to study the effect of buoyancy, we modify the governing equations considered in Chapter 3 (hereinafter referred to as *I*), by treating the body force terms as temperature dependent and including an energy equation. This allows us to use the solutions obtained in *I* for studying the effect of buoyancy. Therefore, to have a consistency in notation and numerical procedure, we consider the same geometry and coordinate system as used in *I*, a rectangular duct of width a and height b , with an aspect ratio defined as $\gamma = b/a$. The axis of the duct is aligned perpendicular to the gravity vector. The duct is rotating along an axis perpendicular to its own at a rate Ω . The cross-section of the duct is tilted by ϕ° with respect to the gravity vector as shown in figure 4.1. We recall, in *I*, the tilt was used as a means for obtaining asymmetric solutions. In this problem, the buoyancy itself breaks symmetry, thus, the purpose of keeping tilt is only to have a consistency in equations. Also, the potential $\hat{\phi}$ in *I* now combines centrifugal and thermodynamic pressure only. The flow is driven by a constant imposed pressure gradient $\frac{\partial \hat{\phi}}{\partial \hat{z}}$, and heated by an streamwise uniform flux $\frac{\partial \hat{\theta}}{\partial \hat{z}}$. Thus the streamwise invariant state is assumed to exist. With these premises, the governing equations describing flow and energy are:

continuity equation

$$\frac{\partial \hat{u}}{\partial \hat{x}} + \frac{\partial \hat{v}}{\partial \hat{y}} = 0 \quad (4.1)$$

x -momentum

$$\frac{\partial \hat{u}}{\partial \hat{t}} + \left(\hat{u} \frac{\partial \hat{u}}{\partial \hat{x}} + \hat{v} \frac{\partial \hat{u}}{\partial \hat{y}} \right) = -\frac{\partial \hat{\phi}}{\partial \hat{x}} + \frac{\mu}{\rho_r} \hat{\nabla}^2 \hat{u} - 2 \frac{\rho}{\rho_r} \Omega \hat{w} \cos \phi - g \frac{\rho}{\rho_r} \sin \phi \quad (4.2)$$

y-momentum

$$\frac{\partial \hat{v}}{\partial \hat{t}} + \left(\hat{u} \frac{\partial \hat{v}}{\partial \hat{x}} + \hat{v} \frac{\partial \hat{v}}{\partial \hat{y}} \right) = -\frac{\partial \hat{\varphi}}{\partial \hat{y}} + \frac{\mu}{\rho_r} \hat{\nabla}^2 \hat{v} + 2 \frac{\rho}{\rho_r} \Omega \hat{w} \sin \phi - g \frac{\rho}{\rho_r} \cos \phi \quad (4.3)$$

z-momentum

$$\frac{\partial \hat{w}}{\partial \hat{t}} + \left(\hat{u} \frac{\partial \hat{w}}{\partial \hat{x}} + \hat{v} \frac{\partial \hat{w}}{\partial \hat{y}} \right) = -\frac{\partial \hat{\varphi}}{\partial \hat{z}} + \frac{\mu}{\rho_r} \hat{\nabla}^2 \hat{w} + 2 \frac{\rho}{\rho_r} \Omega (\hat{u} \cos \phi - \hat{v} \sin \phi) \quad (4.4)$$

energy equation

$$\frac{\partial \hat{\theta}}{\partial \hat{t}} + \left(\hat{u} \frac{\partial \hat{\theta}}{\partial \hat{x}} + \hat{v} \frac{\partial \hat{\theta}}{\partial \hat{y}} + \hat{w} \frac{\partial \hat{\theta}}{\partial \hat{z}} \right) = \frac{k}{\rho_r c_p} \hat{\nabla}^2 \hat{\theta} \quad (4.5)$$

Note that a fully developed state implies $\frac{\partial \hat{\theta}}{\partial \hat{z}} = \frac{d\hat{\theta}_b}{d\hat{z}}$. Furthermore, a stronger Boussinesq approximation is invoked to account for the density variation in the gravity term as well as in the Coriolis term.

$$\hat{\rho} = \rho_r [1 - \beta (\hat{\theta} - \hat{\theta}_r)] \quad (4.6)$$

where

$$\beta = -\frac{1}{\rho_r} \left(\frac{\partial \hat{\rho}}{\partial \hat{\theta}} \right)_p$$

is the coefficient of thermal expansion. Here the subscript r denotes a reference state. The equations of motion and energy subject to these conditions are:

continuity equation

$$\frac{\partial \hat{u}}{\partial \hat{x}} + \frac{\partial \hat{v}}{\partial \hat{y}} = 0 \quad (4.7)$$

x-momentum

$$\begin{aligned} \frac{\partial \hat{u}}{\partial \hat{t}} + \left(\hat{u} \frac{\partial \hat{u}}{\partial \hat{x}} + \hat{v} \frac{\partial \hat{u}}{\partial \hat{y}} \right) = & -\frac{\partial \hat{\varphi}}{\partial \hat{x}} + \frac{\mu}{\rho_r} \hat{\nabla}^2 \hat{u} \\ & - 2(1 - \beta (\hat{\theta} - \hat{\theta}_r)) \Omega \hat{w} \cos \phi \\ & - g(1 - \beta (\hat{\theta} - \hat{\theta}_r)) \sin \phi \end{aligned} \quad (4.8)$$

y-momentum

$$\begin{aligned}
\frac{\partial \hat{v}}{\partial \hat{t}} + \left(\hat{u} \frac{\partial \hat{v}}{\partial \hat{x}} + \hat{v} \frac{\partial \hat{v}}{\partial \hat{y}} \right) = & - \frac{\partial \hat{\varphi}}{\partial \hat{y}} + \frac{\mu}{\rho_r} \hat{\nabla}^2 \hat{v} \\
& + 2(1 - \beta (\hat{\theta} - \hat{\theta}_r)) \Omega \hat{w} \sin \phi \\
& - g(1 - \beta (\hat{\theta} - \hat{\theta}_r)) \cos \phi
\end{aligned} \quad (4.9)$$

z-momentum

$$\begin{aligned}
\frac{\partial \hat{w}}{\partial \hat{t}} + \left(\hat{u} \frac{\partial \hat{w}}{\partial \hat{x}} + \hat{v} \frac{\partial \hat{w}}{\partial \hat{y}} \right) = & - \frac{\partial \hat{\varphi}}{\partial \hat{z}} + \frac{\mu}{\rho_r} \hat{\nabla}^2 \hat{w} \\
& + 2\Omega(1 - \beta (\hat{\theta} - \hat{\theta}_r)) (\hat{u} \cos \phi - \hat{v} \sin \phi)
\end{aligned} \quad (4.10)$$

energy equation

$$\frac{\partial \hat{\theta}}{\partial \hat{t}} + \left(\hat{u} \frac{\partial \hat{\theta}}{\partial \hat{x}} + \hat{v} \frac{\partial \hat{\theta}}{\partial \hat{y}} + \hat{w} \frac{\partial \hat{\theta}}{\partial \hat{z}} \right) = \frac{k}{\rho_r c_p} \hat{\nabla}^2 \hat{\theta} \quad (4.11)$$

To get the dimensionless equations of motion and energy, following variables are used to normalize the variables:

$$\begin{aligned}
u = \frac{\hat{u}}{U}, \quad v = \frac{\hat{v}}{U}, \quad w = \frac{\hat{w}}{U}, \quad x = \frac{\hat{x}}{a}, \quad y = \frac{\hat{y}}{b}, \\
\tau = \hat{t}\Omega, \quad \varphi = \frac{\hat{\varphi}}{bU\Omega}, \quad \psi = \frac{\hat{\psi}}{bU}, \\
\Delta\hat{\theta} = b \frac{d\hat{\theta}_b}{dz}, \quad \theta = \frac{\hat{\theta}_r - \hat{\theta}}{\Delta\hat{\theta}}, \quad \eta = \beta \Delta\hat{\theta}
\end{aligned} \quad (4.12)$$

where $U = -\hat{\varphi}_z / \rho\Omega$. The non-dimensional equations take the following form:

continuity equation

$$\gamma \frac{\partial u}{\partial x} + \frac{\partial v}{\partial y} = 0 \quad (4.13)$$

x-momentum

$$\begin{aligned}
\frac{\partial u}{\partial \tau} + Ro \left(\gamma u \frac{\partial u}{\partial x} + v \frac{\partial u}{\partial y} \right) = & - \gamma \frac{\partial \varphi}{\partial x} + Ek \nabla^2 u - 2w(1 + \eta\theta) \cos \phi \\
& - \frac{GvEk^2}{Ro} \eta\theta \sin \phi
\end{aligned} \quad (4.14)$$

y-momentum

$$\begin{aligned} \frac{\partial v}{\partial \tau} + Ro \left(\gamma u \frac{\partial v}{\partial x} + v \frac{\partial v}{\partial y} \right) = & - \frac{\partial \varphi}{\partial y} + Ek \nabla^2 v + 2w(1 + \eta\theta) \sin \phi \\ & - \frac{GvEk^2}{Ro} \eta\theta \cos \phi \end{aligned} \quad (4.15)$$

z-momentum

$$\begin{aligned} \frac{\partial w}{\partial \tau} + Ro \left(\gamma u \frac{\partial w}{\partial x} + v \frac{\partial w}{\partial y} \right) = & 1 + Ek \nabla^2 w \\ & + 2(1 + \eta\theta)(u \cos \phi - v \sin \phi) \end{aligned} \quad (4.16)$$

energy equation

$$\frac{\partial \theta}{\partial \tau} + Ro \left(\gamma u \frac{\partial \theta}{\partial x} + v \frac{\partial \theta}{\partial y} \right) = \frac{Ek}{Pr} \nabla^2 \theta + wRo \quad (4.17)$$

where $\nabla^2 = \gamma^2 \frac{\partial^2}{\partial x^2} + \frac{\partial^2}{\partial y^2}$. In the above equations the dimensionless group $Gv = gb^3/\nu^2$ is the gravity number. This represents the ratio of gravitational to viscous forces. Pr is Prandtl number defined as $C_p\mu/k$.

Since the flow is two-dimensional, continuity implies

$$u = \frac{\partial \psi}{\partial y}, \quad \text{and} \quad v = -\gamma \frac{\partial \psi}{\partial x} \quad (4.18)$$

In the above equation, ψ is a solution of the Poisson equation

$$\nabla^2 \psi + \xi = 0 \quad (4.19)$$

where

$$\xi = \gamma \frac{\partial v}{\partial x} - \frac{\partial u}{\partial y} \quad (4.20)$$

is the streamwise component of the vorticity, which is determined from the z component of the vorticity transport equation given by

$$\frac{\partial \xi}{\partial \tau} = Ek \nabla^2 \xi + Ro \gamma \left(\frac{\partial \psi}{\partial x} \frac{\partial \xi}{\partial y} - \frac{\partial \psi}{\partial y} \frac{\partial \xi}{\partial x} \right) + 2 \left(\gamma \frac{\partial w}{\partial x} \sin \phi + \frac{\partial w}{\partial y} \cos \phi \right) (1 + \eta\theta)$$

$$\begin{aligned}
& - 2 \left(\gamma \frac{\partial \theta}{\partial x} \cos \phi - \frac{\partial \theta}{\partial y} \sin \phi \right) \frac{GvEk^2\eta}{Ro} \\
& + 2\eta w \left(\gamma \frac{\partial \theta}{\partial x} \sin \phi + \frac{\partial \theta}{\partial y} \cos \phi \right)
\end{aligned} \tag{4.21}$$

As a consequence of equation(4.19), it is clear that the secondary flows result from a non-zero streamwise vorticity ξ . Furthermore, from equation(4.21) we see that the body force terms(i.e the Coriolis term and buoyancy term) serve as sources for the streamwise vorticity, and are the driving mechanism for the generation of secondary flows.

If equation(4.19) is substituted into equation(4.21), we obtain an equation in streamfunction form as:

$$\begin{aligned}
\frac{\partial(-\nabla^2\psi)}{\partial\tau} = & -Ek\nabla^4\psi \\
& + Ro\gamma \left[\left(\gamma^2 \frac{\partial^3\psi}{\partial x^3} \frac{\partial\psi}{\partial y} - \frac{\partial\psi}{\partial x} \frac{\partial^3\psi}{\partial y^3} \right) - \left(\gamma^2 \frac{\partial\psi}{\partial x} \frac{\partial^3\psi}{\partial x^2y} + \frac{\partial^3\psi}{\partial xy^2} \frac{\partial\psi}{\partial y} \right) \right] \\
& + 2 \left(\gamma \frac{\partial w}{\partial x} \sin \phi + \frac{\partial w}{\partial y} \cos \phi \right) (1 + \eta\theta) \\
& + 2\eta w \left(\gamma \frac{\partial \theta}{\partial x} \sin \phi + \frac{\partial \theta}{\partial y} \cos \phi \right) \\
& - 2 \left(\gamma \frac{\partial \theta}{\partial x} \cos \phi - \frac{\partial \theta}{\partial y} \sin \phi \right) \frac{GvEk^2\eta}{Ro}
\end{aligned} \tag{4.22}$$

where

$$\nabla^4 = \gamma^4 \frac{\partial^4}{\partial x^4} + 2\gamma^2 \frac{\partial^4}{\partial x^2 y^2} + \frac{\partial^4}{\partial y^4}$$

Similarly, streamwise velocity and energy equations can be written by using u and v in terms of streamfunction as,

$$\begin{aligned}
\frac{\partial w}{\partial \tau} = & 1 + Ek\nabla^2 w + Ro\gamma \left(\frac{\partial\psi}{\partial x} \frac{\partial w}{\partial y} - \frac{\partial\psi}{\partial y} \frac{\partial w}{\partial x} \right) \\
& + 2(1 + \eta\theta) \left(\gamma \frac{\partial\psi}{\partial x} \sin \phi + \frac{\partial\psi}{\partial y} \cos \phi \right)
\end{aligned} \tag{4.23}$$

and

$$\frac{\partial \theta}{\partial \tau} = Ro \gamma \left(\frac{\partial \psi}{\partial x} \frac{\partial \theta}{\partial y} - \frac{\partial \psi}{\partial y} \frac{\partial \theta}{\partial x} \right) + \frac{Ek}{Pr} \nabla^2 \theta + w Ro \quad (4.24)$$

respectively. We have to find stationary solutions of the equations (4.22), (4.23), and (4.24) subject to noslip and impenetrability boundary conditions on the walls of the duct:

$$w = 0, \quad \theta = 0, \quad \psi = 0, \quad \frac{\partial \psi}{\partial x} = 0, \quad \text{and} \quad \frac{\partial \psi}{\partial y} = 0 \quad \text{at} \quad x = \pm \frac{1}{2}, y = \pm \frac{1}{2} \quad (4.25)$$

In order to solve above equations with boundary conditions, we use the spectral approximation for discretization and continuation method for tracking solution paths, as discussed in Chapter 3. For the sake of avoiding repetition, details are not presented here. The solution is always sought over the full 2D domain.

4.3 Results and Discussion

Fluid flow through a uniformly heated, horizontal stationary duct is also known as the Morton problem. The physical mechanism responsible for the existence of multiple solutions in the Morton problem is well understood. An unstable stratified density field exists only near the bottom of the wall when the fluid is heated uniformly with a constant temperature around the periphery. Viscosity acts as a damping mechanism and therefore the primary solution is unique and stable. This solution consists of a secondary flow with two-dimensional counter rotating vortices, driven by the buoyancy force. Because of the presence of a nonlinear coupling between viscous and buoyancy forces, multiple solutions are expected. When the strength of the buoyancy force is increased relative to that of viscous forces, additional solutions bifurcate at certain critical points. The bifurcation study of mixed convection heat transfer in horizontal ducts was examined by Nandakumar

and Weintschke (1991). If we invoke the Boussinesq approximation to account for the density variation only in the buoyancy force term, we get a secondary flow source term $\frac{\partial \theta}{\partial x}$ (Nandakumar & Weinitschke, 1991) in the streamwise vorticity equation for the mixed convection problem. It should be noted that for mixed convection flow, the equations admit symmetric solutions about y-axis. More specifically, for $\phi = 0$, the boundary conditions on the line of symmetry(y-axis) are:

$$\frac{\partial w}{\partial x} = 0, \frac{\partial \theta}{\partial x} = 0, \psi = 0, \xi = 0 \quad (4.26)$$

The additional feature, rotation, can be incorporated by use of a rotating coordinate system, which affects the governing equations. By treating the Coriolis force as a perturbation over mixed convection flow, the effect of rotation on the bifurcation diagram obtained for mixed convection problem by Nandakumar & Weinitschke (1991) can be determined.

The other approach to studying the simultaneous effect of buoyancy and Coriolis forces on flow through a duct could be by treating buoyancy as a perturbation of flow through a rotating duct. The solution and flow structure for the flow in a rotating straight rectangular duct was discussed in the previous chapter. The secondary flow is generated and sustained by the presence of a Coriolis force, which pushes the fluid horizontally across the duct. Two counter-rotating vortices are established as the secondary flow. The interaction of the Coriolis force with the viscous force gives rise to a complicated bifurcation diagram at higher values of Ro . The source term for secondary flow in a rotating duct appears in the streamwise vorticity equation as $\frac{\partial w}{\partial y}$ (Nandakumar *et al.*, 1991). The solution structure is symmetric about the x-axis. For the angle of tilt, $\phi = 0$, the governing equations for the flow in a rotating duct about an axis perpendicular to the duct axis admit the following boundary

conditions about the x-axis($y=0$):

$$\frac{\partial w}{\partial y} = 0, \psi = 0, \xi = 0 \quad (4.27)$$

It should be noted from the above discussion that whenever both buoyancy and Coriolis driven sources of secondary flow ($\frac{\partial \theta}{\partial x}$ and $\frac{\partial w}{\partial y}$ respectively) are present, they break symmetry on $y = 0$ and $x = 0$ respectively. Thus, the governing equations for the present problem only admit asymmetric solutions.

In the present work we have chosen the second approach for studying non-isothermal flow through a rotating duct *i.e.* we impose the buoyancy force on flow through a rotating duct. This study provides a link between the problem of flow through a rotating duct and a mixed convection flow problem. The relative magnitude of the forces driving secondary flow can give the asymmetric solutions present in both the problems. A strong Coriolis effect and a weak buoyancy effect produce solutions similar to the asymmetric solutions obtained for flow in a rotating duct. On the other hand a strong buoyancy effect and a weak Coriolis effect produce solutions similar to those in the Morton problem. When these forces are of a comparable magnitude, a solution structure having a strong degree of asymmetry is obtained. The interplay of these forces is illustrated in Figures 4.2, 4.3 and 4.4. These figures were obtained by keeping Coriolis effect constant (fixing $Ro = 0.1$ and $Ek = 0.01$) and increasing the buoyancy effect through the Grashoff number, Gr . The Grashoff number is obtained indirectly by first computing the average streamwise velocity and mean bulk temperature at a given Ro . Thus, the value of Gr represents buoyancy effect at a specified rotation. The streamwise velocity and temperature scales are chosen such that the mean streamwise velocity does not explicitly appear in the equations of motion. Hence the Grashoff number (defined

as $Gr = b^3 \beta g Q_l / k \nu^2$, where Q_l is heat transfer per unit length) becomes

$$Gr = \frac{2Pr \langle w \rangle \eta Gv Ro}{(1 + \gamma) Ek} \quad (4.28)$$

where $\langle w \rangle$ is the mean streamwise velocity computed as:

$$\langle w \rangle = \frac{\int_{-0.5}^{+0.5} \int_{-0.5}^{+0.5} w dx dy}{Area}$$

Gr can be computed after a solution is obtained for a specified value of η, Gv, Pr, γ, Ek and Ro . For $Ro = 10$ and $Ek = 0.01$ the solution has a two cell flow structure. Figure 4.2 shows the streamwise contour plots at five different Grashoff numbers. The two cell flow structures at $Gr = 172$ and $Gr = 1736$ correspond to a strong rotation effect and a weak buoyancy effect. These flow structures show a weak degree of asymmetry. At higher values of Grashoff number *viz.*, $Gr = 174908$ and $Gr = 1682992$ we obtained two-cell flow structures corresponding to a strong buoyancy effect. At the intermediate value of $Gr = 17380$ a two-cell flow structure having a strong asymmetric effect was obtained. This flow structure corresponds to competing Coriolis and buoyancy effects. Figure 4.3 shows contours of isotherms for five Grashoff numbers, showing the effect of heating. At a sufficiently high value of $Gr = 1682992$, the isotherm resembles that in mixed convection problem. A similar result is shown in Figure 4.4, which shows the contours of streamwise velocity at five different Grashoff numbers. At higher values of Gr , we note a strong degree of asymmetry.

Since buoyancy destroys symmetry in the problem, the symmetry breaking points do not remain robust to this perturbation. This results in a smooth unfolding of the solution branches. The amount of unfolding depends on the degree of asymmetry introduced by buoyancy. First we examined the effect of slight imperfections introduced by heating. The solution structure for $Gv = 10^3, \eta = 10^{-3}, \gamma = 1, \phi = 0^0, Pr = 0.707$ as shown in Figure 4.6 represents state diagrams of streamwise

velocity computed at the $(0.45, 0.05)$. The state diagram shown in Figure 4.6(a) is for flow through a rotating duct in the absence of a buoyancy effect. It was obtained in Chapter 3. It shows two symmetric and three asymmetric branches. The two symmetric solution branches, PM and $IS1$ are connected by an asymmetric branch $AS1$ emanating from a symmetry breaking point, $SB1$ near the limit point $L2$. Other symmetry breaking points, $SB2$ and $SB3$ are present near the limit point $L3$ and $L4$ respectively. An asymmetric branch, $AS2$ originates from the symmetry breaking point, $SB3$. A third asymmetric branch, $AS3$ corresponds to a pitchfork bifurcation, $SB4$, which originates from the PM having four-cell flow structure. Thus, at $Ro = 5$ there exist three symmetric and four asymmetric solutions. When the buoyancy effects are introduced, the symmetry breaking points unfold and all the solutions become asymmetric. The effect of heating is shown in Figure 4.6(b). We observe that the solution branches get disconnected into four branches $B1$, $B2$, $B3$ and $B4$. The branch $B1$ that originates at $Ro = 0$ continues smoothly until $Ro = 5$. All the solutions on this branch have an asymmetric two-cell flow structure. The other three disconnected branches, $B2$, $B3$ and $B4$ have a single limit point. Only the limit points $L1$, and $L5$ remain robust under heating. The unfolded branches $B2$, and $B3$ have limit points $L1^*$ and $L5^*$ respectively. These correspond to $L1$ and $L5$ in the isothermal case. The symmetry breaking point $SB4$ due to pitchfork bifurcation is unfolded into a limit point, $L6^*$, on branch $B4$ in Figure 4.6(b). There are seven different solutions present at $Ro = 5$ and these are numbered as (1-7) in Figure 4.6(b). As evident from Figure 4.6 the presence of buoyancy effect unfolds symmetry breaking bifurcation point by connecting symmetric branch with the asymmetric branch emanating from the symmetry breaking points so that new unfolded branch has only asymmetric solutions. In Figure 4.6(b) a new asymmetric branch, $B1$, is formed by connecting the solution branch PM with the lower solution branch of $AS1$, present in Figure 4.6(a). Thus, on the unfolded branch, $B1$, a two-

cell solution exist up to $Ro = 5$. This flow structure is shown in the contours of streamline in Figure 4.8(d). The corresponding streamwise velocity perspective plot is shown in Figure 4.9(d). The isotherm is shown in Figure 4.10(d). A second asymmetric branch, $B2$, in Figure 4.6(b) connects the upper $IS1$ branch, the upper $AS1$ branch and the upper $AS3$ branch through the limit point $L1$ present in Figure 4.6(a). This limit point is labelled as $L1^*$ in Figure 4.6(b). Unlike, $L1$, the limit point $L1^*$ has an asymmetric solution. $B2$ has a two-cell flow structure at one end and a four-cell flow structure at the other end of the branch at $Ro = 5$. Figures 4.8(b) and 4.8(f) show contours of streamline at $Ro = 5$ on the branch $B2$ and Figures 4.9(b) and 4.9(f) show the streamwise velocity perspective plots at $Ro = 5$ on this branch. The isotherms for this branch at $Ro = 5$ are shown in Figures 4.10(b) and 4.10(f). The third disconnected branch, $B3$, in Figure 4.6(b) connects two-cell solutions on the upper $AS2$ branch and four-cell solutions on $IS1$ branch through a limit point $L5$ present in Figure 4.6(a). This is labelled as $L5^*$ in Figure 4.6(b). The flow structures at $Ro = 5$ for this branch are shown for streamline contours in Figures 4.8(e) and 4.8(c), streamwise velocity perspectives in Figures 4.9(e) and 4.9(c), and corresponding isotherms in Figures 4.10(e) and 4.10(c). Finally, fourth branch, $B4$, corresponds to an unfolded pitchfork bifurcation. This branch connects a four-cell solution at both ends at $Ro = 5$. It connects the lower branch $AS3$ and a four-cell solution branch PM . The unfolded symmetry breaking point, $SB4$ in Figure 4.6(a) is labelled as $L6^*$ in Figure 4.6(b). At $Ro = 5$, contours of streamline are shown in Figures 4.8(a) and 4.8(g). For the same solutions, streamwise velocity perspective plots are shown in Figures 4.9(a) and 4.9(g). The corresponding isotherms are shown in Figures 4.10(a) and 4.10(g). The unfolding of the bifurcation diagram for the case of uniform cooling of the duct is shown in Figure 4.6(c). It should be noted that for the case of a uniform cooling of duct, the branches $B1$, $B2$, $B3$ and $B4$ are smoothly connected through asymmetric branches present in isothermal

case. The asymmetric branches present in isothermal case, are connected through these branches in a different way than for the case of heating. During the unfolding due to cooling, $B1$ is connected through the upper $AS1$, $B2$ through lower $AS1$, $B3$ through lower $AS3$ and $B4$ through the upper $AS3$. Thus, exactly opposite asymmetric branches are chosen for the new disconnected branches in the case of cooling than that for the case of heating. Apart from this fact, other features of the unfolding process are essentially the same as for the heating case. A similar unfolding under heating/cooling is also shown in terms of other state functions θ and ψ . The corresponding bifurcation diagrams are shown in Figures 4.5 – 4.7.

The second set of results was computed for a higher degree of buoyancy effect. Consequently, in these solutions we expect a greater degree of asymmetry. The parameters chosen for this study are $Gv = 10^6$ and $\eta = 10^{-3}$, and keeping all other parameters fixed. As the degree of asymmetry increases we observed a greater amount of unfolding. This fact is shown in the state diagrams representing the solution structures for this parameter space. Two new state parameters fRe , frictional coefficient and Nu , Nusselt number are obtained. The friction factor is defined as

$$fRe = \frac{2}{\langle w \rangle Ek(1 + \gamma)^2} \quad (4.29)$$

The Nusselt number is defined by

$$Nu = \frac{RoPr \langle w \rangle}{Ek \langle \theta_b \rangle (1 + \gamma)^2} \quad (4.30)$$

where the average bulk temperature $\langle \theta_b \rangle$ can be computed from

$$\langle \theta_b \rangle = \frac{\int_{-0.5}^{+0.5} \int_{-0.5}^{+0.5} w \theta dx dy}{Area \langle w \rangle}$$

In the forced convection limit *i.e.*, zero rotation and zero buoyancy, we obtained $fRe = 14.4155$ and $Nu = 3.6328$. The parameters, $\gamma = 1$, $Ek = 0.1$, $Ro = 10^{-4}$ and

$Gr = 0$ were chosen for simulating a forced convection limit. The values of fRe and Nu obtained in the forced convection limit are very close to the values in the literature (Shah & London, 1978). This also serves as a validation of our code. The state diagrams are plotted with respect to Grashoff number, Gr . The bifurcation diagrams in Figures 4.11, 4.12 and 4.13 are given for Q , fRe and Nu respectively with respect Ro and Gr . Because the state functions, Q , fRe and Nu are integrated quantities, the difference in their values corresponding to different solution branches at the same value of Ro or Gr is not so significant that they can be seen graphically. Since the state functions are one-dimensional projections of the solution paths, some paths may appear to intersect in certain projections and other branches that are distinct may appear to be coincident. At the bifurcation point, however, they must intersect at the same value of Ro or Gr in every possible projection- *i.e.*, the entire solution vector of the discretized problem should be the same at such critical points. Thus, for stronger heating effects we also represent the solution structure in terms of local state functions, streamwise velocity, w and streamfunction, ψ measured at the location $(-0.45, 0.05)$. This spatial location was chosen since the flow profile changes most significantly in this region and both branches of any asymmetric solution will be made visible. A greater amount of unfolding is clearly illustrated in Figure 4.14 and Figure 4.15. These figures show the bifurcation diagram for unfolded branches with w and ψ as state functions, respectively. For a stronger buoyancy effect, the limit point on branch $B1$ disappears. The remaining three branches have a limit point. Figure 4.16, Figure 4.17 and Figure 4.18 show streamline contour plots, streamwise velocity perspective plots and isotherms contours respectively. In these figures, (b) and (f) are the solution on branch $B2$, (d) is a solution on branch $B1$, (e) and (c) are solution on branch $B3$ and (a) and (g) are solutions on branch $B4$.

Next we describe the unfolding process at $SB1$ with a greater degree of heating.

The behaviour is quite similar at the other symmetry breaking bifurcation points. As Gv increases, $SB1$ is unfolded into a limit point, $L2^*$ close to $L2$. With increasing Gv , these two limit points coalesce into a hysteresis or cusp point at a critical value of Gv as shown in Figure 4.19. Above this critical value, these limit points disappear. We have calculated $L2$ and $L2^*$ as functions of Gv . The result is shown in Figure 4.20. This figure shows how these limit points approach each other in the bifurcation diagram of the state functions w and ψ versus Ro .

4.4 Conclusions

The unfolding of the bifurcation structure for the case of flow through a rotating duct with heating/cooling is studied. The presence of buoyancy breaks the symmetry in the problem. This results in unfolding of the symmetry breaking points. They disappear through a cusp bifurcation, which result in a smooth unfolding of various branches. The four asymmetric branches appear in the unfolded bifurcation diagram. These asymmetric branches smoothly connect through the asymmetric branches and the limit points of isothermal case. Only two limit points present in the isothermal case remain robust to the unfolding by buoyancy. There are seven solutions present at $Ro = 5$, all of them asymmetric. The unfolding for a greater amount of heating shows a greater amount of asymmetry. At a fixed rotation, the degree of asymmetry increases with an increase of buoyancy effect. When the buoyancy effect overwhelms the Coriolis effect, the flow structure is very similar to that in mixed convection flow.

DIMENSIONLESS PARAMETERS

$$\gamma = b/a \quad Ek = \frac{\nu}{b^2 \Omega} \quad Ro = \frac{U}{b \Omega} \quad Pr = \frac{C_p \mu}{k} \quad \eta = \beta \Delta \theta$$

$$Gv = \frac{g b^3}{\nu^2} \quad fRe = \frac{2}{\langle w \rangle Ek (1 + \gamma)^2} \quad Q = Area \langle w \rangle$$

$$Nu = \frac{Ro Pr \langle w \rangle}{Ek \langle \theta \rangle (1 + \gamma)^2} \quad Gr = \frac{2 \langle w \rangle Pr Gv Ro}{(1 + \gamma) Ek}$$

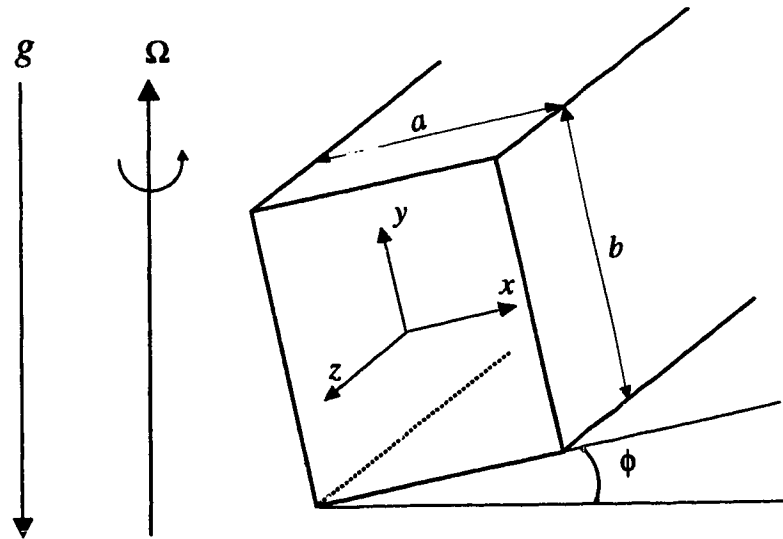


Figure 4.1: Geometry and coordinate system

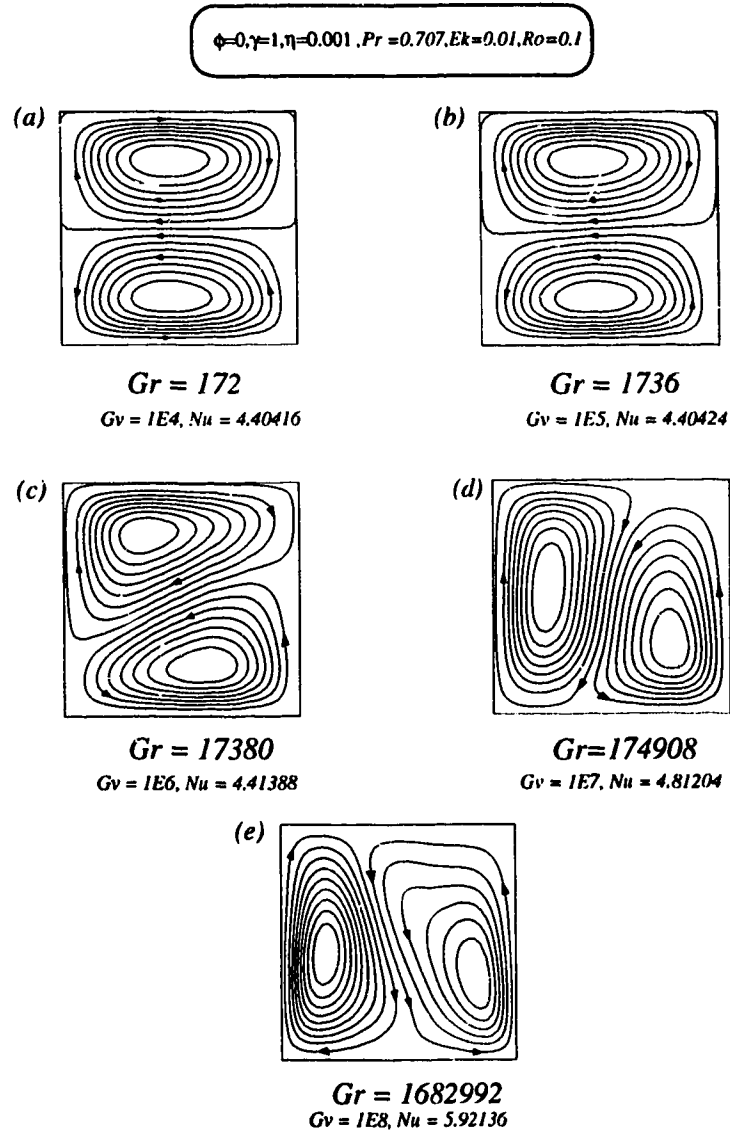


Figure 4.2: This figure shows the contours of streamline with increasing Gr for $\phi = 0, \gamma = 1, \eta = 0.001, Pr = 0.707, Ek = 0.01, Ro = 0.1$.

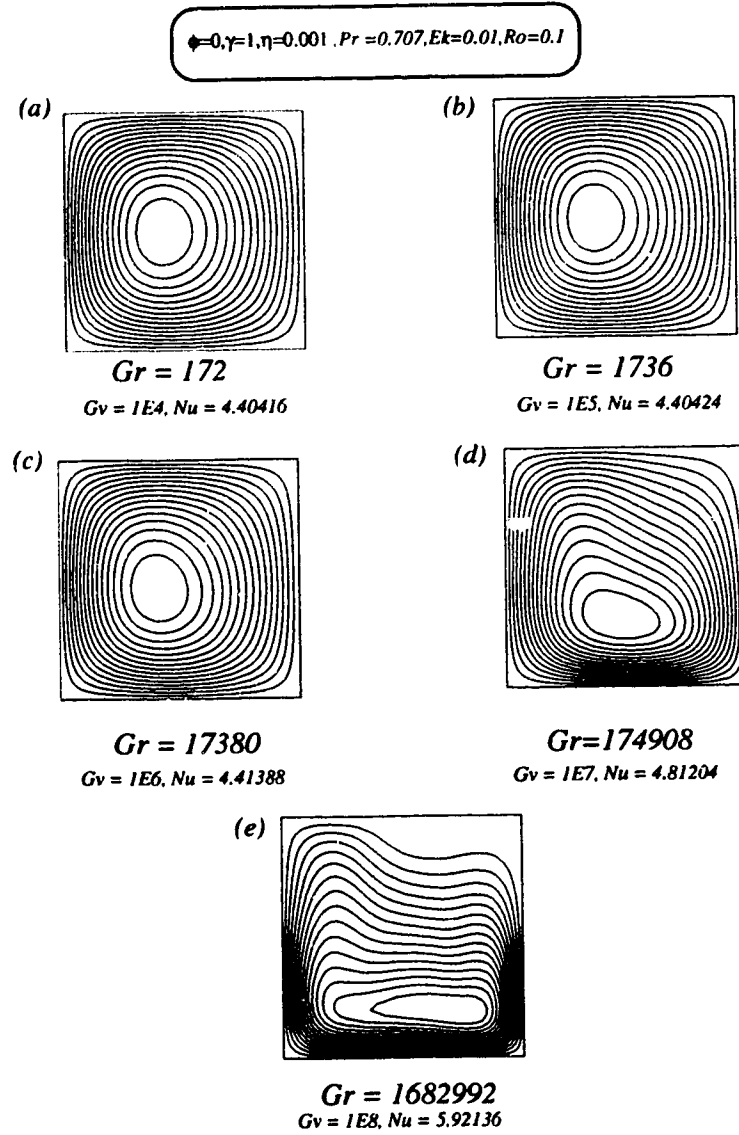


Figure 4.3: This figure shows the isotherms with increasing Gr for $\phi = 0, \gamma = 1, \eta = 0.001, Pr = 0.707, Ek = 0.01, Ro = 0.1$.

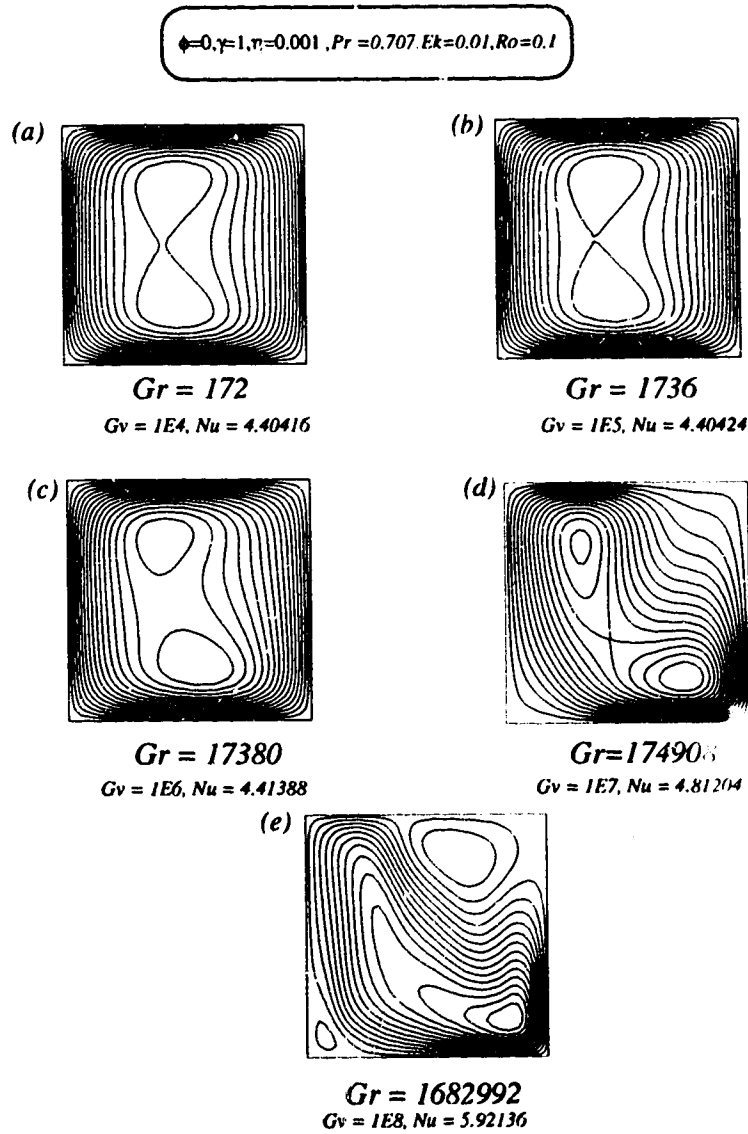


Figure 4.4: This figure shows the contours of streamwise velocity with increasing Gr for $\phi = 0, \gamma = 1, \eta = 0.001, Pr = 0.707, Ek = 0.01, Ro = 0.1$.

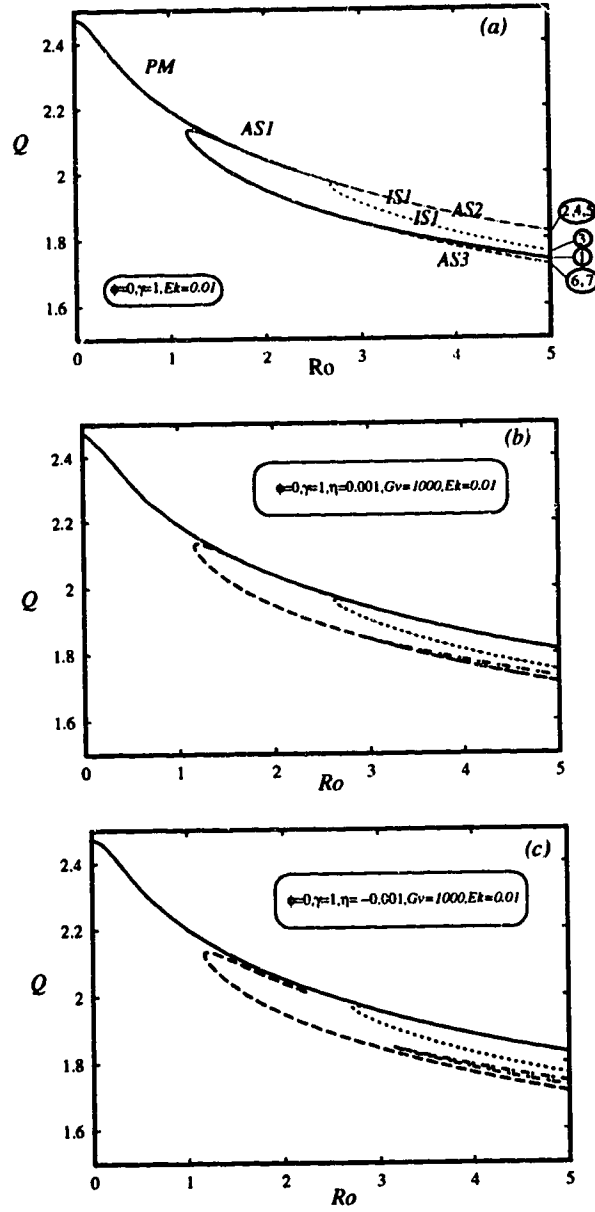


Figure 4.5: State diagram shows how the solution structure unfolds in the presence of non-isothermal effects for $\phi = 0, \gamma = 1, Gv = 1000, Pr = 0.707, Ek = 0.01$. Q vs. Ro for (a) isothermal case, (b) heating with $\eta = 0.001$ and (c) cooling with $\eta = -0.001$.

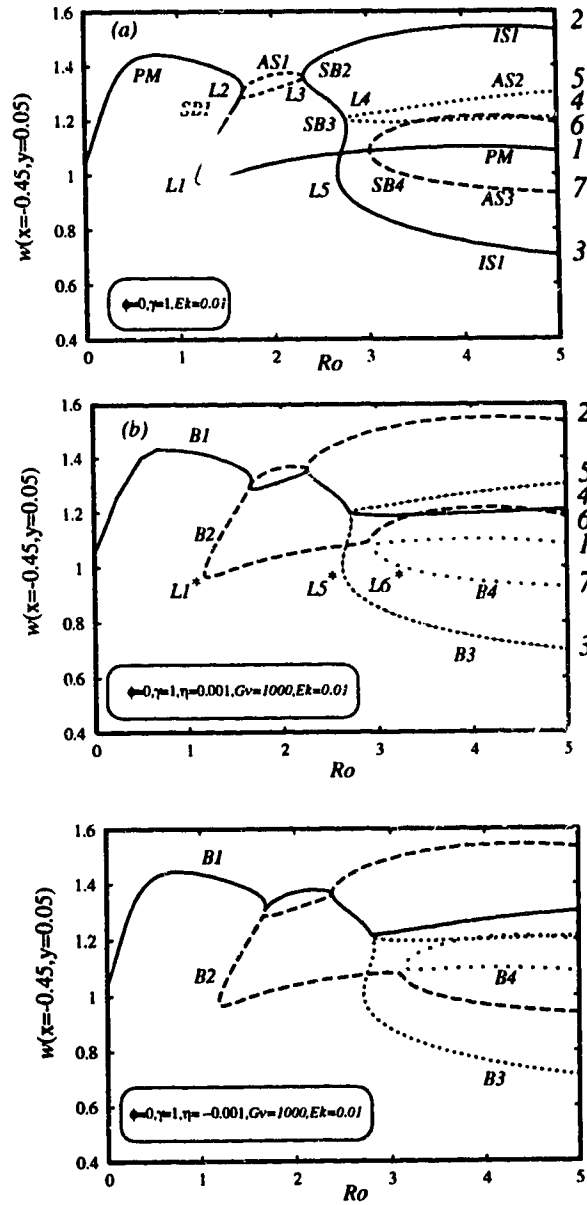


Figure 4.6: State diagram shows how the solution structure unfolds in the presence of non-isothermal effects for $\phi = 0, \gamma = 1, Gv = 1000, Pr = 0.707, Ek = 0.01$. $w(-0.45, 0.05)$ vs. Ro for (a) isothermal case, (b) heating with $\eta = 0.001$ and (c) cooling with $\eta = -0.001$.

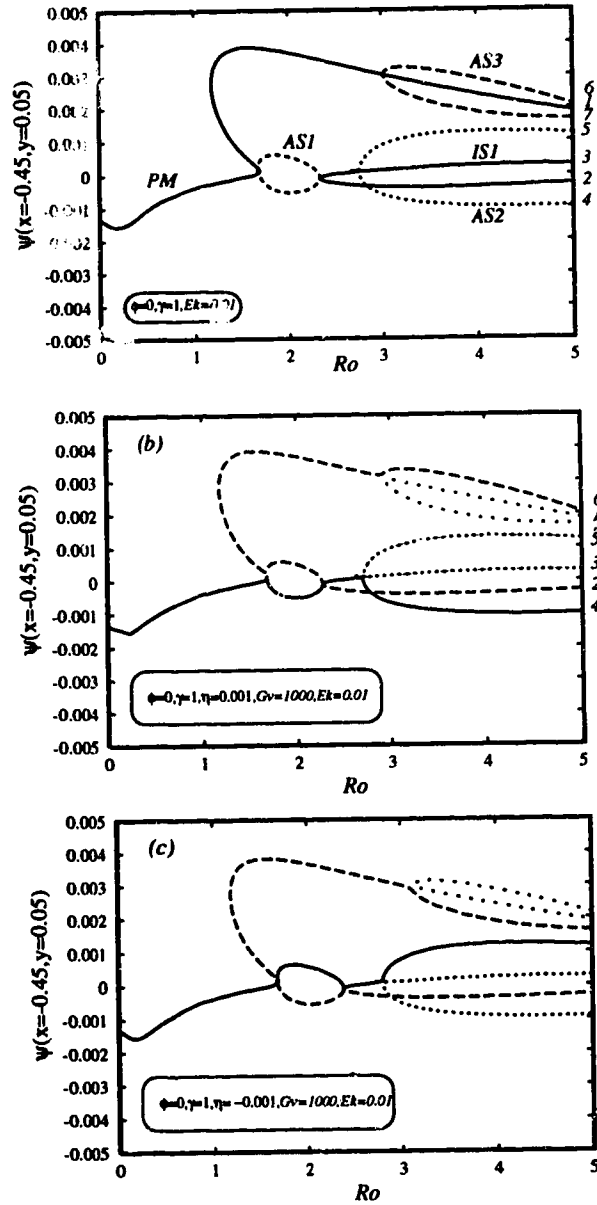


Figure 4.7: State diagram shows how the solution structure unfolds in the presence of non-isothermal effects for $\phi = 0, \gamma = 1, Gv = 1000, Pr = 0.707, Ek = 0.01$. $\psi(-0.45, 0.05)$ vs. Ro for (a) isothermal case, (b) heating with $\eta = 0.001$ and (c) cooling with $\eta = -0.001$.

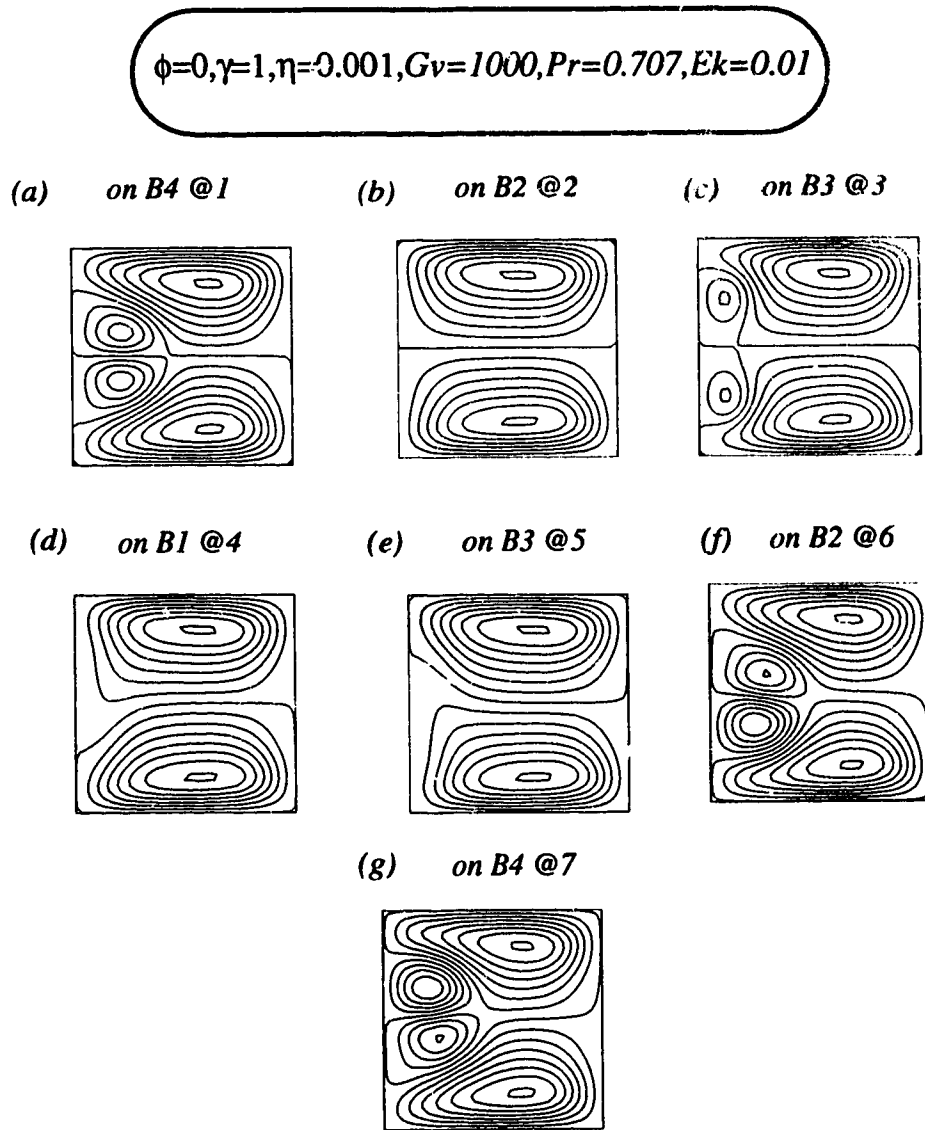


Figure 4.8: Streamline contours for seven solutions present at $Ro = 5$ for $\phi = 0, \gamma = 1, \eta = 0.001, Gv = 1000, Pr = 0.707, Ek = 0.01$. Points refer to the labels on Figure 4.6(b).

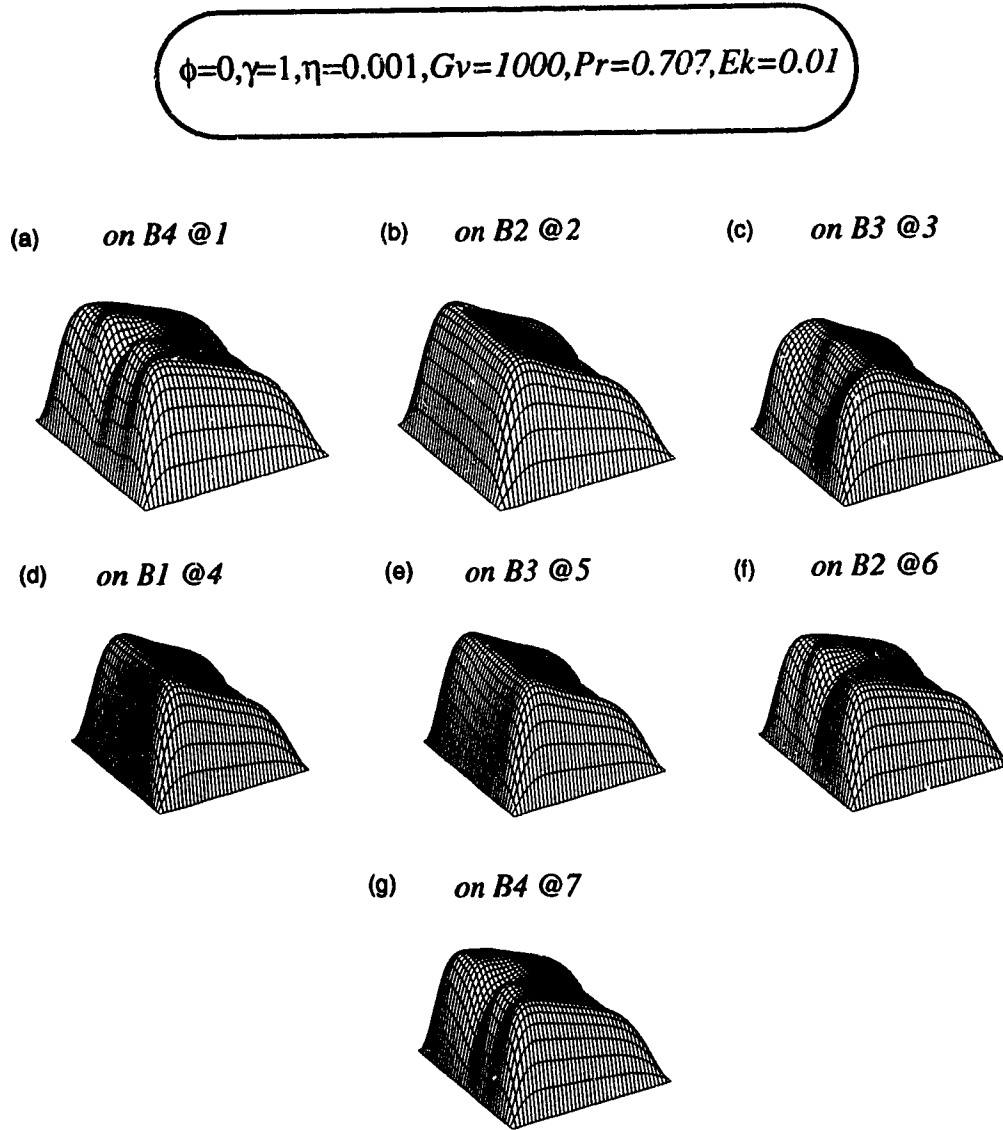


Figure 4.9: Streamwise velocity perspectives for seven solutions present at $Ro = 5$ for $\phi = 0, \gamma = 1, \eta = 0.001, Gv = 1000, Pr = 0.707, Ek = 0.01$. Points refer to the labels on Figure 4.6(b).

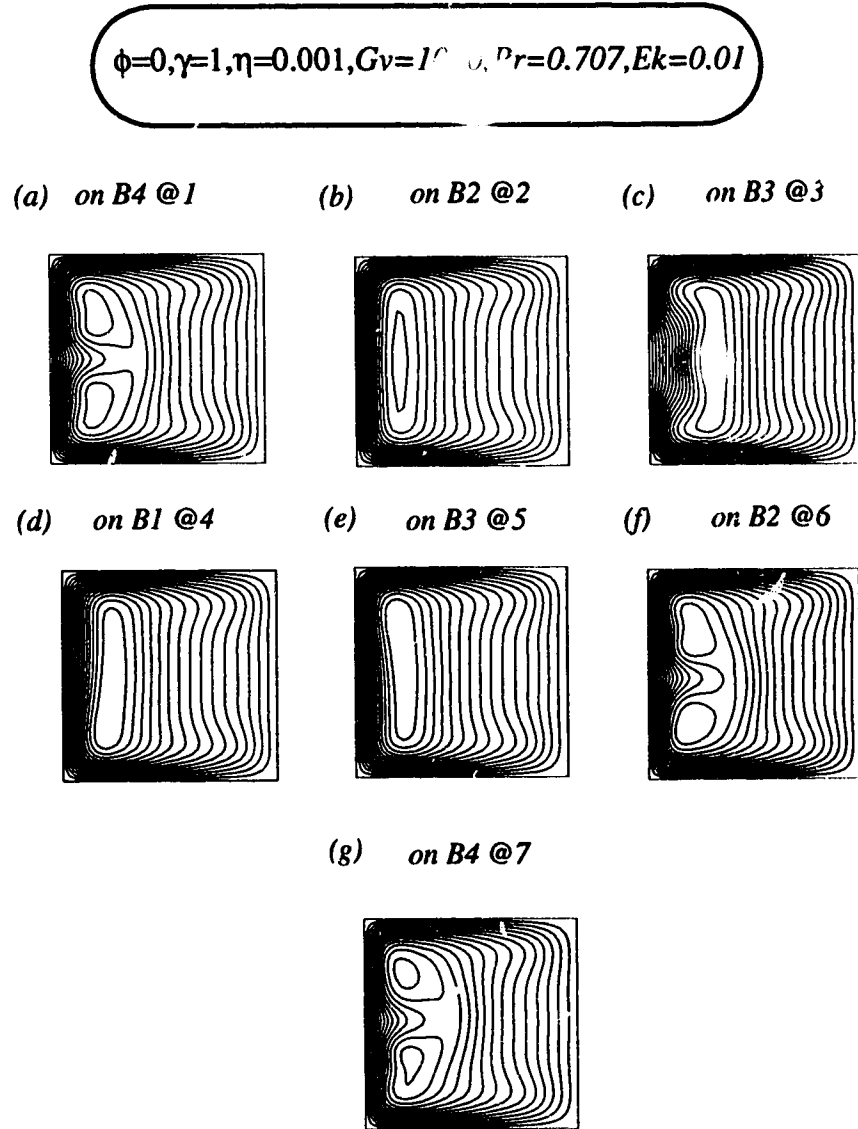


Figure 4.10: Isotherms for seven solutions present at $Ro = 5$ for $\phi = 0, \gamma = 1, \eta = 0.001, Gv = 1000, Pr = 0.707, Ek = 0.01$. Points refer to the labels on Figure 4.6(b).

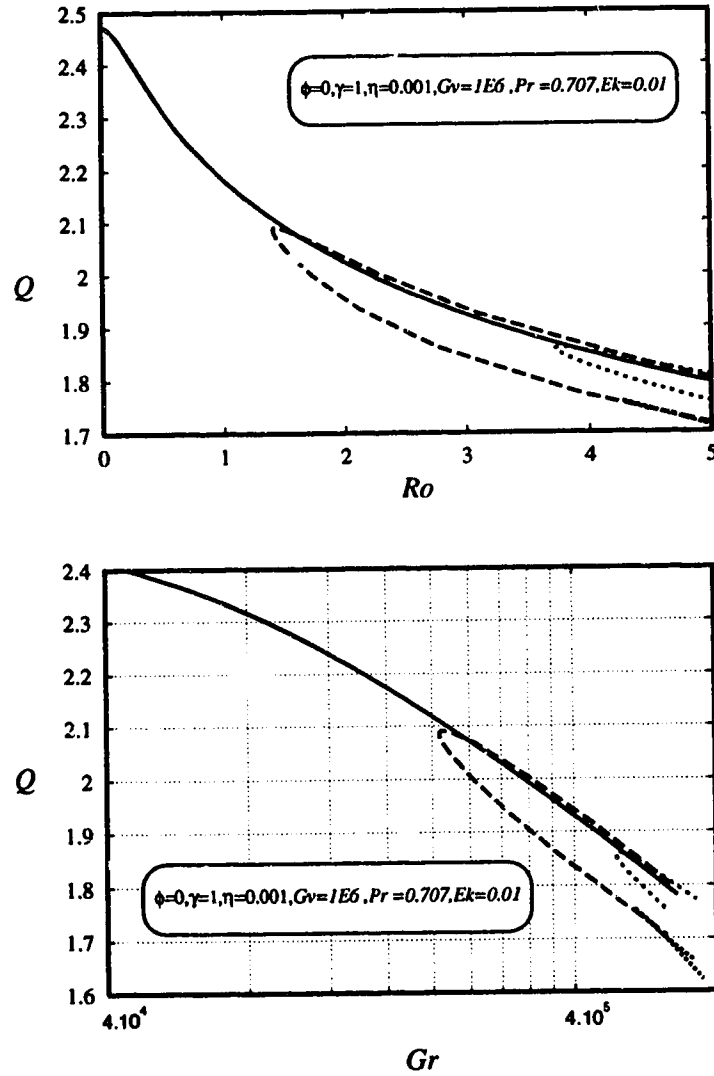


Figure 4.11: State diagram shows how the solution structure unfolds in the presence of non-isothermal effects for $\phi = 0, \gamma = 1, \eta = 0.001, Gv = 10^6, Pr = 0.707, Ek = 0.01$. (a) Q vs. Ro and (b) Q vs. Gr

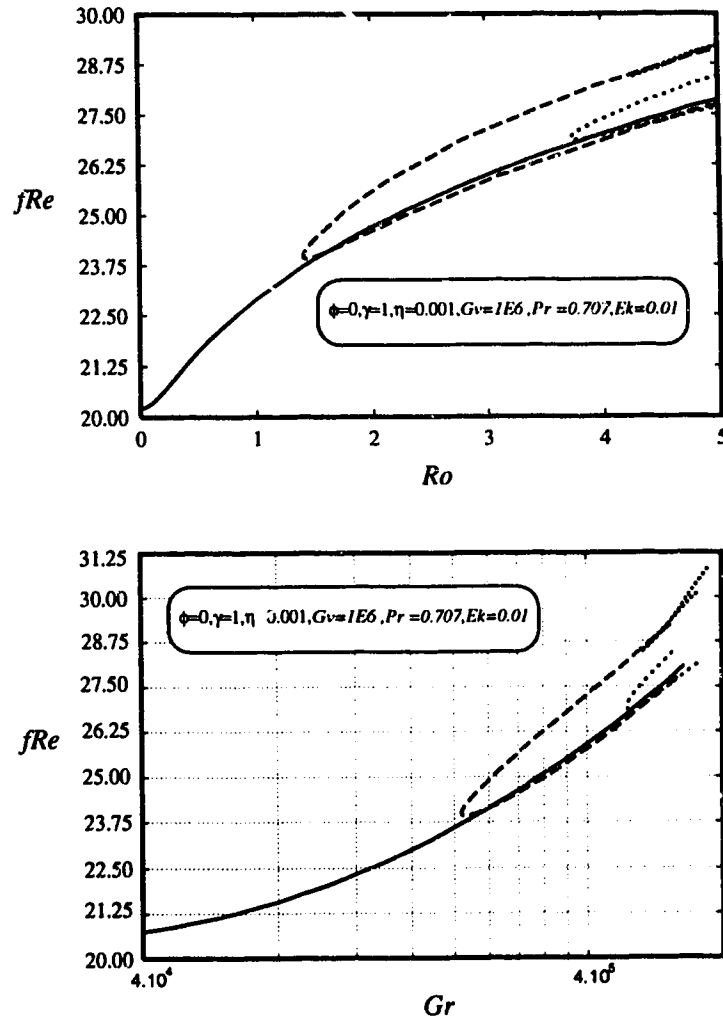


Figure 4.12: State diagram shows how the solution structure unfolds in the presence of non-isothermal effects for $\phi = 0, \gamma = 1, \eta = 0.001, Gv = 10^6, Pr = 0.707, Ek = 0.01$. (a) fRe vs. Ro and (b) fRe vs. Gr

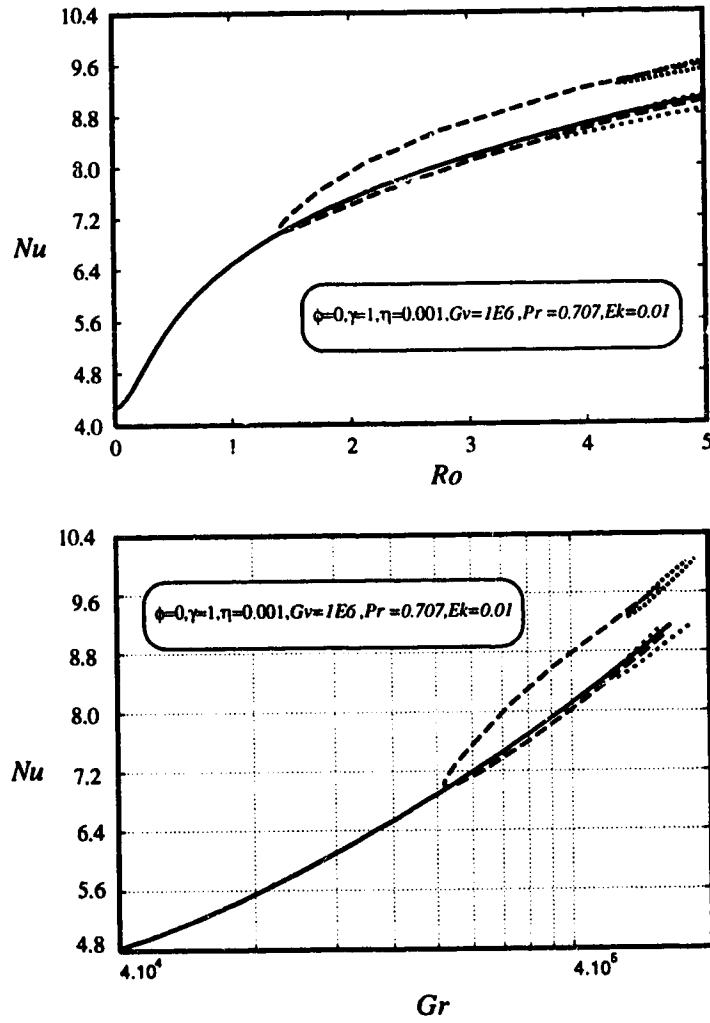


Figure 4.13: State diagram shows how the solution structure unfolds in the presence of non-isothermal effects for $\phi = 0, \gamma = 1, \eta = 0.001, Gv = 10^6, Pr = 0.707, Ek = 0.01$. (a) Nu vs. Ro and (b) Nu vs. Gr

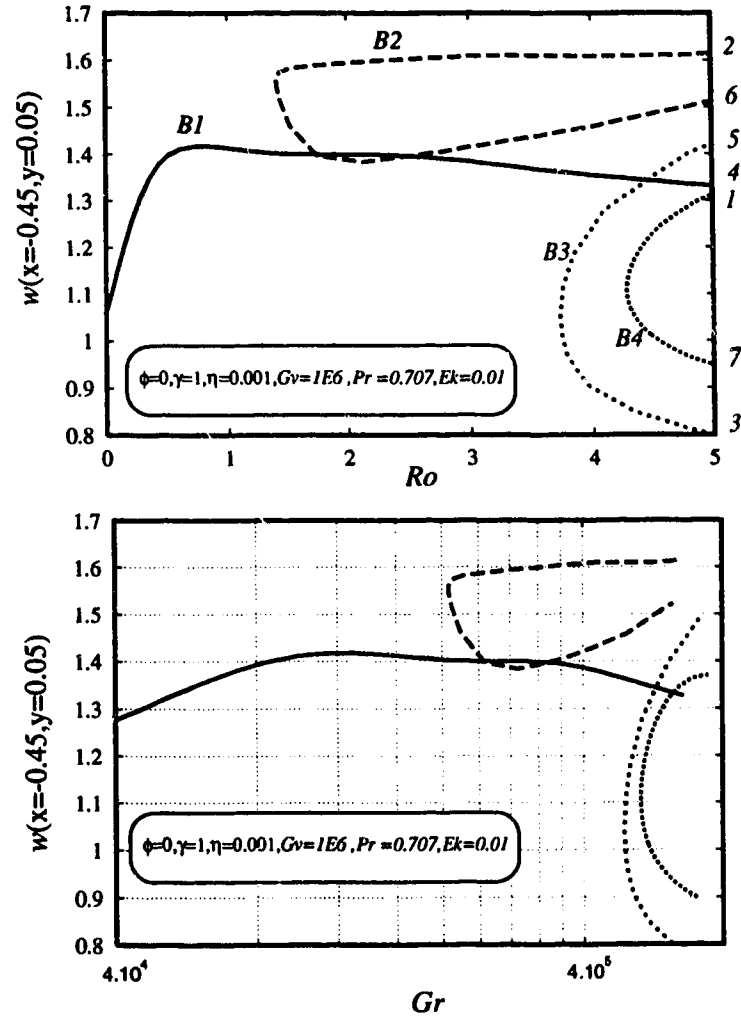


Figure 4.14: State diagram shows how the solution structure unfolds in the presence of non-isothermal effects for $\phi = 0$, $\gamma = 1$, $\eta = 0.001$, $Gv = 10^6$, $Pr = 0.707$, $Ek = 0.01$. (a) $w(-0.45, 0.05)$ vs. Ro and (b) $w(-0.45, 0.05)$ vs. Gr

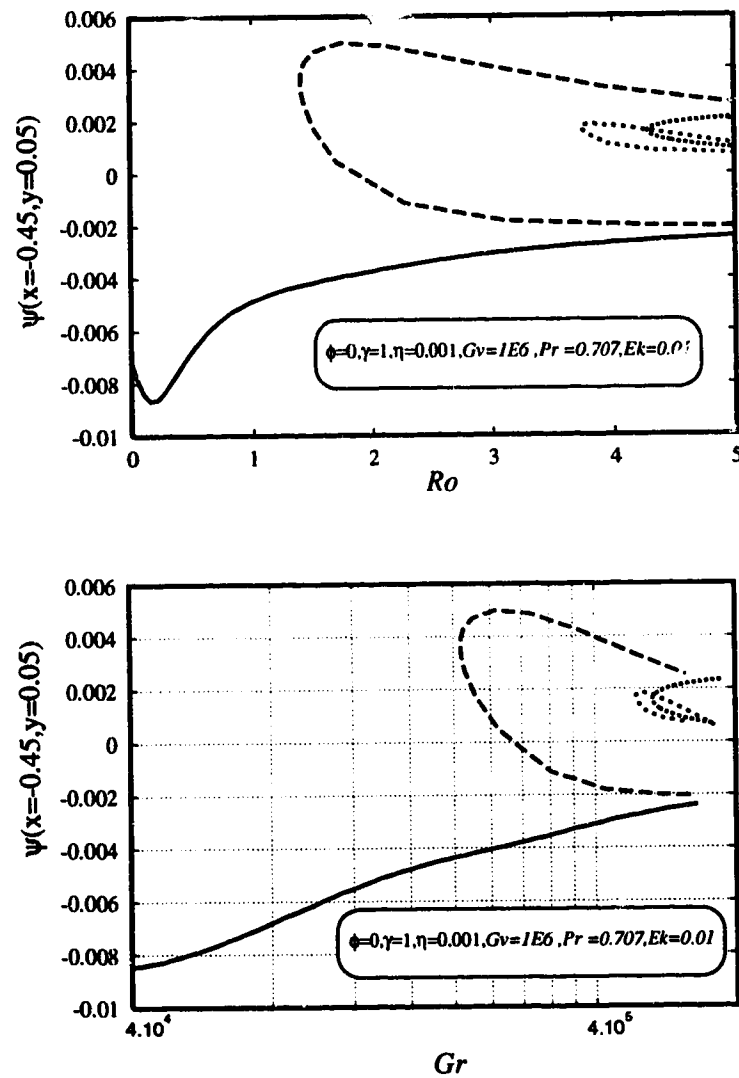


Figure 4.15: State diagram shows how the solution structure unfolds in the presence of non-isothermal effects for $\phi = 0$, $\gamma = 1$, $\eta = 0.001$, $Gv = 10^6$, $Pr = 0.707$, $Ek = 0.01$. (a) $\psi(-0.45, 0.05)$ vs. Ro and (b) $\psi(-0.45, 0.05)$ vs. Gr

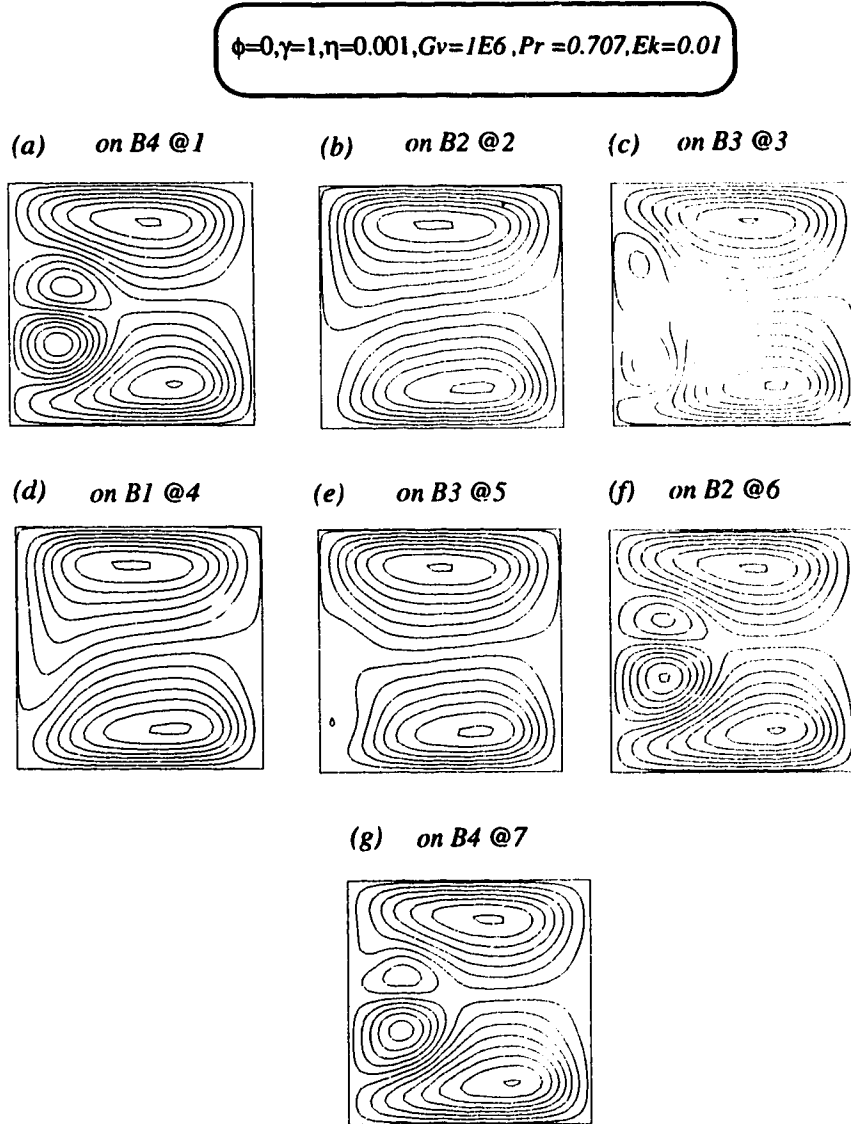


Figure 4.16: Streamline contours for seven solutions present at $Ro = 5$ for $\phi = 0, \gamma = 1, \eta = 0.001, Gv = 10^6, Pr = 0.707, Ek = 0.01$. Points refer to the labels on Figure 4.14(a).

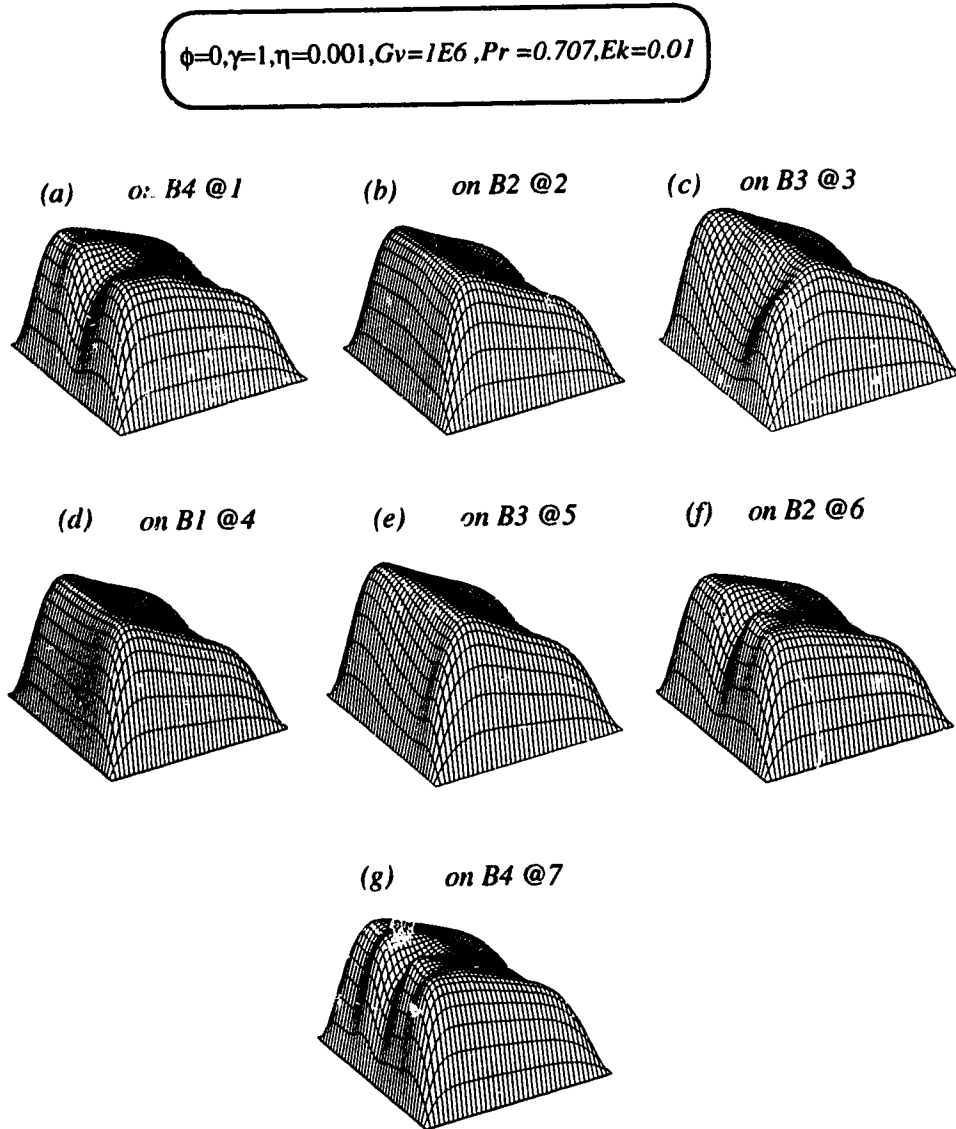


Figure 4.17: Streamwise velocity perspectives for seven solutions present at $Ro = 5$ for $\phi = 0, \gamma = 1, \eta = 0.001, Gv = 10^6, Pr = 0.707, Ek = 0.01$. Points refer to the labels on Figure 4.14(a).

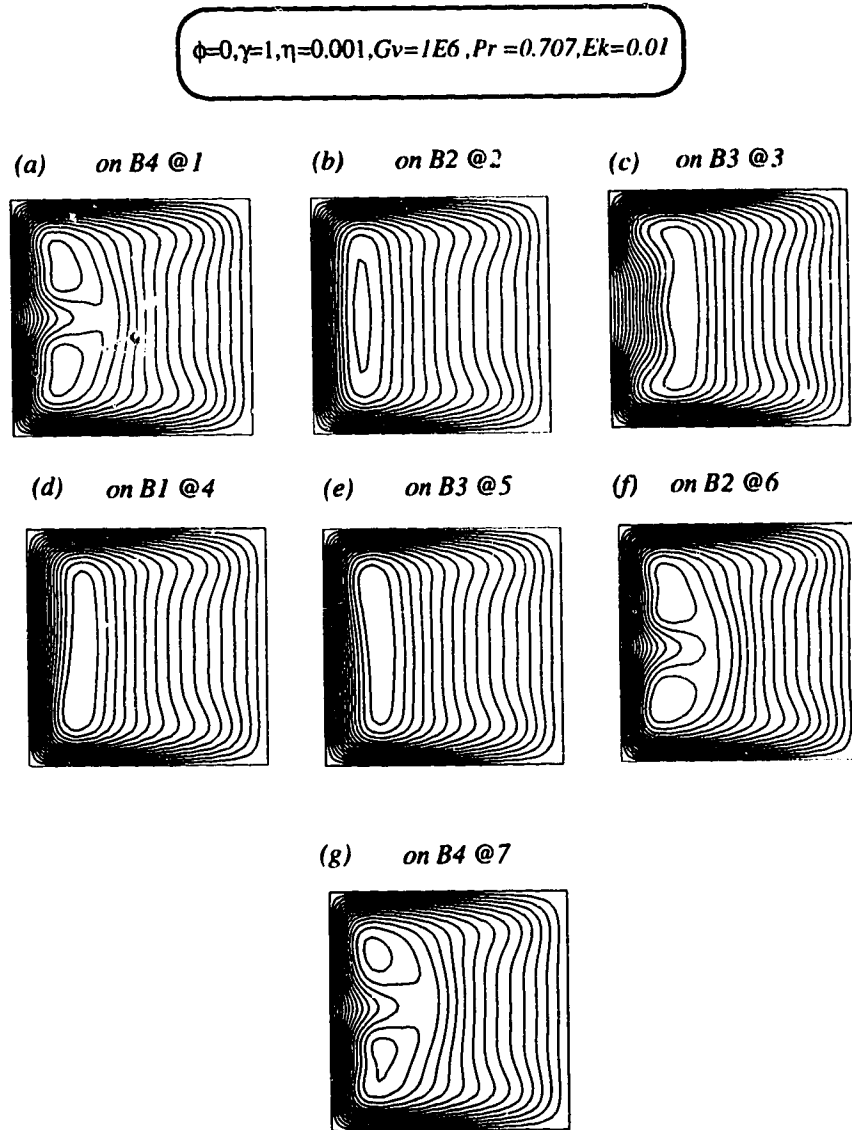


Figure 4.18: Isotherms for seven solutions present at $Ro = 5$ for $\phi = 0, \gamma = 1, \eta = 0.001, Gv = 10^6, Pr = 0.707, Ek = 0.01$. Points refer to the labels on Figure 4.14(a).

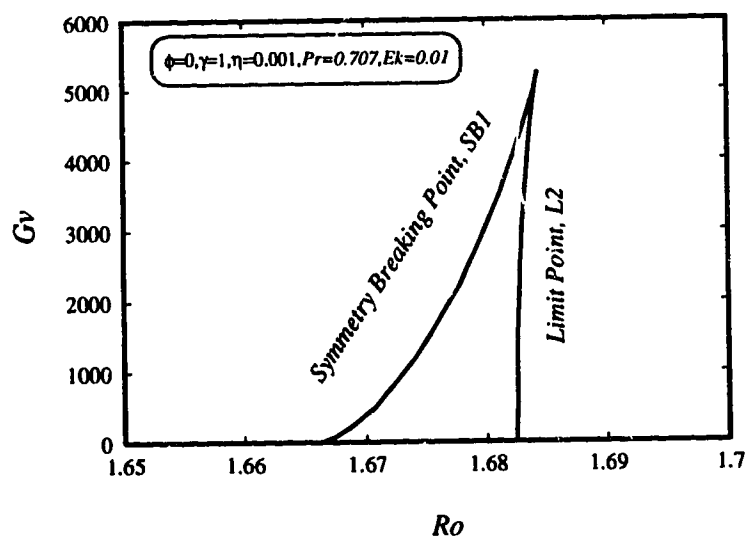


Figure 4.19: Unfolding of $SB1$ for $\phi = 0, \gamma = 1, \eta = 0.001, Pr = 0.707, Ek = 0.01$ with heating.

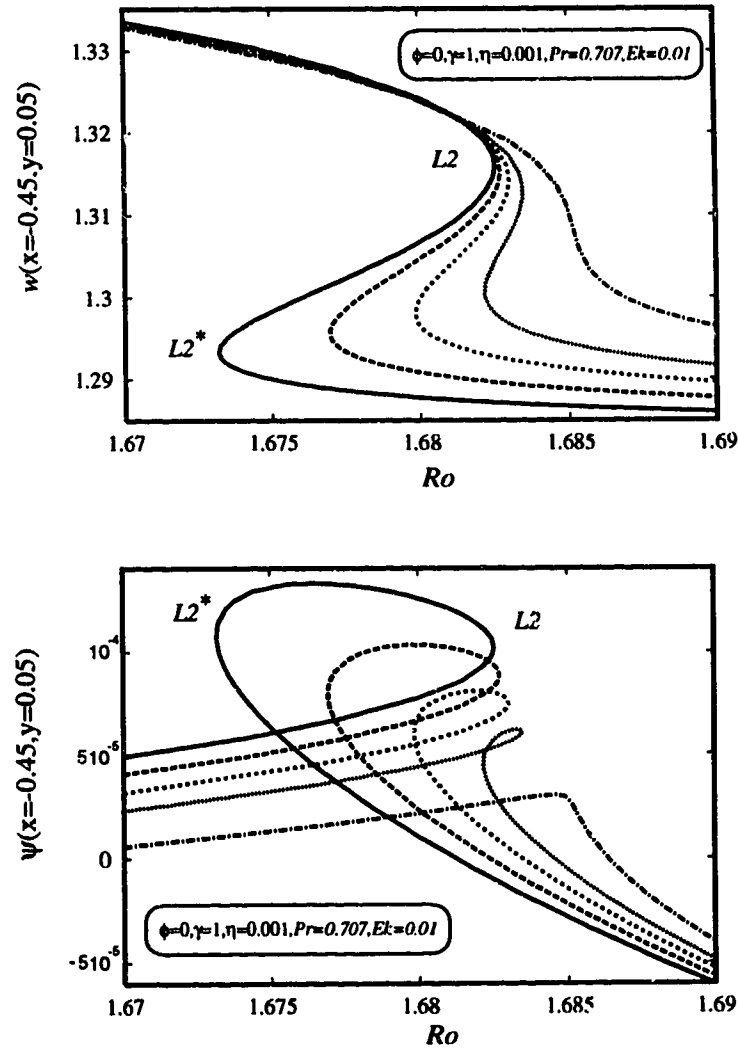


Figure 4.20: Unfolding of SB1 for $\phi = 0$, $\gamma = 1$, $\eta = 0.001$, $Pr = 0.707$, $Ek = 0.01$ with increasing $Gv = 1000, 2000, 3000, 4000$, and 5000 . (a) $w(-0.45, 0.05)$ vs. Ro and (b) $\psi(-0.45, 0.05)$ vs. Ro

References

- CHENG, K.C., & HWANG, G.J. 1969. Numerical solution for combined free and forced laminar convection in horizontal rectangular channels. *Trans. ASME C: J. Heat Transfer*, **91**, 59–66.
- CHOU, F.C., & HWANG, G.-J. 1984. Combined free and forced laminar convection in horizontal rectangular channels for high $Re - Ra$. *Can. J. Chem. Engng*, **62**, 830–836.
- FARIS, G.N., & VISKANTA, R. 1969. An analysis of combined forced and free convection heat transfer in a horizontal tube. *Intl J. Heat Mass Transfer*, **12**, 1295–1309.
- HWANG, G.-J., & CHENG, K.C. 1970. Boundary vorticity method for convective heat transfer with secondary flow-applications to the combined free and forced convection in horizontal tubes. *Heat Transfer*, **4**, Paper NC3.5.
- IQBAL, M., & STACHIEWICZ, J.W. 1966. Influence of tube orientation on combined free and forced laminar convection heat transfer. *Trans. ASME C: J. Heat Transfer*, **88**, 109–116.
- MORRIS, W.D. 1981. *Heat Transfer and Fluid Flow in Rotating Coolant Channels*. Research Studies Press, John Wiley and Sons.

- MORTON, B.R. 1959. Laminar convection in uniformly heated horizontal pipes at low Rayleigh numbers. *Q. J. Mech. Appl. Maths*, **12**, 410–420.
- NANDAKUMAR, K., & WEINITSCHKE, H.J. 1991. A bifurcation study of mixed-convection heat transfer in horizontal ducts. *J. Fluid Mech.*, **231**, 157.
- NANDAKUMAR, K., MASLIYAH, JACOB H., & LAW, HIN-SUM. 1985. Bifurcation in steady laminar mixed convection flow in horizontal ducts. *J. Fluid Mech.*, **152**, 145–161.
- NANDAKUMAR, K., RASZILLIER, H., & DURST, F. 1991. Flow through rotating rectangular ducts. *Phys. Fluids A*, **3**, 770.
- PATANKAR, S.V., RAMAKHYANI, S., & SPARROW, E.M. 1978. Effect of circumferentially nonuniform heating on laminar combined convection in a horizontal tube. *Trans. ASME C: J. Heat Transfer*, **100**, 63–70.
- SHAH, R.K., & LONDON, A.L. 1978. *Laminar Flow Forced Convection in Ducts*. Academic.
- SOONG, C.Y., LIN, S.T., & HWANG, G.J. 1991. An experimental study of convective heat transfer in radially rotating rectangular ducts. *Trans. ASME C: J. Heat Transfer*, **113**, 604.
- WANG, L. 1995. *Fluid Flow and Heat Transfer in Rotating Curved Channels*. University of Alberta: Ph.D Thesis.

Chapter 5

Conclusions and Recommendations

In this work we first examined the the multiplicity features and the secondary flow structure of the fully developed, laminar flow of a Newtonian fluid in a straight pipe that is rotating about an axis perpendicular to the pipe axis (Chapter 2). The governing equations of motion were solved numerically using the control volume method and the SIMPLE algorithm. Results were presented for a fixed Ekman number of $Ek = 0.01$ and a range of Rossby numbers between 0 and 20. The primary solution branch begins as a unique solution at low Rossby numbers. Its secondary flow structure consists of two-cells. At higher values of Ro a hitherto unknown solution with a four-cell flow structure appears, which coexists with the two-cell flow structure over a range of Ro up to 20. Transient, two-dimensional simulations were carried out to determine the stability of the solutions to two-dimensional perturbations. The two-cell flow structure is stable to both symmetric and asymmetric perturbations. The four-cell flow structure is stable to symmetric perturbations and unstable to asymmetric perturbations, where it breaks down to a

two-cell flow structure. It should be noted that this transient breakdown of four-cell to two-cell flow structure is not experimentally realizable, since in any experiment there is a dominant, streamwise motion. Such a streamwise motion has been shown in the Dean problem by Bara *et al.* (1992). Any asymmetric perturbations due to the imperfections in experimental apparatus would grow and eventually destabilize the four-cell flow. Our present study is only limited to the stability analysis of two-dimensional flows to two-dimensional perturbations. A three-dimensional stability analysis is a natural extension to our present study. Another interesting consequence of the conditional stability of the two-dimensional, four-cell flow is that there must exist a symmetry breaking point some where along the primary solution branch. For both the curved pipe and rotating pipe problems, the complete bifurcation structure for the circular geometry is yet to be mapped out using continuation methods and extended systems for locating the various singular points. Questions regarding grid independent results for the location of the singular points also remain. It is very clear that the intermediate solution branch must be unstable. In our experience, the SIMPLE algorithm is capable of converging only to those solutions that are also physically stable. This procedure is adequate to demonstrate the existence of the four-cell flow solution for the rotating straight pipes. In our study, we did not find an unstable solution branch connecting the two-cell and four-cell branch as reported by Yang & Keller(1986) for curved pipe. To find all the solution branches, more powerful algorithms based on the continuation method should be devised. In Chapter 3, we used such an approach to track the solutions for flow through rotating rectangular ducts.

The equations for flow through a rotating rectangular duct were discretized using spectral approximations. The expansion functions were chosen as linear combinations of Chebyshev polynomials. This kind of discretization scheme is also

recommended for studying flow through a rotating pipe. In this problem we can use a combination of Chebyshev polynomials for discretizing in the radial direction and polynomials based on Fourier series for discretization in angular direction. Using the arclength continuation method we were able to find seven solutions at $Ro = 5$. In the bifurcation study of Nandakumar *et al.* (1991) of flow through rotating duct, all of these solutions show instability. They all have a pair of imaginary eigenvalues with positive real parts. Thus, the presence of Hopf bifurcation is expected. While time-periodic branches may emerge through Hopf bifurcation, they are believed to be physically unrealizable. It is likely that, as in the Dean problem (Sankar *et al.*, 1993), flows with periodic structure along the duct will develop, which imply a breaking of the continuous translation symmetry assumed in the present work down to a discrete one. A study of such three-dimensional flow for a rectangular geometry is also required. We have shown the effect of Ek on the solution structure for asymptotic limits. In the asymptotic limit of rapid rotation, boundary layer flow exists. To resolve these thin boundary layers, a study of their stability at higher values of Ro is required.

In Chapter 4, we studied the effects of heating/cooling on the flow through a rotating duct. The buoyancy effect drives a secondary flow in a direction orthogonal to the Coriolis driven secondary flow. Thus, in the bifurcation diagrams obtained, we see a smooth unfolding of the branches. The symmetry breaking points unfold through a tilted cusp bifurcation. For stronger heating effects, we observed a greater degree of asymmetry. Further, it was shown that bifurcations in mixed convection flow (Nandakumar & Weinitschke, 1991) and isothermal flow through a rotating duct (Nandakumar *et al.*, 1991), are the asymptotic cases of nonisothermal flow through a rotating duct. The asymmetric solutions in both the problems can be obtained by adjusting the relative magnitudes of buoyancy and Coriolis effects.

References

- BARA, B., NANDAKUMAR, K., & MASLIYAH, J.H. 1992. An experimental and numerical study of the Dean problem: flow development towards two-dimensional multiple solutions. *J. Fluid Mech.*, **244**, 339.
- NANDAKUMAR, K., & WEINITSCHKE, H.J. 1991. A bifurcation study of mixed-convection heat transfer in horizontal ducts. *J. Fluid Mech.*, **231**, 157.
- NANDAKUMAR, K., RASZILLIER, H., & DURST, F. 1991. Flow through rotating rectangular ducts. *Phys. Fluids A*, **3**, 770.
- SANKAR, S. RAVI, MEES, P.A.J., & NANDAKUMAR, K. 1993. Development of three-dimensional, streamwise-periodic flows in mixed-convection heat transfer. *J. Fluid Mech.*, **255**, 683.
- YANG, Z., & KEEFE, H.B. 1986. Multiple laminar flows through curved pipes. *Applied Numerical Mathematics*, **2**, 257.